ABSTRACT

Title of Document: CORRELATING ELECTROCHEMICAL PERFORMANCE WITH *IN SITU* OPTICAL SPECTROSCOPY IN SOLID OXIDE FUEL CELLS

Bryan Christopher Eigenbrodt,
Doctor of Philosophy, 2011

Directed By: Professor Robert A. Walker
Department of Chemistry and Biochemistry

Solid oxide fuel cells are versatile electrochemical devices that can operate with a wide variety of carbon containing fuels. However, SOFCs operate at high temperatures (≥650˚C) making *in situ* characterization of material properties and reaction mechanisms, associated with electrochemical fuel oxidation, difficult to perform. Experiments described employed *in situ* vibrational spectroscopy and standard electrochemical methods to characterize the properties of SOFC electrolytes and anodes at temperatures up to 715˚C. Collectively these methods address long standing questions about fuel oxidation and degradation mechanisms.

One investigation coupled *in situ* Raman with surface specific EIS measurements to show that yttria stabilized zirconia electrolytes form a slightly conductive, surface reduced layer under anodic conditions commonly encountered during SOFC operation. Polarizing the SOFC further depleted oxide ion

concentrations close to the three phase boundary. Additional *ex situ* XAS measurements confirmed that only zirconium, in the crystal structure, plays a role in the formation of conductive surface states in reduced YSZ.

A second project combined electrochemical measurements with kinetically resolved *in situ* spectroscopic data to compare the performance and oxidation mechanisms of SOFCs operating with methanol and methane. Methanol exhibited higher percentages in utilization and conversion at the anode as compared to methane. Results emphasized that this increase in reactivity enabled the methanol fuel to pyrolyze into carbon deposits on the anode at a faster rate and significant amounts leading to greater degradation in electrochemical performance than compared to methane.

The final project investigated the internal oxidative and steam reforming of methane and ethanol using *in situ* Raman, real time electrochemical, and FTIR exhaust measurements. EIS data show that direct methane and ethanol lead to anode degradation that correlates directly with the appearance of aggressive carbon deposits on the anode surface. *Ex situ* FTIR measurements revealed that methane doesn't undergo pyrolysis but when reformers were introduced into the fuel, a mixture of H_2, CO, CO_2, and H_2O was created. These same measurements show a decrease in acetylene when H_2O was introduced into ethanol. *In situ* Raman measurements showed that carbon formation could be completely suppressed in the presence of these reformers, especially at high cell overpotentials.

CORRELATING ELECTROCHEMICAL PERFORMANCE WITH *IN SITU* OPTICAL SPECTROSCOPY IN SOLID OXIDE FUEL CELLS

By

Bryan Christopher Eigenbrodt

Dissertation submitted to the Faculty of the Graduate School of the
University of Maryland, College Park, in partial fulfillment
of the requirements for the degree of
Doctor of Philosophy
2011

Advisory Committee:
Professor Robert A. Walker, Chair
Professor Bryan W. Eichhorn
Professor Sang Bok Lee
Professor Neil V. Blough
Professor Gregory S. Jackson, Dean's Representative

Dedication

For my Mom and Dad, making it possible for me to dream of the future…

For Robert Walker, making those dreams a reality…

And for Melissa Ellis, making it possible for me to start dreaming again…

Acknowledgements

There are numerous people that deserve recognition and thanks for their involvement toward this thesis and support through out the duration of my graduate career. If it not for their unlimited guidance, contributions, and support this thesis would have not been possible.

My advisor, Professor Robert A. Walker, deserves an incredible amount of gratitude because if it wasn't for him this project would not be possible. His professionalism, expertise, and his enthusiasm towards science and exploring the unknown are truly inspiring to me and makes me want to strive become a better scientist. If not for his guidance and belief in me, I would not be the scientist that I am today, and for that I am eternally thankful to him.

The SOFC project is a collaborative effort comprised of chemists and mechanical engineers at the University of Maryland. Professors Bryan Eichhorn and Gregory Jackson, who are the principle investigators on this project, also deserve credit for their guidance, support, and helpful conversations. They both have provided me with so many resources to allow me to excel in this project. Other fuel cell group members, past and present, also deserve credit for their helpful conversations though out my time at the University of Maryland: Dr. Mary Sukeshini, Dr. Oktay Demirican, Dr. Steven DeCaluwe, Dr. Selim Alayoglu, Paul Jawlik, Dr. Chunjuan Zhang, and Siddharth Patel.

I would like to thank Dr. Michael Pomfret of the Naval Research Laboratory for, not only being a great friend but also a great mentor that helped me at the beginning of my graduate career to refine my experimental techniques in the area of

spectroscopic and electrochemical measurements. This project would not exist if not for the combining efforts of Professor Walker and Dr. Pomfret who designed the optically accessible SOFC apparatus that made it possible to use Raman spectroscopy to investigate the chemistry occurring in SOFCs at these high temperatures. I would also like to thank Dr. Jeffery Owrutsky and Dr. Daniel Steinhurst, also at the Naval Research Laboratory, for their helpful conversations and contributions to this project.

I would like to thank the other members of my committee, including Professor Sang Bok Lee and Professor Neil Blough, for all their support and guidance.

I have had the opportunity to work with some of the greatest people in the Walker Research Group. Their friendship and motivation has made this process all that much more enjoyable. These members include: Dr. Suleyman Can, Dr. Wendy Heiserman, Dr. Michael Brindza, Dr. Anthony Dylla, Dr. Debjani Roy, Renee Siler, Eric Gobrogge, Lauren Woods, and especially John Kirtley who has contributed directly to the spectroscopic fuel cell work.

I would also like to thank the professors in the Physics and Mechanical Engineering Department at Montana State University for opening up their laboratories to me and providing insight into SOFC material development and operation. These professors include Dr. Stephen Sofie, Dr. Yves Idzerda, and Dr. Richard Smith. Martin Finsterbusch, also from Montana State University, also deserves recognition for his contributions to this thesis by providing the X-ray absorption measurements presented in Chapter III of this thesis.

I would like to thank the ones closest to me who have been there from the very beginning right by my side. To my family, your unending love and support have

been a guiding light that has led me not only though graduate school, but through out my life to make me the person that I am today. To my Mom and Dad, if not for all of your motivation, support, hard work and efforts to provide me with the best education that I could receive, I am confident to say I would not be here and have had this opportunity if it wasn't for both of you.

Finally, and most importantly, I would like to thank Melissa Ellis. I could have not have done this without you by my side and with all your support and help through out this entire process. You and your family have sacrificed so much to see me to this point in my life, and I am forever indebted to you and your family. I look forward to beginning the next chapter of life with you.

Table of Contents

List of Tables

List of Figures

List of Abbreviations

Abbreviation	**Meaning**
A	Absorbance
AC	Alternating current
C	Series equivalent capacitance of a cell
C_1	First capacitive element in DC equivalent circuit
C_2	Second capacitive element in DC equivalent circuit
C_3	Third capacitive element in DC equivalent circuit
CCD	Charged couple device
Cermet	Ceramic-metal
D	Refers to the diagnostic peak of disorder in graphite
DMFC	Direct methanol fuel cell
E	Energy
EIS	Electrochemical impedance spectroscopy
FC	Fuel cell
FRA	Frequency response analyzer
FTIR	Fourier transform infrared spectroscopy
G	Refers to the diagnostic peak of disorder in graphite
h	Planck constant
I.	Measured current
I_o	Excitation intensity
I_R	Raman intensity
L	Path length
LSM	Lanthanum strontium manganate
LSV	Linear sweep voltammetry
MCFC	Molten carbonate fuel cell
MEA	Membrane electrode assembly
MIEC	Mixed ionic and electronic conductor

N	Number of molecules present in sample
NIR	Near-infrared
O_o^0	Filled oxide vacancy
OCV	Open circuit voltage
PAFC	Phosphoric acid fuel cell
PEMFC	Polymer electrolyte fuel cell
PV-work	Pressure and volume work
Q_j	Specific vibrational mode being excited
R	Pure ohmic resistance
R_1	First resistive element in DC equivalent circuit
R_2	Second resistive element in DC equivalent circuit
R_3	Third resistive element in DC equivalent circuit
R_{bulk}	Bulk resistance
RC	Resistive and capacitive elements
R_{pol} or $R_{polarization}$	Polarization resistance
sccm	Standard cubic centimeters
SEM	Scanning electron microscopy
SOFC	Solid oxide fuel cell
t	time
TEY	Total electron yield
TPB	Three phase boundary
V	Observed voltage at any time
V’	Measured voltage at any time
V(ω,t)	Oscillating potential defined wave
V°	Set amplitude of oscillating potential
V’°	Measured amplitude of oscillating potential
V_{cell}	Observed voltage of SOFC
V-I	Voltage vs current plot
V_o^{2+}	Unfilled oxide vacancy
V_{ocv}	Open circuit voltage
V_{op}	Applied cell overpotential

XAS	.....	X-ray asorption spectroscopy
XPS	.....	X-ray photoelectron spectrscopy
XRD	.....	X-ray diffraction
YSZ	.....	Yttria stabilized zirconia
Z_{img}	.....	Imaginary component of impedance measurement
Z_{real}	.....	Real component of impedance plot
ω	.....	Frequency (EIS)
φ	.....	Phase angle
υ	.....	Frequency (Raman)
α	.....	Inherent Polarizability
σ_j	.....	Raman scattering cross section
ε	.....	Molar absorbtivity

Chapter 1: Introduction

1. Fuel Cells

1A. General Introduction

Increasing demands on a limited supply of fossil fuels have necessitated the need to find more efficient ways of utilizing these resources to produce electricity and power.[1,2] Renewable fuels have also begun to attract considerable attention as sustainable sources of energy that can be used both in traditional and emerging power producing systems.[3-23] The traditional mechanism of power production involves the combustion of a fuel and using PV-work to move pistons in engines or to turn turbines to produce energy.[1,2,24] These internal combustion systems typically operate with efficiencies no higher than 30 %, meaning that a large fraction of the energy released during fossil fuel combustion is lost in the form of heat.[1,2] At these low efficiencies, typical combustion engines are also creating significant amounts of CO, CO_2, NO_x, and SO_x air pollutants.[1,2,24-27]

Fuels cells (FC) have attracted considerable attention because of their ability to provide electricity cleanly and efficiently.[1,2,24] These alternative energy conversion devices can convert a wide variety of fuels into products and electricity with efficiencies as high as 80 % in combined heating and power applications.[1] Because these devices produce power electrochemically, they do not emit significant amounts of NO_x and SO_x pollutants.[1,2,24-27] Fuel cells can be distinguished by the type of electrolyte material used in a given device. The four main types of fuel cells and their

operating temperatures are: the 200˚C phosphoric acid fuel cell (PAFC), the 80˚C polymer electrolyte membrane fuel cell (PEMFC), the 650˚C molten carbonate fuel cell (MCFC), and the 650-1000˚C solid oxide fuel cell (SOFC).[1,28-30]

1B. Solid Oxide Fuel Cells

SOFCs consist of a solid oxide electrolyte and two electrodes: an anode and a cathode.[1,2,27,31](Figure I.1) The electrolyte is YSZ, a cubic zirconia lattice containing 5-15 mole % Y_2O_3.[1,2,32-46] Doping ZrO_2 with Y_2O_3 creates oxide ion vacancies that allow oxide ions to diffuse from the cathode through the electrolyte to the anode.[33-36,38-40,47,48] Anodes typically consist of porous electrocatalysts such as nickel-yttria stabilized zirconia (YSZ) ceramic-metallic (or cermet) composites. Mixed-valence, metal oxide materials represent an alternative class of candidate anode materials currently being investigated.[1,25,32,49-56] The cathode of an SOFC typically consists of an electrocatalytic material such as lanthanum strontium manganate (LSM) or a simple platinum mesh.[1,39,48,57] New cathode materials are being explored to alter or change the cations in the perovskite structure and to see the effect these changes will have on molecular oxygen activation, oxide migration and electrochemical performance.[48,57,58]

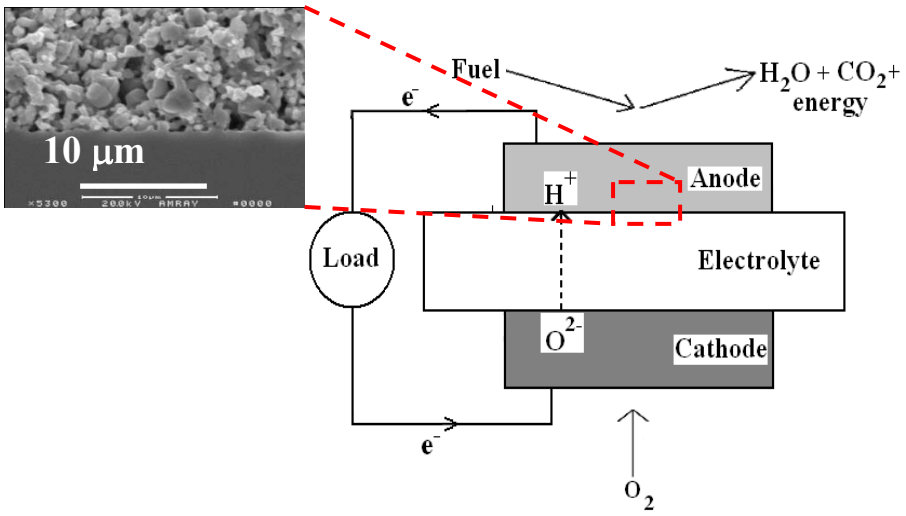

Figure I.1. Schematic of the construction of a planar electrolyte-supported SOFC with general reactions. Left inset is an SEM image showing the porous nature of the Ni/YSZ cermet anode along with the dense YSZ electrolyte.

SOFCs rely on the electrochemical oxidation of a fuel to provide an electrical current.[1,34,59-71] In the most general sense, the overall chemistry occurring in SOFCs converts a fuel into products and electricity in the presence of oxide ions that have already been electrochemically reduced.[1,24,59,60](Eq. 1) The oxide ions arrive at the anode after diffusing through vacancies in the YSZ matrix.[34,38-40,48] Oxidation of the fuel is thought to happen at the three phase boundary (TPB), the region where the ionically conducting electrolyte, the electronically conducting anode and the gas phase fuel mixture meet.[61,63,72-76](Eqs. 2a and b) At the TPB, electrons are carried away into the circuit and arrive at the cathode where they reduce the adsorbed O atoms to form O^{2-}, Eq. 3.[2,34,59,61] The general reactions that can take place at the TPB of SOFCS (with H_2 as the fuel) are shown in Figure I.2.[55] An important point to note, however, is that these proposed mechanisms are speculative and depend on a description of the TPB that is not experimentally validated. Reaction mechanisms become more numerous and complex with the hydrocarbon fuels.[77]

$$H_2 + CO + 2O^{2-} \rightarrow H_2O + CO_2 + \Delta E \quad \textbf{(Eq.1)}$$

$$H_2 + O^{2-} \rightarrow H_2O + 2e^- \quad \textbf{(Eq. 2a)}$$

$$CO + O^{2-} \rightarrow CO_2 + 2e^- \quad \textbf{(Eq. 2b)}$$

$$O_2 + 4e^- \rightarrow 2O^{2-} \quad \textbf{(Eq. 3)}$$

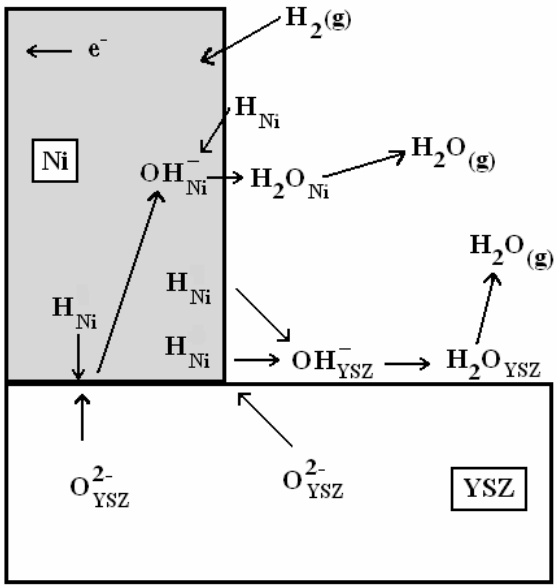

Figure I.2. Possible anode reactions occurring near the TPB of an SOFC operating with H_2 as the fuel source.[55]

1C. Advantages and Disadvantages of Solid Oxide Fuel Cells

SOFCs have distinct advantages over other types of fuel cells that afford SOFCs the best possibility of being adapted into widespread commercial applications.[2,11,27-30] The modular nature of these devices allow them to used either for stationary (250 kW, Siemens Westinghouse) or portable (50 W, Adaptive Materials Inc.) power production in stand-alone, small scale, or remote applications.[1,25-30] Also because of the simplicity to their design, SOFC can easily be

integrated into stack systems for more efficient, larger scale power production compared to other fuel cell systems.[1,28-30]

Unlike other fuel cell systems, that utilize liquid electrolytes, the electrolytes of SOFCs are solid allowing them to be configured into flexible geometries to suit the specific needs of an application.[1,28-30] Typical geometries include planar and tubular designs that can be adapted to a wide range of different shape, sizes, and configurations.[1,28-30] The dense, solid state composition of these electrolytes limits corrosion and degradation problems that occur with liquid electrolytes.[1,28-30]

SOFCs are characterized by their support layer, the thickest component, of the cell and the component that gives the membrane electrode assembly (MEA) its structural integrity.[58] These categories include anode, cathode and electrolyte supported designs. These different designs are possible because the electrolyte material is a dense non porous solid oxide material, and only needs to be strong and thick enough to be impermeable to gas diffusion, as thin as $\sim 10\ \mu m$.[58] The justification of having thin electrolytes and thicker electrodes is to limit the resistance associated with oxide migration through the electrolyte while also increasing the electrode surface area to improve fuel reactivity.[58] With careful design and construction, anode or cathode supported MEAs can significantly improve fuel utilization and overall cell performance.

The high activation energies required to drive oxide diffusion through the electrolyte (100 kJ/mol) and activate molecular oxygen at the cathode (223 kJ/mol) require that SOFCs operate at relatively high temperatures ($\geq 650^{\circ}C$).[31,78] The high temperature environments required for SOFC operation confer to them several

advantages over other low temperature FC systems. The high temperature conditions creates an environment that doesn't require an expensive catalyst and instead can be manufactured from relatively inexpensive materials such as Ni.[1,25,32,49-56] These catalysts show an improved tolerance toward some common fuel impurities relative to low temperature fuel cells, where trace amounts of CO can completely deactivate catalytic sites leading to rapid device failure.[1,28-30,79] High operating temperatures also give SOFCs fuel flexibility, enabling them to operate with a wide variety of different fuels (H_2, CO, alcohols, biofuels, and medium-sized hydrocarbons) directly and internally without the need for external fuel processing to convert hydrocarbon fuels into H_2 and CO_2, removing all trace amounts of CO.[1-13,24,25,27,79-86]

The high operating temperatures of SOFCs, although advantageous in some respects, also present many drawbacks. A major problem associated with SOFCs is in the need to use materials that are chemically and thermally compatible with each other.[1,30] At the elevated temperatures required for operation, a mismatch in electrolyte and electrode thermal expansion can lead to delamination of the electrodes from the electrolyte or electrolyte cracking that results in direct mixing of the fuel and oxidant.[1,30] Similar concerns surround the use of seals designed to isolate the anode and cathode chambers and interconnects that couple MEA components to external loads. When seals are exposed to the high temperature environment and for prolonged periods of fuel exposure they can become compromised leading to mixing of the anode and cathode gases.[1,30] Interconnects are on both the anode and cathode side, because of this, they will experience both oxidizing and reducing environments at extreme temperatures and therefore are required to be chemically stable.[1,30] To

prevent oxidation of the interconnect, a chromium layer is normally plated over the material.[1,30] At high temperatures, chromium can begin to volatilize depositing chromium throughout the electrode increasing ohmic resistances and decreasing catalytic activity.[1,30]

A final challenge presented by the high temperatures required for SOFC operation involves processes that occur in SOFCs operating with carbon containing fuels. The high operating temperatures of SOFCs allow for internal reforming of the hydrocarbon fuel ideally creating a mixture of CO and H_2.[19,53,81,87-89] However, the high temperatures of SOFCs can lead hydrocarbon fuels to pyrolyze and form graphitic carbon species that nucleate carbon growth on electrodes.[1,2,10,13,25,32,71,79,90-99] Carbon formation in SOFCs have been found to be a major contributor in overall device degradation by decreasing porosity, increasing fuel tortuosity, and blocking active anode catalysts.[1,2,10,13,25,32,71,79,90-99]

1D. Challenges

Despite decades of the extensive research exploring SOFC operation and performance, the molecular processes occurring on and near SOFC electrodes remain poorly characterized due to numerous technical challenges associated with carrying out molecularly specific, *in situ* measurements. Most of the challenges associated with SOFC research are related to the operational conditions and design of the devices themselves.[2,61,100] The normal operating temperature of a SOFC is usually no lower than 650˚C and can be as high as 1000˚C.[1,2,25,31,78] Furthermore, the device is normally fully enclosed and surrounded by a furnace to improve efficiency.[2,61,100] These high operating temperatures and inaccessible architectures make it extremely

difficult to validate proposed kinetic models because of lingering questions about the elementary reactions occurring on the surfaces of SOFC materials.

Current methods used to study these devices involve the use of standard voltammetry and electrochemical impedance methods.[55,101-103] These methods provide valuable information about changes in performance and operating conditions, but the techniques are intrinsically nonspecific and can not provide detailed information about the structural and chemical changes that are leading to these observed changes in electrochemical performance. *Ex situ* characterization methods are normally used in conjunction with *in situ* electrochemical experiments to provide information about the formation of chemical species or changes in material properties at the electrode that might have led to observed changes in performance that were observed while the SOFC was operating. *Ex situ* experiments can again provide valuable information, but since they are conducted after the device has been completely cooled and disassembled these studies can not provide a direct correlation between changes in electrochemical performance and specific chemical and material changes occurring in the SOFC.

Traditionally, most SOFC research has focused on improving efficiency and durability of the fuel cell by electrochemically testing systematically different anode and cathode materials.[1,25,32,39,48-58] The electrochemical data are then fit to kinetic models.[51,53,77,104] Most kinetic models use analytical expressions to interpret electrochemical data in terms of diffusion and reaction rate constants and electrochemical reversibility with respect to cell overpotential.[51,53,104] Ideally, accurate kinetic models would contain data that identified specific species present as

a function of operating conditions. Since the SOFC electrode surfaces are not generally amenable to examination by non-invasive techniques during operation, most information about device operation comes from *in situ* electrochemical analysis coupled with extensive *ex situ* characterization.

2. Goal of Research

The research described in this thesis overcomes the challenges associated with performing *in situ* studies of SOFC chemistry. This objective is accomplished by using a unique, custom built, electrochemical SOFC assembly that allows us to perform *in situ* Raman scattering experiments. A schematic description of the assembly appears in Appendix I. Experiments are performed at operational temperatures and measure changes in SOFC MEA structure and composition while correlating these observations with concurrent electrochemical experiments.

The goal of the research presented in this thesis, is to explore the chemical and material changes that are occurring with different SOFC elements *in situ* and in real time *while the device is operating* to correlate with changes in electrochemical performance. Specific questions this research will address are:

1) What -if any- role does YSZ play in the electrochemical oxidation of the fuel and charge conduction?
2) How do oxygenated fuels such as methanol and ethanol behave in SOFCs?

3) How will internal reforming of alkanes and alcohols affect overall electrochemical performance and carbon formation on the SOFC anode?

4) Can mechanisms of anode degradation and failure be correlated with the rate and type of carbon formation on SOFC anodes?

The SOFCs used in these efforts are electrolyte-supported MEAs. These MEAs consist of a dense yttria-stabilized zirconia (YSZ) electrolyte with a thickness of 0.80 ± 0.02 mm and a diameter of 25 mm. YSZ's composition consisted of 8 % Y_2O_3 (by mole fraction of Y relative to Zr). These electrolytes then have a ~ 30 μm thick porous cathode attached to them that is 50 % by weight of $(La_{0.8}Sr_{0.2})_{0.98}MnO_{3-x}$ to YSZ. Experiments that focused on studying the chemical and electronic properties of the YSZ electrolyte lacked an anode or utilized a non-catalytic patterned gold anode; these architectures are further discussed in chapters II and III. For experiments that focused on anode degradation brought upon by different fuel and/or fuel mixtures, a ~ 30 μm thick Ni/YSZ anode (50 % Ni by weight) was attached to electrolytes with previously constructed cathodes; these MEAs are describe in more detail in chapters IV, V, and VI. Unless stated otherwise, the temperatures of experiments described in this paper were performed at 715˚C with 8 mW excitation from a 488 nm Argon ion laser. The temperatures of these experiments were monitored by the peak position of YSZ which depends linearly on temperatures. Further explanation of YSZ peak migration and temperature dependence is presenting in Appendix II.

Experiments described in Chapters II and III investigated changes in chemical and electronic properties of YSZ when the material was exposed to anode-like conditions experienced in operating SOFCs. Experiments coupled *in situ* Raman data with lateral electrochemical impedance spectroscopy (EIS) measurements that examined what role -if any- surface reduced YSZ plays in electrochemical oxidation and charge transfer processes. The next set of experiments further explored the nature of the oxidized and surface reduced YSZ by coupling additional *in situ* Raman experiments with *ex situ* X-ray absorption spectroscopy (XAS) studies. These techniques were used to help identify compositional changes that resulted from exposure to reducing and oxidizing environments at high temperatures.

The goal of experiments investigating fuel chemistry in operating SOFCs was to observe the activity of different fuels and fuel mixtures during operation by monitoring graphite formation and correlating these observations with device electrochemical performance. The first sets of experiments, presented in Chapter IV, investigated the differences between SOFCs operating with either a direct alkane or alcohol fuel. Experimental techniques used included *in situ* Raman scattering, real time EIS, *in situ* near-infrared (NIR) thermal imaging, and *ex situ* Fourier-transform infrared (FTIR) spectroscopy exhaust measurements. Each individual technique provided its own perspective on processes occurring in SOFCs and when combined, provided a thorough understanding of SOFC chemistry. The spectroscopic experiments were expanded in scope to explore the chemistry occurring in SOFC when operated with alkane and alcohol fuels that undergo internal reforming with either oxygen or H_2O (Chapter V and VI).

Unlike traditional electrochemical measurements or *ex situ* analyses, the optical methods employed in this work provide real time, materials-specific *in situ* information about the chemistry occurring in operating SOFCs. Such data provide the quantitative benchmarks needed to test proposed models of electrochemical oxidation in these devices. More importantly, being able to differentiate mechanisms of SOFC operation as a function of fuel identity and cell polarization can help guide the development of new SOFC materials and architectures.

3. Technical Overview

3A. Explanation of Electrochemical Measurements

Two methods commonly used to characterize SOFC performance are electrochemical impedance spectroscopy (EIS) and linear sweep voltammetry (LSV). These techniques provide information about the resistive elements and electrochemical efficiencies of the cells. Conditions such as temperature, overpotential, and fuel identity will be varied to better understand how SOFCs convert reactants to products and generate electricity. These techniques will play valuable roles in the studies described in this thesis and complement the *in situ* optical measurements.

EIS is a technique that measures the frequency dependent impedance of materials, and the results are then associated with specific chemical processes such as charge and mass transfer.[105-107] Unlike a pure ohmic resistance, impedance can have both real and imaginary components where the real contribution attenuates voltage and the imaginary piece changes the phase.[105-107] Electrochemical impedance is measured by applying an oscillating potential, either across or through a material and

measuring the amplitude change and phase shift of the AC wave at a separate electrode.[105-107] By analyzing the frequency-dependent real and imaginary impedances from a through-cell EIS experiment, we can associate resistive or capacitive properties to corresponding materials.[105-107](Figure I.3) In an EIS experiment an oscillating wave (V(ω,t)), having a user defined amplitude (V˚) is applied to an electrode and the frequency of the wave is varied.[105-107] The response of the system is measured at the second electrode over a range of frequencies between 10^5-0.03 Hz. Data can be represented in two different formats: Nyquist and Bode plots.[105-107] The Nyquist plot will represent all the EIS data presented in this paper and therefore deserves further explanation.

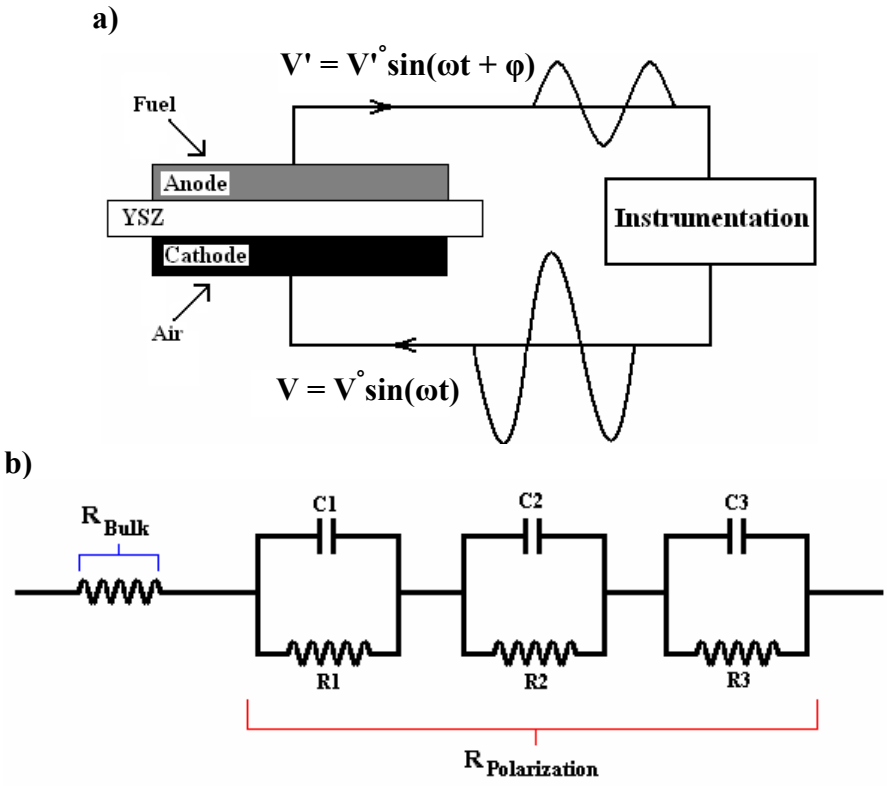

Figure I.3. a) Through cell EIS experiment set up b) circuit representation of the SOFC elements in part a.

The Nyquist plot correlates real impedance (resistance) vs. imaginary impedance (reactance or capacitance) over a range of AC frequencies.[105-107] When an oscillating AC wave is sent through a resistor, the current being measured is attenuated but not shifted in phase compared to the oscillating voltage.[105-107] The impedance associated with this property is real impedance, $Z_{Real} = R$ where "R" represents pure ohmic resistance.[105-107] When an oscillating potential wave is sent through a capacitor the current being measure is attenuated and shifted in phase by $\pi/2$.[105-107] The impedance associated with these characteristics is the imaginary impedance, represented by $Z_{Im} = X_C = 1/(2\pi\omega C)$, where X_C = the capacitive resistance, ω = frequency of AC wave, and C = pure capacitance.[105-107] The important data on a Nyquist plot are the bulk resistance (R_{bulk}), polarization resistance (R_{pol}), and resistance associated with the different processes taking place at the cathode and anode (R_1, R_2, R_3).[108](Figure I.4)

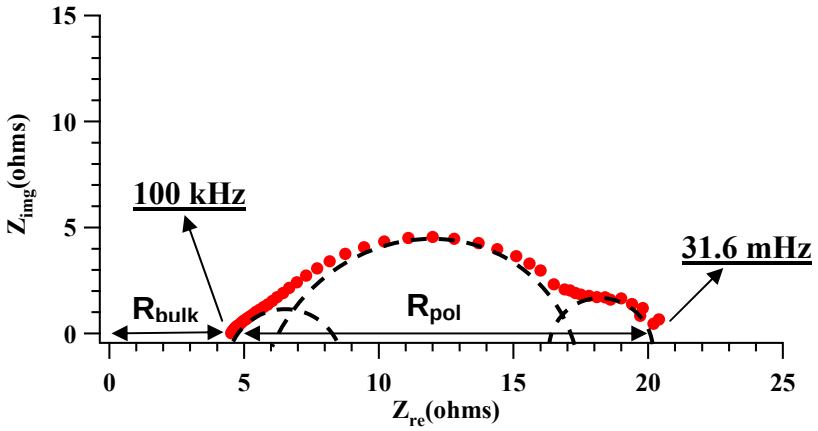

Figure I.4. Nyquist plot of a through-cell electrolyte-supported SOFC with porous Ni/YSZ anode and LSM cathode operating with direct methane at 715˚C. Spectrum exhibiting the high and low frequency regions along with R_{bulk} and R_{pol} and representative arcs associated with cathode and anode processes. Peak frequencies: ~ 63 Hz (high frequency arc), ~ 6.3 Hz (middle frequency arc), and ~ 320 mHz (low frequency arc)

EIS is a valuable technique when observing changes in overall electrochemical performance of SOFCs because the technique not only highlights changes in impedance but also can provide detailed information about specific mechanisms assigned to frequency dependent SOFC processes.[54,109] Information about SOFC processes can be seen in the different arcs (associated with different resistive and capacitive (RC) circuit elements) and the purely ohmic bulk resistance (R_{bulk}) exhibited in a typical EIS spectrum.[54,109] The high frequency x-intercept in a Nyquist plot is associated with R_{bulk}, the resistance assigned to mass transfer of oxides through the electrolyte. R_{bulk} has no capacitive contribution features but does depend on temperature.[54,109] For an electrolyte supported SOFC there are typically three different arcs associated with cathodic processes, and anodic processes.[54,109] From numerous experiments, we infer that the highest frequency arc, at low Z_{real} impedances, is associated with cathodic processes and remains unchanged from prolonged exposures to carbon containing fuels. Also from these experiments we observe that with the formation of graphite from prolonged exposures to these same fuels there is an increase in both impedance components in the middle and high frequency arcs inferring that these arcs are associated with anodic processes. The sum of the Z_{real} for these three arcs represent the polarization resistance (R_{pol}).[54,109]

LSV is an electrochemical technique that measures a change in cell voltage as a function of the current being drawn from the device.[105-107] LSV is an excellent method for studying the electrochemical performance of the SOFC as a function of operational conditions.[60] When no current is being drawn (overpotential = 0.0 V), open circuit voltage (OCV) is measured. OCV reflects a combination of the standard

reduction potentials of the reactions taking place on the anode and cathode.[105-107] LSV experiments apply an overpotential to the cell and measure the resulting current generated at the anode.[105-107] As overpotential is increased, more current is drawn and the overall cell potential drops.[105-107] When the electrochemical potential equals overpotential, there is no electromotive force driving charge through the circuit.[105-107] On a LSV plot, OCV holds a special significance as it represents a thermodynamic equilibrium between reactants and products and establishes an upper limit the amount of electrochemical energy the cell can produce.[105-107](Figure I.5) Another important feature of these plots is that maximum current and power information can be determined (right axis).

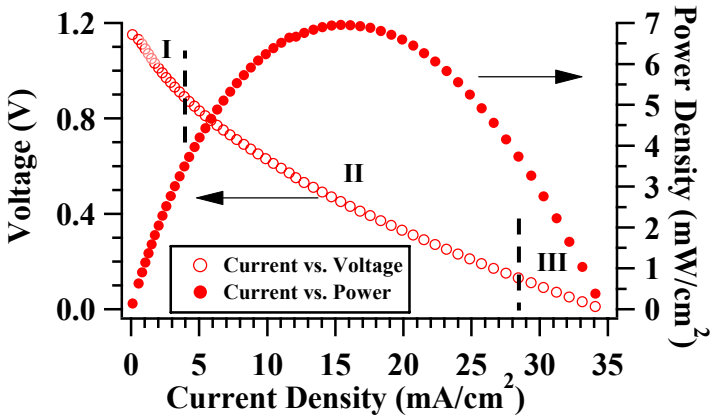

Figure I.5. Through-cell LSV plot taken at 715˚C with H_2 diluted in argon as the fuel source. Current density vs. voltage is represented by left axis while current density vs. power density is represented by right axis. Three distinct regions (I, II, III) marked off by dashed lines are associated with different SOFC processes.

When the SOFC is connected to an external load, a potential is created through electrochemical reactions.[109] The cell potential can be reduced by irreversible voltage losses that are associated with current dependent SOFC processes.[109] In a typical V-I plot there are three distinct regions, each reflecting

these different, current dependent SOFC processes.[109] These regions are associated with overpotentials requiring for overcoming activation (region I), ohmic resistance losses (region II), and changes in concentration (region III).[109] Region I is associated with activation overpotentials is related to the energy needed to drive reactions responsible for fuel oxidation at the anode and oxygen reduction at the cathode.[109] Ohmic resistance losses shown in region II are directly related to the oxide ion migrating from the cathode to the anode through the electrolyte.[109] Finally, changes in the overpotential exhibited in region III by a depletion of the reactants at either the cathode and anode brought upon by low flow rates and/or slow diffusion through a dense electrode.[109]

3B. Explanation of *In Situ* Raman Spectroscopic Measurements

Raman spectroscopy is a technique used to study the vibrational structure of molecules and materials. This technique is especially effective at measuring the frequencies of low frequency vibrational and phonon modes.[110-112] In a Raman experiment, a sample is typically irradiated with laser radiation in the visible or near infrared region of the spectrum.[110-112] When the sample is irradiated, the incident electromagnetic field interacts with the charged particles (nuclei and electrons) of a molecule or material causing the incoming photons to be scattered.[110-112] Only vibrations that can change the polarizability of the molecule or material can produce Raman scattering.[110-112] The observed intensity of Raman scattered photon is $I_R = I_o\sigma_j n$. Where "I_o" is the laser intensity, "σ_j" is the Raman scattering cross section of a particular vibration, "n" is the number of molecules present in the sample.[110-112]

The magnitude of σ_j is related $\delta\alpha/\delta Q_j$ where α is the inherent polarizability and Q_j is a specific vibrational mode being excited.[110-112]

Photons can be scattered in one of three ways. Rayleigh scattered photons have the same frequency ($E = h\nu$) as the incoming radiation but travel in different directions.[110-112] Photons that are Stokes and Anti-Stokes scattered change the vibrational state by either $\Delta v = +1$ (Stokes) or $\Delta v = -1$ (anti-Stokes).[110-112] When a photon is Stokes scattered, some energy from the incoming photon is transferred to the molecule or material leaving the sample in an excited vibrational state ($-\Delta E$). The result of this energy transfer is that the scattered photon has a lower frequency (or longer wavelength) compared to the initial incoming light or Rayleigh photons.[110-112] When a photon is Anti-Stokes scattered, vibrational energy from the molecule or material in a higher vibrational state ($v \geq 1$) is transferred to the incoming photon producing a new photon having a higher frequency (or shorter wavelength) compared to the initial incoming light or Rayleigh photons ($+\Delta E$).[110-112] The stokes scattering mechanism is illustrated schematically in Figure I.6. Spectra in this thesis are collected using Stokes scattered light because of the higher ground state vibrational populations *and* because of instrumental limitations. The Stokes-scattered signal is collected and sent through a monochromator/filter assembly that blocks light at the incident excitation and anti-Stokes frequency.

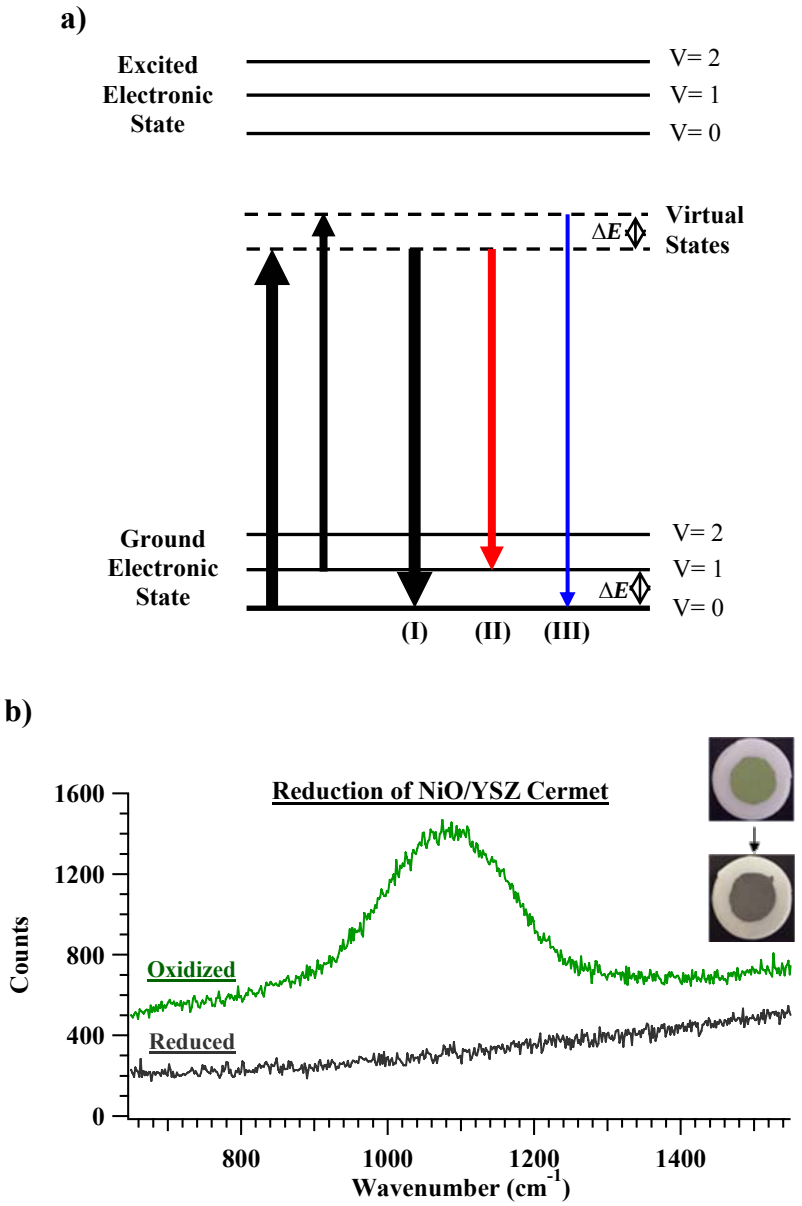

Figure I.6. a) Energy level diagram representing Rayleigh (I) and Stokes (II) and Anti-Stokes (III) Raman scattering. b) *In situ* Raman spectra taken at 715˚C of an oxidized NiO/YSZ anode that has been reduced to Ni/YSZ with H_2 diluted with argon during operation. Raman spectra of NiO 2LO second order band. Inset in b) shows an actual oxidized and reduced anode.

3C. Explanation of *Ex Situ* Measurements

Some experimentation presented in this thesis required the use *ex situ* FTIR spectroscopy to quantify the chemical composition of the fuel reaching the anode. In

FTIR spectroscopy, absorbances are observed if vibrational motion causes changes in the molecule's dipole.[112] For experiments presented in this thesis, IR absorbance was used to obtain a Beer's law analysis of the chemical composition of the gas phase reacting at the anode.[113] The equation used in these measurements was $A = \varepsilon CL$: where A is the IR absorbance measured by the molar absorbtivity (ε) and the concentration(C) of the molecule(s) being studied, and the sample path length (L).[113]

4. Organization

The organization of this thesis is as follows: Chapter II utilizes experiments that employ *in situ* Raman spectroscopy and lateral EIS measurements to characterize the properties of an YSZ electrolyte under electrochemical potential control. Experiments measure changes in YSZ surface chemistry as a function of through-cell overpotential, and experiments are designed to identify what role -if any- surface reduce YSZ plays in electrochemical oxidation and charge transfer. Raman spectra show that the change in YSZ, from fully oxidized to surface reduced, is reversible and happens on a timescale of minutes at temperatures above 700˚C. Spatially resolved Raman experiments carried out with polarized cells show that oxide ion concentration near the TPB of the anode is depleted even further when an overpotential is applied. The change in relative oxide concentration with respect to overpotential is also a reversible process. EIS measurements, probing lateral impedance across the electrolyte surface, show that the surface reduced YSZ phase has a lower R_{pol} as through-cell overpotential increases. Results are discussed in terms of reduced resistances to processes involving charge and mass transfer reactions specific to the reduced YSZ surface states.

Chapter III explores further the chemical composition of YSZ by coupling *in situ* Raman spectroscopy with *ex situ* XAS measurements performed by collaborators at Montana State University. To understand the origins of the observations from Chapter II, *ex situ* XAS analyses were performed with freshly reduced YSZ samples that had been cooled to room temperature under inert conditions. The XAS experiments show that the reduced YSZ samples have a higher zirconium M_4/M_5 branching ratio when compared to oxidized YSZ and correlates with an increase in oxide vacancies and electron density at the YSZ surface. Similar measurements were performed on the yttrium $L_{2,3}$ edge, and no change was observed between the oxidized and reduced YSZ samples. This is strong evidence that yttrium does not play a significant role in the formation of conductive surface states of reduced YSZ.

Chapter IV uses vibrational Raman scattering and NIR imaging to measure the susceptibility of Ni/YSZ cermet anodes to carbon formation in operating SOFCs with direct methane and methanol fuels. The imaging experiments were performed by collaborators at the Naval Research Laboratory. Imaging and spectroscopic data show that when the cell is held at OCV, carbon forms within one minute of methanol or methane being introduced into the anode chamber. We note that the formation of graphite will depend on operating conditions including temperature, fuel residence time and Ni loading. Raman spectra identify these deposits as highly ordered graphite based on a single sharp feature in the vibrational spectrum near 1580 cm^{-1}. While graphite formed from methane remains highly ordered regardless of exposure duration, graphite formed from sustained exposure to methanol begins to show

evidence of structural disorder inferred from the appearance of a weak feature at 1340 cm^{-1}. Correlating the growth of the intensity in the Raman spectra with exposure time quantifies the kinetics of carbon deposition and suggests that carbon formed from methanol grows via two distinct mechanisms. Thermal imaging data show that the formation of carbon deposits is an endothermic process and reduces anode temperature. This effect is more pronounced with methanol than methane. These results agree with data from vibrational Raman experiments showing that exposure to methanol leads to significant more carbon depositions. Polarizing the cell reduces the amount of carbon deposited. The effects of the graphite formed from methanol are evident in the EIS data. In contrast, graphite formed from methane only modestly affects device performance.

Chapter V investigates the internal oxidative and steam reforming of methane in operating SOFCs by correlating *in situ* Raman measurements with concurrent EIS measurements. Data show that a direct methane fuel feed leads to anode degradation brought upon by highly ordered graphite formations. *Ex situ* FTIR measurements revealed that oxidative reforming of methane creates a combination of CO and CO_2 but steam reforming converts CH_4 to CO with no observable CO_2. *In situ* Raman measurements showed that carbon formations could be completely suppressed in the presence of both reformers, although EIS data from oxidatively reformed CH_4 contained much more scatter than data acquired using steam reformed CH_4. Additional Raman measurements revealed that O_2 was capable of oxidizing the Ni catalyst in the SOFC while H_2O was not, suggesting that fluctuations in the scatter in

the EIS data resulted from microscopic, reversible oxidation and reduction of the anode catalyst.

Chapter VI explains the observations of using direct and humidified ethanol in operating SOFCs. In cells operating with direct ethanol (diluted in argon), graphite forms rapidly and the Ni/YSZ anode suffers irreversible structural degradation. With humidified ethanol, degradation is minimized in cells at OCV and completely suppressed in polarized ells. The tendency of ethanol to form graphite and the stability of the cermet anode is tied directly to the composition of the fuel mixture that reaches the anode. *Ex situ* FTIR analysis of the SOFC fuel effluent shows humidifying the ethanol fuel lead to less acetylene, carbon monoxide, and methane formation when compared to the direct ethanol fuel. These fuel species have been found to be precursors to carbon formation and therefore device degradation explaining the rapid degradation observed with the direct fuel and minimal degradation observed with the humidified fuel.

Chapters II through VI are all modified versions of manuscripts that have either appeared in press (Chapters IV and VI), have been submitted for peer-review (Chapter II), or are in preparation for submission (Chapters III and V). Because of this, there will be some redundancy throughout the thesis, especially in the introductory and experimental sections of each chapter. Some results displayed in the chapters were possible through the work of collaborating authors (Chapters III and IV). These contributions are explained further in Appendix III.

5. References

(1) Ormerod, R. *Chem. Soc. Rev.*, **2003**, *32*, 17.

(2) Song, C. *Catal. Today*, **2002**, *77*, 17.

(3) Brett, D.; Atkinson, A.; Brandon, N.; Skinner, S. *Chem. Soc. Rev.*, **2008**, *37*, 1568.

(4) Kendall, K. *Int. Mater. Rev.*, **2005**, *50*, 257.

(5) Mogensen, M.; Kammer, K. *Annual Rev. Mater. Res.*, **2003**, *33*, 321.

(6) Gorte, R.; Park, S.; Vohs, J.; Wang, C. *Adv. Mater.*, **2000**, *12*, 1465.

(7) Gorte, R.; Kim, H.; Vohs, J. *J. Power Sources*, **2002**, *106*, 10.

(8) Kee, R. Zhu, H.; Goodwin, D. *Proc. Combust. Inst.*, **2005**, *20*, 2379.

(9) Liu, J. *Prog. Chem.*, **2006**, *18*, 1026.

(10) McIntosh, S.; He, H.; Lee, S.; Costa-Nunes, O.; Krishnan, V.; Vohs, J.; Gorte, R. *J. Electrochem. Soc.*, **2004**, *151*, A604.

(11) Pomfret, M.; Marda, J.; Jackson, G.; Eichhorn, B.; Dean, A.; Walker, R. *J. Phys. Chem. C*, **2008**, *112*, 5232.

(12) Randolph, K.; Dean, A. *Phys. Chem. Chem. Phys.*, **2007**, *9*, 4245.

(13) Coutelieris, F.; Douvartzides, S.; Tsiakaras, P. *J. Power Sources*, **2003**, *123*, 200.

(14) Assabumrungrat, S.; Sangtonkitcharoen, W.; Laosiripojana, N.; Arpornwichanop, A.; Charojrochkul, S.; Praserthdam, P. *J. Power Sources*, **2005**, *148*, 18.

(15) Cimenti, M.; Hill, J. *J. Power Sources*, **2010**, *195*, 3996.

(16) Cimenti, M.; Hill, J. *J. Power Sources*, **2010**, *195*, 54.

(17) Liu, M.; Peng, R.; Dond, D.; Gao, J.; Liu, X.; Meng, G. *J. Power Sources*, **2008**, *185*, 188.

(18) Kim, T.; Ahn, K.; Vohs, J.; Gorte, R. *J. Power Sources*, **2007**, *164*, 42.

(19) Laosiripojana, N.; Assabumrungrat, S. *J. Power Sources*, **2007**, *163*, 943.

(20) Jiang, Y.; Virkar, A. *J. Electrochem. Soc.*, **2001**, *148*, A706.

(21) Mat, M.; Liu, X.; Zhu, Z.; Zhu, B. *Int. J. Hydrogen Energy*, **2007**, *32*, 796.

(22) Cimenti, M.; Hill, J. *J. Power Sources*, **2009**, *186*, 377.

(23) Brett, D.; Atkinson, A.; Cumming, D.; Rameriz-Cabrera, E.; Rudkin, R.; Brandon, N. *Chem. Eng. Sci.*, **2005**, *60*, 5649.

(24) Pomfret, M.; Demircan, O.; Sukeshini, A.; Walker, R. *Environ. Sci. Technol.*, **2006**, *40*, 5574.

(25) Atkinson, A.; Barnett, S.; Gorte, R.; Irvine, J.; Mcevoy, A.; Mogenson, M.; Singhal, S.; Vohs, J. *Nat. Mat.*, **2004**, *3*, 17.

(26) Jacobson, M.; Colella, W.; Golden, D. *Science*, **2005**, *308*, 1901.

(27) Minh, N. *Solid State Ionics*, **2004**, *174*, 271.

(28) Appleby, A. *J. Power Sources*, **1996**, *69*, 153.

(29) Bedringas, K.; Ertesvag, I.; Byggstoyl, S.; Magnussen, B. *Energy*, **1997**, *22*, 403.

(30) Hirschenhofer, J. *IEEE AES Systems Magazine*, **1997**, *12*, 23.

(31) Goodenough, J. *Annu. Rev. Mater. Res.*, **2003**, *33*, 91.

(32) Zhu, W.; Deevi, S. *Mater. Sci. Eng. A.*, **2003**, *362*, 228.

(33) Feinberg, A.; Perry, C. *J. Phys. Chem. Solids*, **1981**, *42*, 513.

(34) Pomfret, M.; Stoltz, C.; Varughese, B.; Walker, R. *Anal. Chem.*, **2005**, *77*, 1791.

(35) Perry, C.; Fienberg, A.; Currat, R. *Bull. Amer. Phys. Soc.*, **1981**, *26*, 405.

(36) Perry, C.; Fienberg, A. *Solid State Commun*, **1980**, *36*, 519.

(37) Hattori, M.; Takeda, Y.;Sakaki, Y.; Nakanishi, A.; Ohara, S.; Mukai, K.; Lee, J.; Fukui, T. *J. Power Sources*, **2004**, *126*, 23.

(38) Swider, K; Worrell, W. *J. Electrochem. Soc.*, **1996**, *143*, 3706.

(39) Sammes, N.; Cai, Z. *Solid State Ionics*, **1997**, *100*, 39.

(40) Lee, J.; Yoon, S.; Kim, B.; Kim, J.; Lee, H.; Song, H. *Solid State Ionics*, **1997**, *144*, 175.

(41) Ishihara, T: Yan, J.; Shinagawa, M.; Matsumoto, H. *Electrochim. Acta.*, **2006**, *52*, 1645.

(42) Nesaraj, A.: Kumar, M.; Raj, I.; radhakrishna, I.; Pattabiraman, R. *Iranian Chem. Soc.*, **2007**, *4*, 89.

(43) Rupp, J; Drobek, T.; Rossi, A.; Gauckler, L. *J. Chem. Mater.*, **2007**, *435*, 795.

(44) Shao, Z.; Haile, S.; Ahn, J.; Ronney, P.; Zhan, Z.; Barnett, S. *Nature*, **2005**, *435*, 795.

(45) Wang, C.; Xui, L.; Tang, W. *Rare Metal Mater. Eng.*, **2006**, *35*, 501.

(46) Zhang, X.; Robertson, M.; Deces-Petit, C.; Qu, W.; Kesler, O.; Maric, R.; Ghosh, D. *J. Power Sources*, **2007**, *164*, 668.

(47) Vernoux, P.; Guth, M.; Li, X. *Electrochem. Solid State Lett.*, **2009**, *12*, E9.

(48) Svensson, A.; Sunde, S.; Nisancioglu, K. *J. Electrochem. Soc.*, **1998**, *145*, 1390.

(49) Qiao, J.; Sun, K.; Zhang, N.; Sun, B.; Kong, J.; Zhou, D. *J. Power Sources*, **2007**, *169*, 253.

(50) Rossmeisl, J.; Bessler, W. *Solid State Ionics*, **2008**, *178*, 1694.

(51) Decaluwe, S.; Zhu, H.; Kee, R.; Jackson, G. *J. Electrochem. Soc.*, **2008**, *155*, B538.

(52) Kakac, S.; Pramuanjaroenkij, A.; Zhou, X. *Int. J. Hydrogen Energy*, **2007**, *32*, 761.

(53) Zhu, H.; Kee, R. *J. Electrochem. Soc.*, **2006**, *153*, A1765.

(54) Bieberle, A.; Gauckler, L. *Solid State Ionics*, **2000**, *135*, 337.

(55) Bieberle, A; Meier, L.; Gauckler, L. *J. Electrochem. Soc.*, **2001**, *148*, A646.

(56) Sukeshini, A.; Habibzadeh, B.; Becker, B.; Stoltz, C.; Eichhorn, B.; Jackson, G. *J. Electrochem. Soc.*, **2006**, *153*, A705.

(57) Lin, Y.; Barnett, S. *Solid State Ionics*, **2008**, *179*, 420.

(58) Mertens, J.; Haanappel, V.; Tropartz, C.; Herzhof, W.; Buchkremer, H. *J. Fuel Cell Sci. Tech.*, **2006**, *3*, 125.

(59) Zhu, H.; Kee, R.; Janardhanan, V.; Deutschmann, O.; Goodwin, D. *J. Electrochem. Soc.*, **2005**, *152*, A2427.

(60) Pomfret, M.; Owrutsky, J.; Walker, R. *Anal. Chem.*, **2007**, *79*, 2367.

(61) Nielsen, J.; Jocobsen, T. *Solid State Ionics*, **2008**, *178*, 1769.

(62) Bove, R.; Ubertini, S.; *J. Power Sources*, **2006**, *159*, 543.

(63) Funkunaga, H.; Ihara, M.; Sakaki, K.; Yamada, K. *Solid State Ionics*, **1996**, *86-88*, 1179.

(64) Nam, J.; Jeon, D. *Electrochim, Acta*, **2006**, *51*, 3446.

(65) Feng, B.; Wang, C.; Zhu, B. *Electrochem. Solid State Lett.*, **2006**, *9*, A80.

(66) Hirabayashi, D; Hasimoto, A.; Hibino, T.; Harda, U.; Sano, M. *Electrochem. Solid State Lett.*, **2004**, *7*, A108.

(67) Ihara, M.; Hasegawa, S. *J. Electrochem. Soc.*, **2006**, *153*, A1544.

(68) Lin, Y.; Zhan, Z.; Liu, J.; Barnett, S. *Solid State Ionics*, **2005**, *176*, 1827.

(69) Nabae, Y.; Yamanaka, I.; Hatano, M.; Otsuka, K. *J. Electrochem. Soc.*, **2006**, *153*, A140.

(70) Sin, A; Kopin, E.; Dubitsky, Y.; Zaopo, A.; Arico, A.; la Rosa, D.; Antonucci, V. *J. Power Sources*, **2007**, *164*, 300.

(71) Walters, K.; Dean, A.; Zhu, H.; Kee, R. *J. Power Sources*, **2003**, *123*, 182.

(72) Martinez, A.; Brouwer, J. *J. Power Sources*, **2010**, *195*, 7268.

(73) Kenney, B.; Valdmanis, M.; Baker, C.; Pharoah, J.; Karan, K. *J. Power Sources*, **2009**, *189*, 1051.

(74) Janardhanan, V.; Heuveline, Deutschmann, O. *J. Power Sources*, **2008**, *178*, 368.

(75) Zhu, W.; Ding, D.; Xia, C. *Electrochem. Solid State Lett.*, **2008**, *11*, B83.

(76) Schmidt, M.; Hansen, K.; Norrman, K.; Mogensen, M. *Solid State Ionics*, **2009**, *180*, 431.

(77) Huayang, Z.; Kee, R.; Janardhanan, V.; Duetschmann, D.; Goodwin, D. *J. Electrochem. Soc.*, **2005**, *152*, A2427.

(78) Devanathan, R.; Weber, W.; Singhal, S.; Gale, J. *Solid State Ionics*, **2006**, *177*, 1251.

(79) McIntosh, S.; Vohs, J.; Gorte, R. *J. Electrochem. Soc.*, **2003**, *150*, A470.

(80) Douvartzides, S.; Coutelieris, F.; Demin, K.; Tsiakaras, P. *AlChE J.*, **2003**, *49*, 248.

(81) Iida, T.; kawano, M.; Matsui, T.; Kikuchi, R.; Eguchi, K. *J. Electrochem. Soc.*, **2007**, *154*, B234.

(82) Tanaka, Y.; Nguyen, T. ; Kato, T.; Shimada, T.; Sugano. K.; Negishhi, A.; Kato, K.; Nozaki, K. *Solid State Ionics*, **2006**, *177*, 3323.

(83) Ye, X.; Huang, B.; Wang, S.; Wang, Z.; Xiong, L.; Wen, T. *J. Power Sources*, **2007**, *164*, 203.

(84) Zhan, Z.; Barnett, S. *Solid State Ionics*, **2005**, *176*, 871.

(85) Zhan, Z.; Barnett, S. *Science*, **2005**, *308*, 844.

(86) Zhu, W.; Xia, C.; Fan, J.; Peng, R.; Meng, G. *J. Power Sources*, **2006**, *160*, 897.

(87) Faungnawakij, K.; Kikuchi, R.; Eguchi, K. *J. Power Sources*, **2007**, *164*, 73.

(88) Goula, G.; Kiousis, V.; Nalbandian, L.; Yentekakis, I. *Solid State Ionics*, **2006**, *177*, 2119.

(89) Liu, D.; Krumpelt, M.; Chien, H.; Sheen, S. *J. Mater. Eng. Perform.*, **2006**, *15*, 442.

(90) Sun, C.; Stimming, U. *J. Power Sources*, **2007**, *171*, 247.

(91) Pomfret, M.; Steinhurst, D.; Kidwell, D.; Owrutsky, J. *J. Power Sources*, **2010**, *195*, 257.

(92) Dokmaingam, P; Assabumrungrat, S.; Soottitantawat, A.; Laosiripojana, N. *J. Power Sources*, **2010**, *171*, 69.

(93) Nikooyeh, K.; Jeje, A.; Hill, J. *J. Power Sources*, **2007**, *171*, 601.

(94) Rakass, S.; Oudghiri-Hassani, H.; Rowntree, P.; Abatzoglou, N. *J. Power Sources*, **2006**, *158*, 485.

(95) Suwanwarangkul, R.; Croiset, E.; Entchev. E.; Charojrochkul, S.; Pritker, M.; Fowler, M.; Douglas, P.; Chewathanakup, S.; Mahaudom, H. *J. Power Sources*, **2006**, *161*, 308.

(96) Macek, J.; Novosel, B.; Marinnsek, M. *J. Eur. Ceram. Soc.*, **2007**, *27*, 487.

(97) Norinaga, K.; Dutschmann, O. *Ind. Eng. Chem. Res.*, **2007**, *46*, 3547.

(98) Holtappels, P.; De Haart, L.; Stimming, U.; Vinke, I.; Mogensen, M. *J. Appl. Electrochem.*, **1999**, *29*, 561.

(99) Sheng, C.; Dean, A. *J. Phys. Chem. A*, **2004**, *108*, 3772.

(100) Pomfret, M.; Owrutsky, J.; Walker, R. *J. Phys. Chem. B*, **2006**, *110*, 17305.

(101) Bebelis, S.; Neophytides, S. *Solid State Ionics*, **2002**, *152-153*, 447.

(102) Bieberle, A.; Meier, L.; Gauckler, L. *Solid State Ionics*, **2002**, *146*, 23.

(103) Sundes, S. *Electrochim. Acta.*, **1997**, *42*, 2637.

(104) Mandin, P.; Bernay, C.; Tran-Dac, S.; Broto, A.; Abes, D.; Cassir, M. *Fuel Cells*, **2006**, *6*, 71.

(105) Simpson, R., *Introductory Electronics for Scientist and Engineers*, ISBN 0205083773, Allyn and Bacon, Inc.

(106) Wang, J., *Analytical Electrochemistry*, ISBN 0-471-67879-1, John Wiley & Sons

(107) Bard, A.; Faulkner, L., *Electrochemical Methods: Fundamentals and Applications*, ISBN 978-0-471-04372-0, John Wiley & Sons

(108) Bessler, W. *Solid State Ionics*, **2005**, *176*, 997.

(109) Hofmann, P.; Panopoulos, K. *J. Power Sources*, **2010**, *195*, 5320.

(110) Ingle, J.; Crouch, S., *Spectrochemical Analysis*, ISBN 0-13-826876-2, Prentice-Hall

(111) McCreery, R., *Raman Spectroscopy for Chemical Analysis*, ISBN 0471252875, John Wiley & Sons

(112) Skoog, D.; Holler, F.; Nieman, T., *Principles of Instrumental Analysis*, ISBN 0-03-002078-6, Saunders College Publishing

(113) Harris, D.; Bertolucci, M., *Symmetry and Spectroscopy: An Introduction to Vibrational and Electronic Spectroscopy*, ISBN 0-486-66144-X, Dover Publications.

Chapter 2: High Temperature Mapping of Surface Electrolyte Oxide Concentration in Solid Oxide Fuel Cells with Raman Spectroscopy

1. Introduction

Solid oxide fuel cells (SOFCs) are devices that can produce DC electricity efficiently from a variety of different fuels. Commercially deployed SOFCs can range in size from very small (50 W, Adaptive Materials Inc.) to very large (250 kW, Siemens Westinghouse), and these devices can use a wide variety of fuels including *syn*-gas, H_2, liquified natural gas, bio-derived fuels, and traditional fossil fuels.[1-5] The actual fuel cell membrane electrode assembly (MEA) consists of three principle components: the cathode, the anode, and the solid oxide electrolyte.[2,4,6] The cathode and the anode are typically electrocatalytic and drive the reduction of molecular oxygen (to form oxide anions) and the oxidation of fuel (to form H_2O and CO_2), respectively.[7,8] The role of the solid oxide electrolyte is to transport oxide anions from the cathode to the anode.[9-16] Consequently, the electrolyte plays a vital role in SOFC operation by setting an upper limit to the amount of current that can be drawn from the device. The figures of merit for solid oxide electrolytes include high oxide conductivities, thermal stability, and large resistances to electron conduction.[9,17-26]

The most common electrolyte used in SOFC designs is yttria stabilized zirconia (YSZ). This mixed solid oxide consists of a fluorite ZrO_2 lattice doped with ~ 8–12 % Y_2O_3 (by mole fraction).[14,15,27] In the YSZ crystal lattice, one equivalence of Y_2O_3 replaces two equivalences of ZrO_2 leaving behind an oxide vacancy. These

oxide vacancies are distributed through the crystal lattice and are responsible for the material's oxide conducting capability.[14,17,27] The relatively high, ~ 100 kJ/mole activation energy to oxide diffusion through the electrolyte is one of the reasons that SOFCs must operate at high temperatures (> 650˚C) to maintain an efficient oxide flux to the anode.[28,29] These high temperature conditions raise challenges for studying the chemistry occurring in SOFCs by limiting the methods that can probe with molecular specificity the electrochemical processes occurring *in situ* and in real time. Experiments described in this work represent the first correlation between spatially resolved, *in situ* spectroscopic studies of SOFCs operating under steady state conditions and traditional electrochemical measurements that probe overall device performance.

Despite YSZ's importance in enabling oxide diffusion, potential roles that YSZ may play in promoting electrochemical activity have remained largely unexplored.[30,31] Kinetic models describing chemistry in SOFCs define the electrochemically active region in terms of a three phase boundary (TPB), the junction of the electron conducting anode, the oxide anion conducting electrolyte and the gas phase fuel mix.[30,32-36] The ideal TPB of an SOFC is defined as a 1-dimensional line although most models will assign this region a finite width that is on the order of tens of nanometers.[30,32-36] In reality, experimentally validating *in situ* length scales over which material properties are affected in operational SOFCs is very difficult. For example there are many variables that can change the length scale of the TPB such as overpotential, temperature, anode microstructure, and partial pressures of fuels.[37,38] Absent in all of this work is any consideration of how the

properties of YSZ are influenced by the high temperatures and strongly oxidizing and reducing conditions found in SOFCs. Reduced YSZ has been shown to be an efficient catalyst in the reforming of hydrocarbons,[39,40] thus the surface condition of YSZ in operating devices, especially near the anode, deserves examination when modeling fuel oxidation processes and spillover chemistry.

Recent reports suggest that the surface chemistry of YSZ can change under conditions commonly encountered in operating SOFCs.[15,24,41-43] *Ex situ* studies found that heating an YSZ sample to 800˚C in a reducing atmosphere and then cooling the sample back down to room temperature resulted in a surface reduced phase of YSZ that was stable at ambient temperatures and atmospheres.[15] Data discussed below show how spatially resolved, relative oxide ion surface concentrations can be inferred using *in situ* vibrational Raman scattering. The surprising result is that increasing overpotential depletes oxide concentration over μm-length distances from the anode. Simultaneous EIS measurements show that this additional net reduction in surface oxide concentration changes the electrochemical properties of the electrolyte and facilitates charge conduction laterally across the YSZ surface.

2. Experimental

2A. SOFC Membrane Electrode Assembly

The electrolyte supported membrane electrode assemblies (MEAs) used in these experiments are similar to those used in previous studies.[44-47] The button cell design consisted of a ~ 30 μm thick sintered LSM/YSZ (50 % LSM by mass) cermet cathode, an 8 % YSZ electrolyte (2.5 cm diameter, 0.8 mm thick) and a patterned gold anode. Details regarding the actual construction of these devices has been

discussed previously.[44-47] Platinum paste (Heraeus) was used to attach platinum mesh (Alfa Aesar) and a gold wire (Alfa Aesar) to the cathode as a current collector while gold paste (Heraeus) and gold wire were used to construct the four-patch anode design. Au was chosen so that the anode was electrochemically inert. Using traditional electrocatalytic materials (such as Ni) ran the risk of obscuring changes in surface electrolyte properties with anode material transformation (such as Ni oxidation and/or NiO reduction). The dimensions of these anode patches were 3 mm x 4 mm x 30 μm. Separating the patches was a 4 mm x 4 mm open area on the YSZ electrolyte. The majority of the experiments discussed in this paper are focused on the spectroscopic and electrochemical properties across this open area of the electrolyte. A schematic diagram is shown in Figure II.1.

2B. *In Situ* Raman Assembly

The complete SOFC assembly has been described previously.[44-46] A distinguishing difference of the devices used in these studies from more traditional button cell designs is the quartz optical window that allows vibrational Raman scattering experiments to focus 488 nm light onto the anode and detect the back scattered signal with a microscope/CCD assembly (InVia, Renishaw). All experiments conducted with the Raman spectrometer used 8 mW of 488 nm light, and all experiments were carried out at a temperature of 715 ± 2˚C. Gas flows to both sides of the MEA were controlled by rotameters. The anode was exposed to a 100 sccm H_2/100 sccm Ar mixture, while the cathode was exposed to 115 sccm of air. Experiments were also performed using humidified conditions where the gases were

passed through a H_2O bubbler, before reaching the anode, creating a 3 % humidified fuel feed.

All electrochemical measurements were made with a Gamry PCI4 Potentiostat/Galvanostat/ZRA instrument. During surface impedance measurements, the potentiostat polarized the SOFC to well-defined overpotentials with respect to open circuit voltage (OCV). OCV (with H_2 as the fuel) typically measured 1.15 ± 0.05 V, and the overpotentials used in these experiments were 0.0375, 0.075, 0.15, 0.225, 0.30, and 0.60 V. Here, overpotential refers to the difference between OCV and the voltage across the operating cell ($V_{op} = V_{OCV} - V_{cell}$). Prior to acquiring electrochemical and spectroscopic data, the SOFC operated with a specific overpotential applied to electrodes patches B and D for ≥ 30 minutes to ensure that the system had reached a steady state. Lateral EIS measurements across the electrolyte were performed independently using electrode patches A and C. (See Figure II.1)

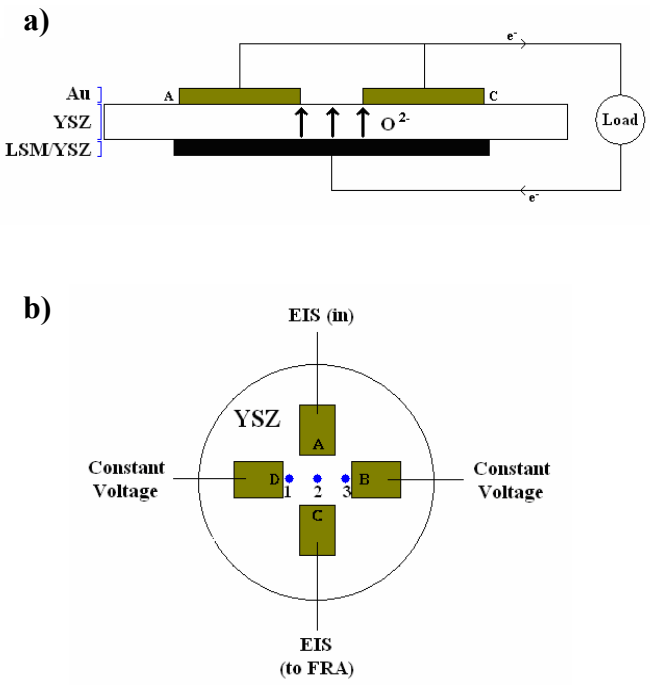

Figure II.1. Schematics of surface impedance and *in situ* Raman oxide mapping measurements performed on YSZ. a) Cross section of SOFC, showing electrodes that are controlling through-cell polarization, b) aerial view of anode side of SOFC showing all four electrodes and measurements they are conducting The electrodes controlling through cell polarization are B and D and the electrodes running the lateral EIS measurements are A and C.

All vibrational Raman spectra were acquired using a Renishaw InVia Raman microscope. A custom designed optical assembly was used to hold a 50x long working distance microscope objective that could be lowered into the furnace and collect backscattered signal. The objective was able to focus the laser to a spot diameter of ~ 2 μm. Raman spectra and impedance data were acquired concurrently. To spatially resolve relative oxide concentrations, spectra were acquired from the same spot on the YSZ electrolyte (position 1, 2, or 3) as the overpotential was changed. After 30 minutes of conditioning at each new V_{op}, a new spectrum was acquired. Data presented below show that this repetitive laser exposure at a single

location did not result in irreversible material changes. After all overpotentials had been sampled at a single position on YSZ, the laser would be repositioned to another location and the sequence repeated. Due to mechanical limitations, the visible spot needed to be translated manually across the YSZ gap between the anode patches (electrodes B and D) that were controlling the through-cell polarization. For a given MEA, benchmark, though-cell measurements were conducted at the beginning and conclusion of the experiment to ensure results were reproducible and that the SOFC did not suffer long term performance degradation.

3. Results and Discussion

Despite the absence of a traditional electrocatalytic anode, the SOFCs used in these studies exhibited well defined and reproducible electrochemical behavior. Figure II.2 shows through-cell voltammetry and impedance data for a representative MEA. The voltammetry data are highlighted by a steep activation energy at relatively small overpotentials followed by a wide V-I window having significantly lower resistance. The large resistance at low V_{op} is due to the absence of an electrocatalytic anode. EIS data also show the consequences of having simple gold patches serving as electrical contacts. Fitting the through-cell EIS spectrum to an effective equivalent circuit (Figure II.3), we observe that the resistance typically associated with anode activity is quite large (~ 355 Ω) compared to electrolyte supported cells that have a traditional Ni/YSZ cermet anode (~ 3 Ω). Results from fitting all EIS data are reported in Table II.1. The decision to use the equivalent circuit shown in Figure II.3 to model the impedance data was based on the circuit's overall simplicity. The circuit consists of four elements in series, one resistor corresponding to R_{bulk} and three

separate RC elements.[48] The first RC combination (R_1/C_1) describes cathodic processes, R_2/C_2 are associated with anodic processes and the lowest frequency R_3/C_3 combination also correlates with anodic processes.[48-50]

An important focus of this work is to correlate spectroscopic vibrational observable features of the SOFC components directly with SOFC electrochemical performance. Doing so provides the *in situ*, material-specific data that can be used to begin testing proposed models of electrochemical oxidation in these devices. Given the prevalence of YSZ in SOFCs,[2,4,6,19,21,22,24] experiments reported in this work focus specifically on the spectroscopic properties of this material.

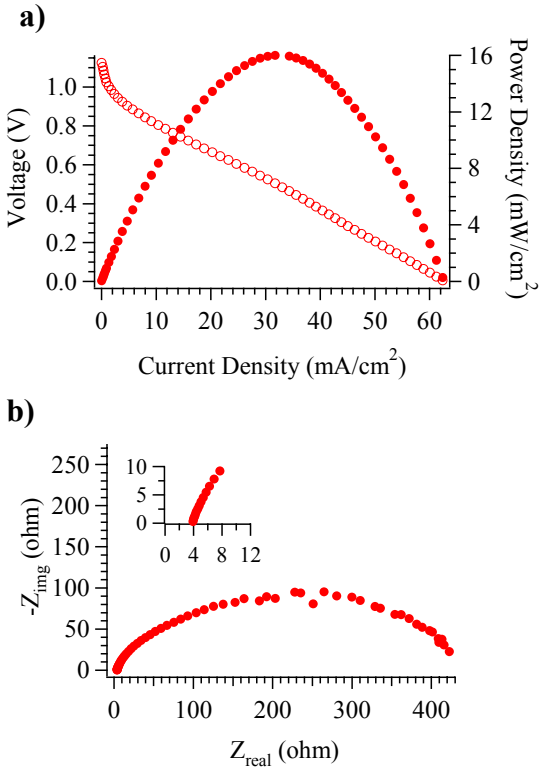

Figure II.2. Electrochemical measurements of anode deficient SOFC: a) LSV; b) EIS with inset showing R_{bulk}. In the EIS measurements, the frequency varied from 100 kHz (low Z_{real}) to 0.03 Hz (high Z_{real}). Peak frequency is at ~ 3.1 Hz

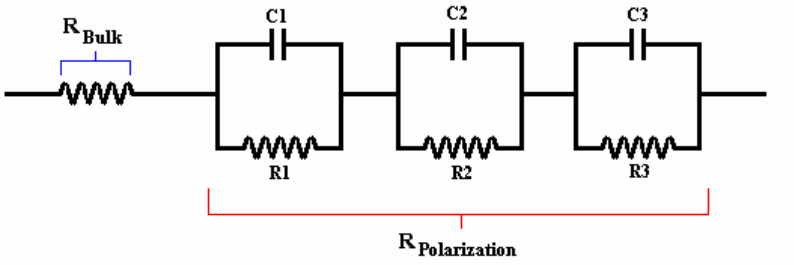

Figure II.3. Schematic of DC circuit model used to analyze EIS data. Results from this modeling are shown in Table II.1.

	$R_{bulk}(\Omega)$	$R_1(\Omega)$	$R_2(\Omega)$	$R_3(\Omega)$	$R_{pol}(\Omega)$
a. Ni/YSZ Anode	5.8 ± 0.1	0.8 ± 0.1	0.8 ± 0.1	2.2 ± 0.1	3.8
b. Au Anode	4.3 ± 0.2	28 ± 3	124 ± 6	231 ± 15	383
c. OCV Surface	43 ± 2.2	86 ± 6	234 ± 21	6680 ± 530	7000
d. 0.30 V Surface	45 ± 2	79 ± 5	208 ± 19	5050± 335	5337
e. 0.60 V Surface	45 ± 2	82 ± 5	216 ± 15	5058 ± 465	5355

Table II.1. Representative data obtained from DC circuit model in Figure II.3. Five case are represented in modeling: a) Electrolyte supported SOFC with a 30 µm Ni/YSZ anode, b) electrolyte supported cell with a gold anode (Figure II.2), c) lateral EIS measurement taken at OCV, d) lateral EIS measurement taken at 0.30 V overpotential, and e) lateral EIS measurement taken at 0.60 V overpotential (Figure II.5).

Figure II.4 shows normalized low frequency Raman spectra of the YSZ electrolyte at a temperature of 715˚C. One spectrum was acquired with the electrolyte material in an oxidizing atmosphere (air) and the other spectrum resulted from YSZ under a reducing atmosphere (of H_2 in Ar). In each case the total acquisition time was 2 minutes. These spectra show considerable low frequency phonon structure but are dominated by a large band near 600 cm^{-1} assigned to the F_{2g} vibrational transition involving correlated stretching motion of adjacent oxides.[14,27] The two spectra -referred to as oxidized and reduced- are virtually identical except for a difference in the total integrated intensity. Changing the atmosphere above the

electrolyte, from oxidizing to reducing, led to a ~ 50 % reduction in signal intensity. The band frequencies and line shapes remained the same, implying that the lattice structure of YSZ did not change. This behavior is reproducible and reversible as seen in Figure II.4b. Figure II.4c shows the kinetics of this change in YSZ vibrational signal intensity as the atmosphere above the anode is changed from oxidizing to reducing. We observe that both the enhancement and reduction of the F_{2g} band intensity occurs on similar timescales of ~ 15 minutes. These data directly and independently confirm findings of earlier, *ex situ* studies that reported a surface reduced phase of YSZ that extends ~ 5 nm into the bulk.[15] More importantly, the ability to differentiate fully oxidized YSZ from YSZ having this surface reduced state *in situ* affords new opportunities to explore material properties under conditions commonly encountered in operating SOFCs.

In order to quantify what role – if any – surface reduced YSZ plays in SOFC operation, we performed a series of surface impedance measurements while the cell operated at different overpotentials. As described in the previous section, these experiments required keeping two anode patches (B and D) at well defined potentials relative to the cathode while the other two anode patches (A and C) were used to launch and measure lateral impedance waves across the surface. Figure II.5 shows data from surface (or lateral) EIS measurements carried out at different through-cell overpotentials. The first observation to note is that R_{pol} is much larger than the through-cell measurement, shown in Figure II.2b and reported in Table II.1. This behavior is not surprising given that neither electrode is catalytically active and that the gap between where the impedance wave is launched and detected is a 4 mm wide

swath of YSZ. A second observation that stands out is that as the cell is polarized to larger overpotentials, both Z_{img} and Z_{real} decrease. In these overpotential dependent experiments, EIS measurements sample YSZ that has reached its steady state condition with patches B and D functioning as anodes relative to the cathode. Patches A and C measure the impedance properties normal to the through-cell polarization. We report this R_{pol} measured between anode patches A and C as the "lateral impedance". A decrease in the lateral real impedance implies that the YSZ surface can more easily conduct charge, while a decrease (in magnitude) of Z_{img} indicates reduced capacitive behavior. Given that the YSZ surface in a functioning SOFC held at OCV will be in its reduced state, there remains a question about what charged species are responsible for the EIS data observed in these lateral impedance measurements. Excess oxide vacancies arising from the reducing atmosphere should improve oxide conductivity. At the same time, reduced YSZ will also have an altered electronic structure relative to the fully oxidized, bulk material, potentially making electron transport more facile. Although the data shown in Figure II.5 correspond to a dry H_2 feed, the results remain qualitatively similar with a humidified H_2 feed (3 % H_2O). The primary difference between the dry vs. wet feeds is when H_2 is humidified, R_{pol} has (slightly) smaller values than those seen with the dry H_2/Ar. This result implies that the large R_3 value observed in the lateral impedance is not due exclusively to a mass transfer resistance associated with delivering H_2O to the patch serving as a cathode. Data with the humidified H_2 compared to a dry H_2 taken on the same cell are shown in Figure II.6.

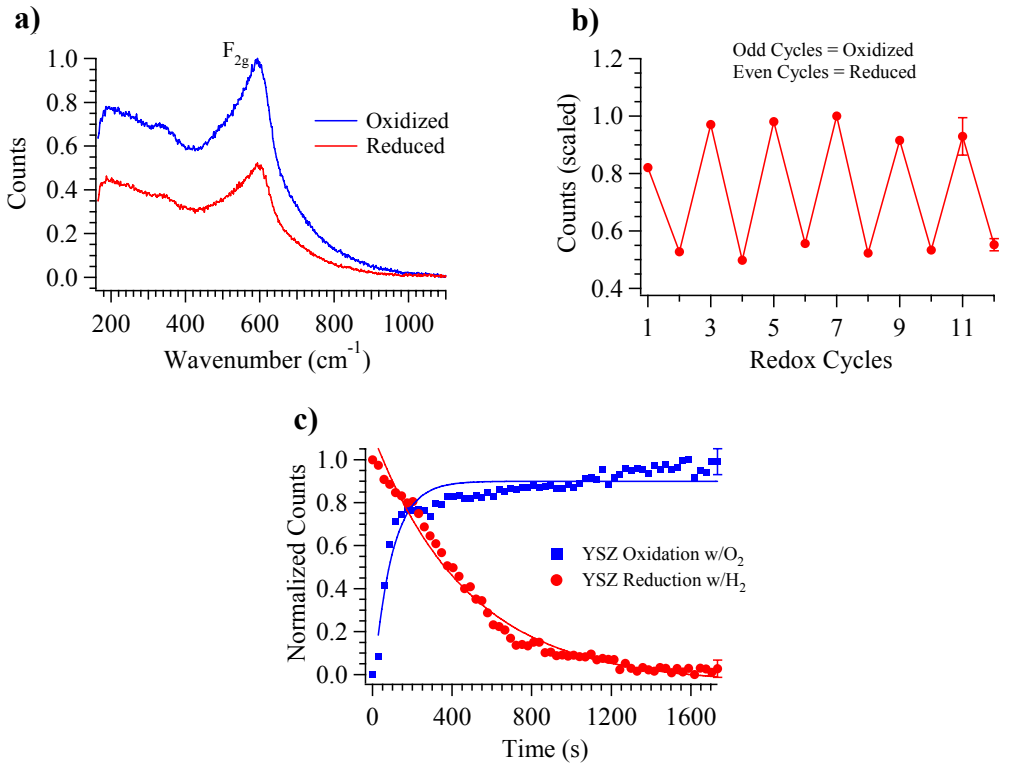

Figure II.4. The reduction and oxidation of YSZ: a) Raman spectra taken at 715˚C, b) monitoring peak height of Zr F_{2g} peak over multiple cycles of reduction and oxidation under reducing and oxidizing environments at 715˚C, and c) monitoring the growth of the YSZ F_{2g} peak with respect to time.

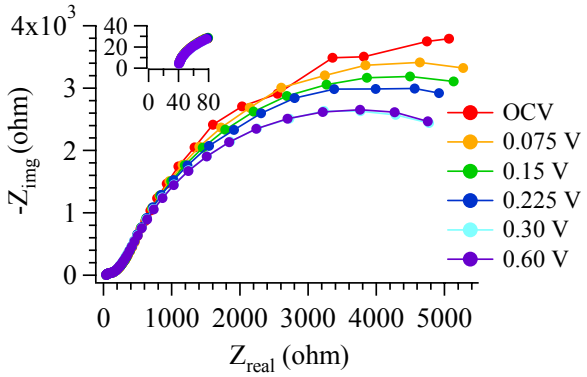

Figure II.5. Surface EIS spectra taken from measurements conducted laterally across YSZ gap as polarization of the SOFC is being varied. Inset showing magnified high frequency section of spectrum.

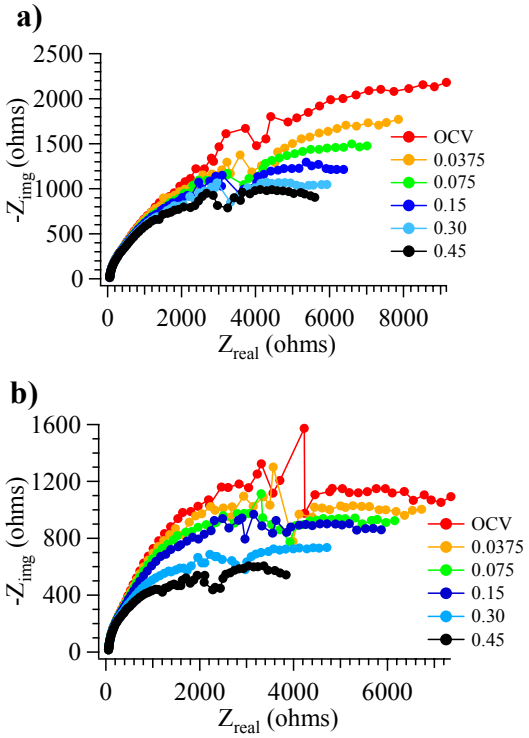

Figure II.6. Surface EIS spectra taken from measurements conducted laterally across YSZ gap as polarization of the SOFC is being varied under dry and humidified fuel conditions a) dry H_2/Ar, b) humidified (3 % H_2O) H_2/Ar.

At the high frequency limit, all surface impedance data converge to an R_{bulk} value of ~ 40 Ω. This result matches to within a factor of two what one would expect simply by scaling the through-cell R_{bulk} by the difference between electrolyte thickness (0.8 mm) and the distances between the electrodes patched A and C (4 mm). Furthermore, R_{bulk} in these lateral EIS measurements does not depend on the through-cell polarization as evidenced by the constant value measured at different overpotentials. This result implies that changes in the EIS data shown in Figure II.5 are not due to changes in the ability of the YSZ surface to conduct oxide ions. As the cell is operated at higher overpotentials, data in Figure II.5 show that R_{pol} decreases significantly. Assuming the four component equivalent circuit described earlier, fits

to the data show that the most important contribution to this reduction in R_{pol} is a decrease in R_3. R_3 is generally assigned to resistances to low frequency dependent anodic processes.[48-50] Qualitatively similar results observed using humidified H_2 rules out a gas phase mechanism and leads us to propose that changing YSZ surface chemistry affects either electron transport or adsorbate surface diffusion between the two anode patches (A and C) used in the EIS measurements.

The lateral EIS measurements show that the electrochemical properties of YSZ depend upon cell operating conditions. *In situ* Raman spectroscopy was used to examine directly the chemical condition across the YSZ electrolyte surface as a function of cell polarization. Affixing the SOFC to a translational stage made it possible to acquire YSZ spectra at different positions across the gap between patches B and D. The three positions tested were located ~ 10 μm away from the each electrode surface and in the middle of the YSZ gap (~ 2 mm from Au electrode patches). Figure II.7 shows how the intensity of the YSZ F_{2g} vibrational band changes as the device operates at different overpotentials. Next to each electrode, vibrational band intensity diminished monotonically (by up to ~ 30 %) as overpotential was increased. Overpotentials ≥ 0.30 V led to no additional change in the F_{2g} band intensity. At position 2, F_{2g} band intensity rose by a small but measurable amount (~ 4 %). These observations are surprising. Data in Figure II.4 show that a reduction in the F_{2g} transition intensity correlates with a surface reduced state of YSZ.[15] YSZ exposed to a reducing atmosphere and at OCV should be reduced, but the overpotential dependent Raman data imply that the YSZ surface can be reduced even further. As the cell becomes more polarized, the oxide anion flux to

the anode increases, and one might expect that the YSZ surface should begin to show some evidence of oxidation. Instead, the observed decrease in the YSZ F_{2g} band intensity shows that near the anodes oxide ion concentration is further depleted, and this effect depends proportionately on V_{op}. Furthermore, the spatially resolved spectroscopic measurements show that oxide depletion can extend ~ 10 μm away from the traditional three phase boundary defined by the anode-electrolyte junction. Additional data with spectra acquired at five spots spaced equidistant between electrode patches, showed a consistent pattern of oxide depletion occurring closet to anode patches and this effect was minimized closer to the center position (furthest away from both electrode B and D). Figure II.8 shows the reversibility of this effect on the YSZ surface where spectra (at position 1) were acquired sequentially with a cell at OCV, $V_{op} = 0.30$ V, and at OCV. Polarizing the cell resulted in the observed reduction in the F_{2g} band, but returning to OCV led to recovery of the original OCV signal in a matter of minutes.

EIS data complement these spatially resolved spectroscopic measurements. In both the optical and electrochemical experiments, data show that the effects of polarizing the cell on the properties of YSZ reach asymptotic limits at $V_{op} \geq 0.30$ V. R_{pol} reaches a minimum value (Figure II.5) and the vibrational Raman scattering shows the lowest intensity (Figure II.7c) indicating a limit to surface oxide depletion. Efforts are underway to improve our experimental design so that experiments can be carried out at higher temperatures and with better spatial resolution to explore these effects further.

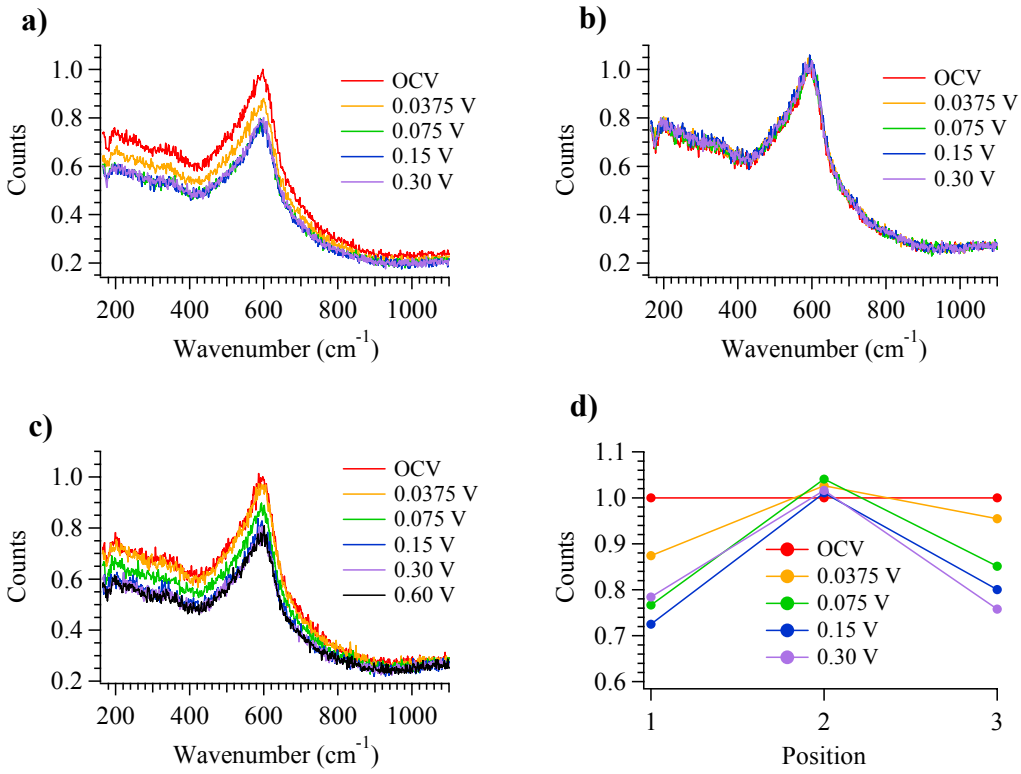

Figure II.7. a) Raman spectra taken at position 1, b) Raman spectra taken at position 2, c) Raman spectra taken at position 3, d) summary of the relative oxide concentration across YSZ gap surface.

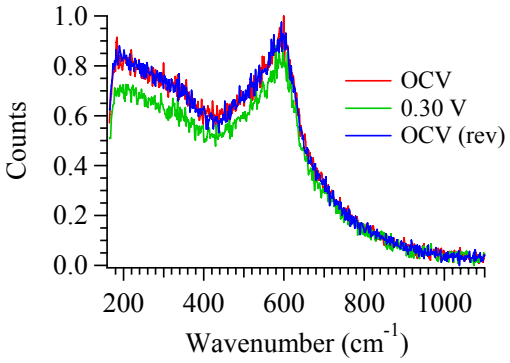

Figure II.8. Raman spectra taken at position 1 nearest to an anode patch showing the reversibility of YSZ surface reduce state after it has been conditioned at an overpotential of 0.30 V and then returning back to OCV.

4. Conclusions

A combination of EIS measurements and *in situ* vibrational Raman spectroscopy has been used to measure the effect that through-cell overpotential has on the properties of a YSZ electrolyte surface and how changes in the state of the YSZ surface can influence electrochemical activity. Initial *in situ* Raman measurements showed that the YSZ surface can be affected by the reducing and oxidizing atmosphere seen in standard SOFC operation. This effect is quantified by a ~ 50 % reduction in the YSZ F_{2g} peak when under reducing conditions. This effect is reversible when cycling back and forth from reducing to oxidizing environments.

Surface EIS measurements were performed to understand how the YSZ surface will be affected as the SOFC is being control electrochemically at different polarizations. These experiments investigated the lateral impedance associated with mass and charge transfer processes across the YSZ surface. The data show that as overpotential of the cell is increased the relative impedance for the processes responsible for charge conduction across the YSZ surface decreases although the EIS data can not identify a mechanism responsible for this observation.

To address the questions posed by the surface EIS measurements, *in situ* Raman spectroscopy was used to measure the relative oxide concentration across the YSZ surface. Data showed that near the TPB, YSZ becomes more even more reduced as overpotential increases. This observed surface reduction suggests an explanation for the observed decrease in lateral impedance across the YSZ surface

as the polarization of the cell is increased. Namely, the altered electronic structure of the reduced surface layer may improve (slightly) electronic conductivity. This altered electronic structure may also promote chemistry not generally associated with fully-oxidized YSZ. For example, surface reduced YSZ might also be able to promote spillover chemistry from electrodes thereby effectively increasing the width of the elecrochemically active region.

The *in situ* spectroscopic methods described in this paper provide insight into mechanisms responsible for data measured by standard electrochemical measurements. These two techniques were used in combination to provide a molecular perspective of the chemistry occurring across the YSZ electrolyte. Data from these two complementary methods can be used to better understand the role of YSZ in the processes occurring in SOFCs and, hopefully, spur the design more accurate models describing electrochemical oxidation.

5. References

(1) Atkinson, A.; Barnett, S.; Gorte, R.; Irvine, J.; Mcevoy, A.; Mogensen, M.; Singhal, S.; Vohs, J. *Nat. Mat.*, **2004**, *3*, 17.

(2) Song, C. *Catal. Today*, **2002**, *77*, 17.

(3) Coutelieris, F.; Douvartzides, S.; Tsiakaras, P. *J. Power Sources*, **2003**, *123*, 200.

(4) Ormerod, R. *Chem. Soc. Rev.*, **2003**, *32*, 17.

(5) Douvartzides, S.; Coutelieris, F.; Demin, K.; Tsiakaras, P. *AlChE J.*, **2003**, *49*, 248.

(6) Minh, N. *Solid State Ionics*, **2004**, *174*, 271.

(7) Kakac, S.; Pramuanjaroenkij, A.; Zhou, X. *Int. J. Hydrogen Energy*, **2007**, *32*, 761.

(8) Zhu, H.; Kee, R. *J. Elecrochem. Soc.*, **2006**, *153*, A1765.

(9) Pornprasertsuk, R.; Ramanarayanan, P.; Musgrave, C.; Prinz, F. *J. Appl. Phys.*, **2005**, *98*, 103513.

(10) Manning, P.; Sirman, J.; Souza, R.; Kilner, J. *Solid State Ionics*, **1997**, *100*, 1.

(11) Hassel, B.; Boukamp, B.; Burggraaf, A. *Solid State Ionics*, **1992**, *53-56*, 890.

(12) Ridder, M.; Welzenis, R.; Brongersma, H.; Kreissig, U. *Solid State Ionics*, **2003**, *158*, 67.

(13) Svensson, A.; Sunde, S.; Nisancioglu, K. *J. Electrochem. Soc.*, **1997**, *144*, 2719.

(14) Perry, C.; and Feinberg, A. *Solid State Commun.*, **1980**, *36*, 519.

(15) Pomfret, M.; Stoltz, C.; Varughese, B.; Walker, R. *Anal. Chem.*, **2005**, *77*, 1791.

(16) Perry, C.; Feinberg, A.; Currat, R. *Bull. Amer. Phys. Soc.*, **1981**, *26*, 405.

(17) Vernoux, P.; Guth, M.; Li, X. *Electrochem. Solid-State Lett.*, **2009**, *12*, E9.

(18) Guo, X. *Solid State Ionics*, **1995**, *81*, 235.

(19) Haering, C.; Roosen, A.; Schichl, H. *Solid State Ionics*, **2005**, *176*, 253.

(20) Swider, K.; Worrell, W. *J. Electrochem. Soc.*, **1996**, *143*, 3706.

(21) Hattori, M.; Takeda, Y.; Sakaki, Y.; Nakanishi, A.; Ohara, S.; Mukai, K.; Lee, J.; Fukui, T. *J. Power Sources*, **2004**, *126*, 23.

(22) Hattori, M.; Takeda, Y.; Lee, J.; Ohara, S.; Mukai, K.; Fukui, T.; Takahashi, S.; Sakaki, Y.; Nakanishi, A. *J. Power Sources*, **2004**, *131*, 247.

(23) Levy, M.; Fouletier, J.; Kleitz, M. *J. Electrochem. Soc.*, **1988**, *135*, 1584.

(24) Hirabayashi, D.; Tomita, A.; Brito, M.; Hibino, T.; Harada, U.; Nagao, M.; Sano, M. *Solid State Ionics*, **2004**, *168*, 23.

(25) Fu, Q.; Mi, S.; Wessel, E.; Tietz, F. *J. Eur. Cerm. Soc.*, **2008**, *28*, 811.

(26) Hui, S.; Petric, A. *J. Electrochem. Soc.*, **2002**, *149*, J1.

(27) Feinberg, A.; Perry, C. *J. Phys. Chem. Solids*, **1981**, *42*, 513.

(28) Goodenough, J. *Annu. Rev. Mater. Res.*, **2003**, *33*, 91.

(29) Devanathan, R.; Weber, W.; Singhal, S.; Gale, J. *Solid State Ionics*, **2006**, *177*, 1251.

(30) Martinez, A.; Brouwer, J. *J. Power Sources*, **2010**, *195*, 7268.

(31) DeCaluwe, S.; Zhu, H.; Kee, R.; Jackson, G. *J. Electrochem. Soc.*, **2008**, *155*, B538.

(32) Kenney, B.; Valdmanis, M.; Baker, C.; Pharoah, J.; Karan, K. *J. Power Sources*, **2009**, *189*, 1051.

(33) Janardhanan, V.; Heuveline, V.; Deutschmann, O. *J. Power Sources*, **2008**, *178*, 368.

(34) Zhu, W.; Ding, D.; Xia, C. *Electrochem. Solid-State Lett.*, **2008**, *11*, B83.

(35) Fukunaga, H.; Ihara, M.; Sakaki, K.; Yamada, K. *Solid State Ionics*, **1996**, *86-88*, 1179.

(36) Schmidt, M.; Hansen, K.; Norrman, K.; Mogensen, M. *Solid State Ionics*, **2009**, *180*, 431.

(37) Sukeshini, A.; Habibzadeh, B.; Becker, B.; Stoltz, C.; Eichhorn, B.; Jackson, G. *J. Electrochem. Soc.*, **2006**, *153*, A705.

(38) Mizusaki, J.; Tagawa, H.; Saito, T.; Kamitani, K.; Yamamura, T.; Hirano, K.; Ehara, S.; Takagi, T.; Hikita, T.; Ippomatsu, M.; Nakagawa, S.; Hashimoto, K. *J. Electrochem. Soc.*, **1994**, *141,* 2129.

(39) Li, Y.; He, D.; Zhu, Q.; Zhang, X.; Xu, B. *J. Catal.*, **2004**, *221*, 584.

(40) Eder, D.; Kramer, R. *Phys. Chem. Chem. Phys.*, **2002**, *4*, 795.

(41) Wright, D.; Thorp, J.; Aypar, A.; Buckley, H. *J. Mat. Sci.*, **1973**, *8*, 876.

(42) Nagle, D.; PaiVerneker, V.; Petelin, A.; Groff, G. *Mat. Res. Bull.*, **1989**, *24*, 619.

(43) Wachsman, E.; Jiang, N.; Frank, C.; Mason, D.; Stevenson, D. *Appl. Phys. A*, **1990**, *50*, 545.

(44) Pomfret, M.; Marda, J.; Jackson, G.; Eichhorn, B.; Dean, A.; Walker, R. *J. Phys. Chem. C*, **2008**, *112*, 5232.

(45) Pomfret, M.; Owrutsky, J.; Walker, R. *Anal. Chem.,* **2007**, *79*, 2367.

(46) Pomfret, M.; Owrutsky, J.; Walker, R. *J. Phys. Chem. B,* **2006**, *110*, 17305.

(47) Pomfret, M.; Demircan, O.; Sukeshini, A.; Walker, R. *Environ. Sci. Technol.*, **2006**, *40*, 5574.

(48) Laurencin, J.; Delette, G.; Sicardy, O.; Rosini, S.; Lefebvre-Joud, F. *J. Power Sources*, **2010**, *195*, 2747.

(49) Hofmann, P.; Panopoulos, K. *J. Power Sources*, **2010**, *195*, 5320.

(50) Jiang, S.; Love, J.; Badwal, S. *Electrical Properties of Oxide Materials*, **1997**, *125*, 81.

Chapter 3: High Temperature *In Situ* Vibrational and *Ex situ* Absorption Analysis of Reduced and Oxidized Yttria Stabilized Zirconia

1. Introduction

Solid oxide fuel cells (SOFCs) are electrochemical devices that operate at temperatures ≥ 650˚C in order to produce low emission DC electricity.[1-3] Since these devices are converting chemical energy directly into electrical energy, the resulting efficiencies can be ≥ 80 % when configured into combined heat and power generation systems, and because the fuel is electrochemically oxidized, these devices do not produce significant amounts of NO_χ and SO_χ pollutants.[1-3] Commercially deployed SOFCs can range in size from small portable devices (50 W, Adaptive Materials Inc.) to large stationary power generation systems (250 kW, Siemens Westinghouse), and because of their high operating temperatures these devices can use a wide variety of fuels including *syn*-gas, H_2, liquified natural gas, bio-derived fuels, and traditional fossil fuels.[2-6] Whether in portable or stationary devices, the general construction of these devices includes the use of an electrocatalytic anode and cathode separated by an ion conducting solid oxide electrolyte.[2,3,7] Figures of merit for solid oxide electrolytes include high oxide conductivities, thermal and chemical stability, and large resistance to electron conduction.[8-18] The general reactions in SOFCs include electrocatalytic reduction of molecular oxygen to form oxide anions at the cathode and electrocatalytic oxidation of fuel at the anode to drive the formation of products (H_2O and CO_2) and electricity.[19,20] The electrolyte plays an important role by

completing the circuit in these SOFC processes allowing oxide anions to diffuse from the cathode to the anode.[8,21-27]

One of the most common metal oxide materials used as an electrolyte in SOFCs is ytrria stabilized zirconia (YSZ).[2,3,27,28] YSZ is a ceramic oxide material that has a face-centered cubic crystal structure that has a thermodynamically stable phase for Y_2O_3 compositions of 5-12 % by mole fraction yttrium.[13,26,27,29] ZrO_2 by itself is stable in the monoclinic phase at temperatures $\leq 1150^{\circ}C$ and doesn't adopt a cubic, fluorite crystal structure until temperatures are $\geq 2400^{\circ}C$.[27,29] Doping yttria (Y_2O_3) into ZrO_2 stabilizes the cubic structure at temperatures up to $2450^{\circ}C$.[30] In the YSZ crystal lattice, one equivalent of Y_2O_3 replaces two equivalences of ZrO_2 leaving behind an oxide vacancy.[9,26,27,29] These oxide vacancies are distributed randomly throughout the crystal lattice and are responsible for the material's ionic conductivity.[9,12,26,27,29,31-33] The relatively high, activation energy to oxide diffusion through the electrolyte (100 kJ/mol) and the large barrier to molecular oxygen activation (223 kJ/mol) at the cathode underlie the need for SOFCs to operate at high temperatures.[34,35] At lower temperatures, insufficient oxide flux from the cathode to the anode limits the current that can be drawn from these devices. SOFCs operating at high temperatures and produce electricity efficiently and cleanly, but the high temperature conditions raise challenges to studying the chemistry occurring in SOFCs by limiting the methods that can probe *in situ* and in real time the molecular mechanisms responsible for electrochemical oxidation and reduction.

Despite YSZ's importance as the ion conductor in SOFCs, potential roles that YSZ may play in promoting electrochemical activity remain largely unexplored.

Kinetic models describing chemistry in SOFCs define the electrochemically active three phase boundary (TPB) as the junction of the electron conducting anode, the oxide anion conducting electrolyte and the gas phase fuel mix.[36-41] The theoretical TPB of an SOFC is defined as a 1-dimensional line although most models will assign this region a finite width that is on the order of submicron to microns.[36-41] There are many variables that can change the length scale of the TPB such as overpotential, temperature, anode microstructure, and partial pressures of fuels.[42,43] Absent in all of this modeling, however, is any consideration of how the properties of YSZ are influenced by the high temperatures and the strongly oxidizing and reducing conditions that occur during SOFCs operation. Reduced YSZ has been shown to be an efficient catalyst in the reforming of hydrocarbons,[44,45] thus the surface condition of YSZ in operating devices, especially near the anode, deserves examination when modeling fuel oxidation processes and spillover chemistry.

Recent reports suggest that the surface chemistry of YSZ can change under conditions commonly encountered in operating SOFCs. Wachsman and coworkers, saw that under reducing conditions the YSZ showed evidence of "blackening" that was attributed to an increase of oxide vacancies at the surface and zirconium precipitation that left behind F-centered defects in the crystal.[46] These defects leave two electrons in the unoccupied vacancy and this reduced character can affect heterogeneous electrocatalytic activity and charge carrying capability of the YSZ.[46] Consistent with these measurements were findings by Pomfret et. al., who reported that heating an YSZ sample to 1000˚C in a reducing atmosphere and then cooling the sample back down to room temperature still in a reducing atmosphere resulted in a

surface reduced phase of YSZ that was stable at ambient temperatures and atmospheres as determined by *ex situ* methods.[27] Additional angle-resolved X-ray photoelectron spectroscopy (XPS) measurements indicated that this newly formed reduced state extended only a few lattice spacings into the sample.[27] Swider et. al., observed that under a reducing atmosphere, YSZ exhibits both oxygen-ion conductivity and n-type conductivity and suggested that this material would be well suited for a mixed ionic and electronic conducting (MIEC) dense anode material.[12] This change in electronic structure could influence YSZ behavior with respects to the TPB because the ionic and electrical transport properties of surface-reduced YSZ are not well characterized. Little is known about how the YSZ surface and how surface chemistry will evolve *in situ* under common SOFC operating conditions. Data discussed below combine *in situ* and *ex situ* techniques that are capable of characterizing the vibrational and electronic state of this YSZ surface reduced state.

2. Experimental

2A. Electrolyte Construction

The yttria-stabilized zirconia (YSZ) used in these studies is similar to that used in previous experiments in our group.[27,47-50] YSZ powder (Tosoh Corporation) consisted of 8 % Y_2O_3 (by mole fraction of Y relative to Zr). A mass of 2.0 g of the YSZ powder was loaded into a 1.1 inch die and pressed at 20,000 psi for 5 minutes to produce an YSZ disc that was then sintered at 1500˚C for one hour in ambient air with a heat up and cool down rate of 1˚C/min. The resulting electrolyte disc had a diameter of ~ 25 mm and a thickness of 0.80 ± 0.02 mm. The YSZ disc was mounted

in a quartz tube surrounded by a split tube furnace where Raman spectra could be acquired at temperatures up to 765˚C.

2B. *In Situ* Raman Assembly

The complete *in situ* Raman assembly used for material research in this paper has been described previously.[47-50] A distinguishing attribute of this device is the quartz tube that allows vibrational Raman scattering experiments to focus 488 nm light onto the electrolyte material and detect the backscattered signal with a microscope objective/CCD assembly (inVia, Renishaw). A custom designed optical assembly was also used to hold a 50x long working distance microscope objective (Leica) that could be lowered into the furnace and collect backscattered signal. The microscope objective focused the incident light to a spot diameter of ≤ 2 μm. All experiments conducted with the Raman spectrometer used 8 mW of 488 nm light, and all experiments were carried out at a temperature of 715˚C.

Gas flows to both sides of the electrolyte were controlled by rotameters (Omega). 108 sccm of Ar was used on the backside of the YSZ disc to create an inert atmosphere and eliminate a potential source of oxide ions. The side studied with Raman spectroscopy was exposed to a variety of gas mixtures to control the surface redox state. To reduce YSZ, a gas mixture of 100 sccm H_2/108 sccm argon was used. To oxidize YSZ, the gas mixture changed to 100 sccm O_2/108 sccm argon. To preserve surface reduced states of YSZ for e*x situ* XAS analysis, YSZ was cooled under argon.

2C. X-ray Absorption Spectroscopy (XAS) Measurements

The polarization dependent X-ray absorption spectroscopy (XAS) measurements were carried out at beamline 4.0.2 and 6.3.1 of the Advanced Light Source (Lawrence Berkeley National Laboratories) in a total electron yield mode (TEY) with nominal spot sizes of 20 μm and 100 μm, respectively. Samples examined included as-sintered oxidized YSZ, and both oxidized and reduced samples that had been probed using *in situ* Raman spectroscopy as described above. Samples that had been studied with Raman spectroscopy were stored in a desiccator and tested 7 days to 1.5 months after exposure. Previous work has shown that the surface reduced state of YSZ is largely insensitive to ambient conditions if temperatures are < 400 K.[27] The polarization dependent XAS spectra of the zirconium M_{45}-edges and oxygen K-edge were measured at both beamlines while the Yttrium L_{23}-edge was only measured at beamline 6.3.1 due to energy limitations.

3. Results and Discussion

3A. *In situ* Raman Spectroscopic Measurements

Previous work by Pomfret, et. al. demonstrated that when a sintered YSZ pellet is heated to 1000˚C under a reducing atmosphere, of 5 % H_2:95 % argon and then cooled (still under a reducing atmosphere), the resulting Raman spectrum has an intensity that was 50 % less than the oxidized form when tested *ex situ*.[27] *Ex situ,* angle-resolved XPS measurements, performed on the same samples identified a surface reduced state of the YSZ material that extends ~ 5 nm into the bulk. More recently, experiments in our own lab have begun to quantify the kinetics associated

with reduction and oxidation of this material. Figure III.1a shows low frequency Raman spectra of the reduced and oxidized YSZ electrolyte at a temperature of 715˚C. In each case the total acquisition time was 2 minutes. The oxidized sample is exposed to the O_2/Ar mix while the reduced spectrum results from the same sample exposed to the H_2/Ar gas mixture. Spectra were acquired after 30 min of gas mixture exposure. The Raman spectrum of 8 % YSZ contains considerable phonon structure in the low frequency region, but the spectrum is dominated by a large band near 600 cm^{-1} called the F_{2g} band. This vibration is assigned to the anticorrelated motion of adjacent oxide ions.[21,27] The oxidized and reduced spectra look remarkably similar except for a noticeable and reproducible change in intensity. Changing the atmosphere above the electrolyte leads to a ~ 50 % reduction in signal intensity, but the band shape remains the same suggesting that the crystal structure of YSZ also remains the same. This conclusion is supported by previous *ex situ* XRD experiment performed by Pomfret, et. al. with oxidized and reduced samples.[27] This change in scattered Raman signal intensity is reversible as shown in Figure III.1b, when the Zr F_{2g} band peak height is monitored with respect to the atmosphere being switched from oxidizing to reducing at operational temperatures of 715˚C. Two important points to note are that consecutive spectra were acquired from the same spot as to maintain sample focus.

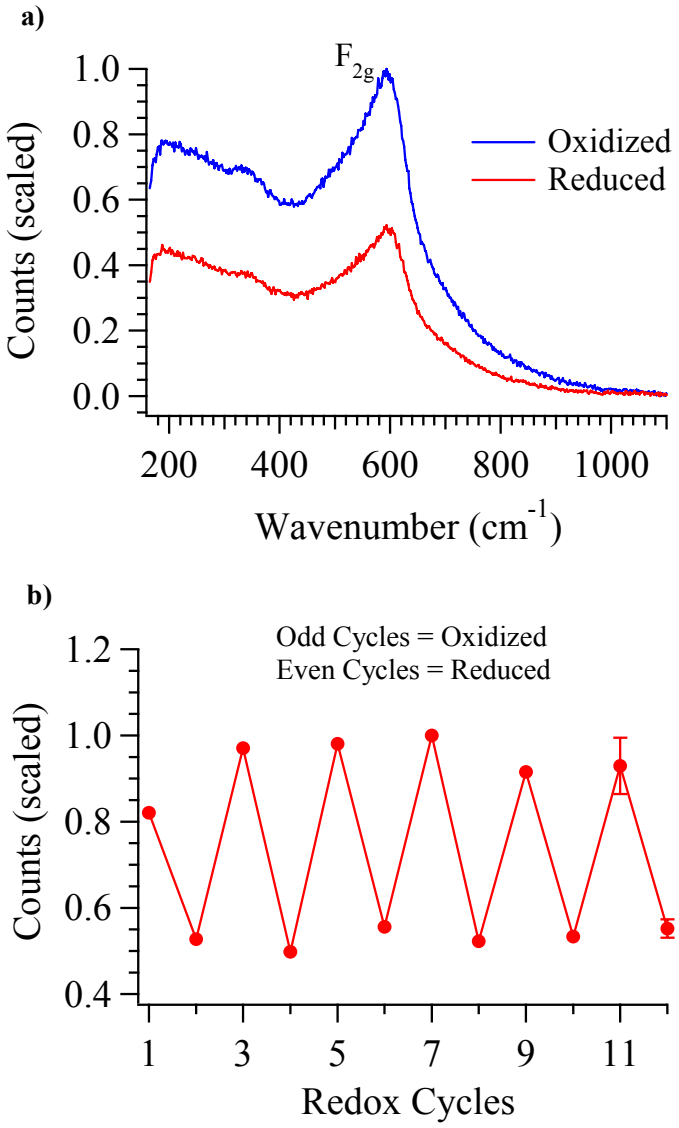

Figure III.1. The reduction and oxidation of YSZ: a) Normalized Raman spectra taken at 715˚C, b) monitoring peak height of normalized Zr F_{2g} peak over multiple cycle of reduction and oxidation under reducing and oxidizing environments at 715˚C. Representative error bars at cycle 11 and 12 show the standard deviation for oxidized and reduced samples.

Given signal to noise considerations, the Raman spectrometer can acquire spectra from the YSZ pellet every ~ 5 sec, Figures III.2a and b. meaning that the kinetics of surface oxidation and reduction can be monitored in real time. Figure III.2c shows the time-dependent peak intensity of the F_{2g} band as the YSZ

sample is exposed to either an O_2 oxidizing environment or an H_2 reducing environment. The data show that oxidization of a reduced sample is very fast and is ~ 90 % complete with in 150 sec. Reduction is slower requiring > 20 min. to reach completion.

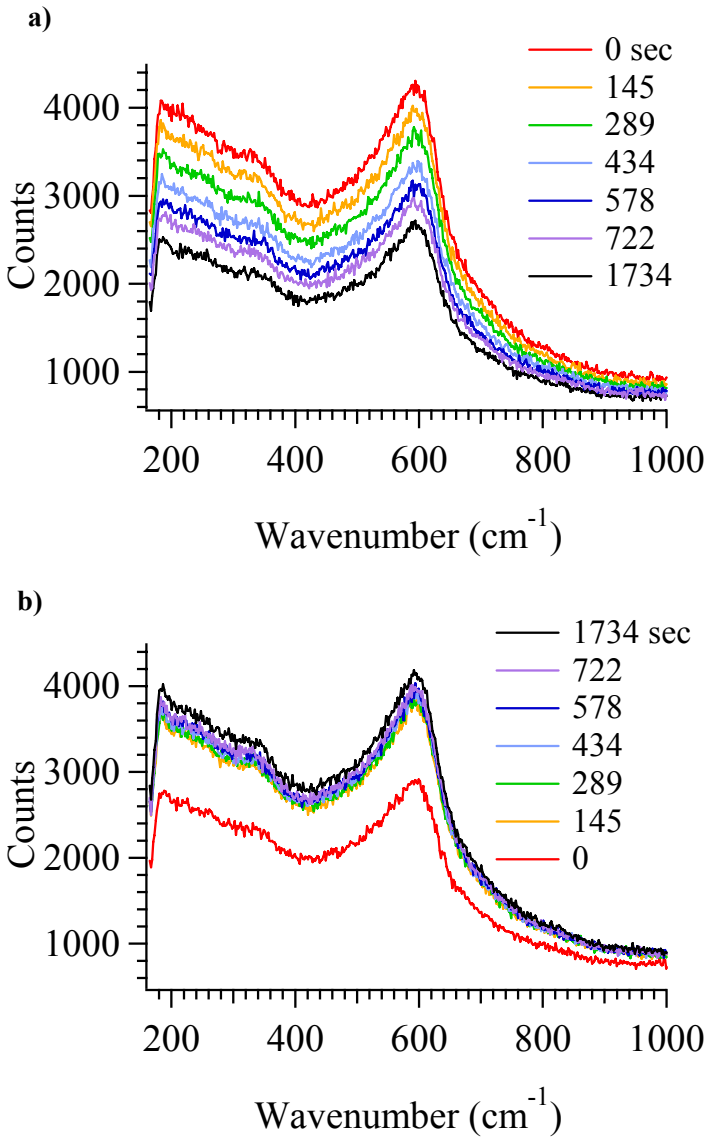

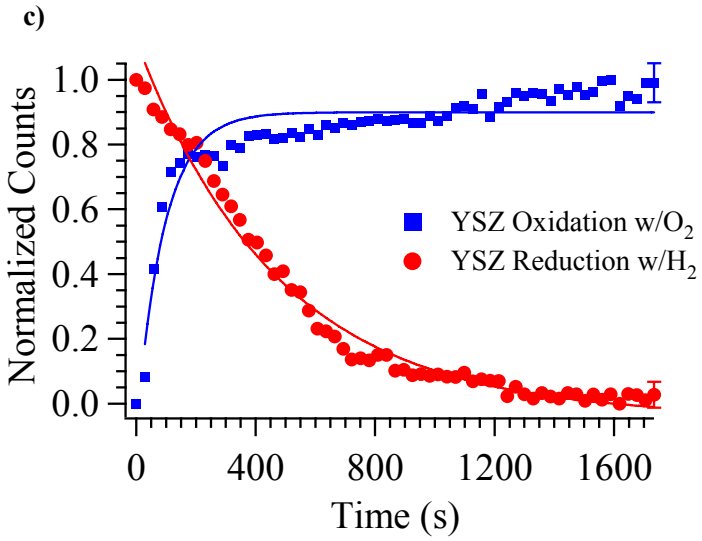

Figure III.2. a) YSZ reduction with H_2/Ar gas mixture at 715˚C. b) YSZ oxidation with O_2/Ar. c) Monitoring the normalized Zr F_{2g} peak height with respect to time in a reducing and oxidizing environment. Fits to first order kinetic rate laws are included as guides for the eye.

Different aspects of YSZ reduction have been examined by a number of researchers,[5,6,21,22] and the process is assumed to proceed through oxide extraction from the material where "O_o^0" is the oxide ion in the crystal lattice and "V_o^{2+}" is the vacancy created when the oxide reacts with H_2 to form H_2O (Eq. 1). The resulting electrons that are left behind partially reduce the Y and Zr remaining in the crystal lattice as reported in previous angle-resolved XPS measurements.[27,46]

$$H_2 + O_o^0 \rightarrow H_2O + V_o^{2+} + 2e^- \qquad \textbf{(Eq. 1)}$$

Oxidation of the reduced YSZ surface with molecular oxygen is also straightforward as shown in Eq. 2 where oxygen reacts with the oxide vacancy and electrons to produce a filled oxide site.

$$\tfrac{1}{2}O_2 + V_o^{2+} + 2e^- \rightarrow O_o^0 \qquad \textbf{(Eq. 2)}$$

The data show clearly that YSZ reduction (at 715˚C) proceeds much more slowly than the corresponding oxidation. The detailed mechanisms for these differences remain uncertain and deserve further investigations. Interestingly, Eq. 1 implies that excess H_2O (in the form of humidified fuel feeds, for example) should repopulate newly created oxide vacancies.

3B. *Ex situ* X-ray Absorption Spectroscopic Measurements

While the *in situ* vibrational Raman measurements are informative, they only measure changes in the YSZ properties and can not provide direct information about the chemical transformations responsible for the observed changes. Specifically, the *in situ* measurements can not identify how reduction changes the electronic structure of the YSZ surface and how this altered chemical structure will affect surface reactivity and surface conductive properties. To gain further insight into the changes resulting from YSZ reduction, *ex situ* XAS measurements were performed on YSZ samples that had been reduced at high temperatures and cooled under and inert atmosphere. Previous results have shown that the surface reduced state of YSZ is both air and humidity stable at room temperature.[27]

XAS is an element specific technique that probes unfilled states above the Fermi-level, indirectly measuring the bonding configuration of any specific element in the host lattice. The photo-absorption selection rules associated with polarized X-rays control which unoccupied states are accessed in the X-ray absorption process.

Comparison of the X-ray absorption peak areas using linear or circular polarizations quantitatively determines the degree of occupation/vacancy of different states (m-levels) that can then be related to different bonding configurations. Since the reduced YSZ surface region is believed to contain excess oxygen vacancies, polarization dependent XAS can be especially helpful in detecting the excess electrons associated with these vacancies, especially since it is slightly less surface sensitive then XPS and Raman, yielding information about the extent of the surface layer.

In XAS, photons of tunable energy are used to excite electrons of particular elements from an inner shell to empty states immediately above the Fermi-level, Figure III.3. In our case we examined the $M_{4,5}$ transitions of Zr corresponding to the excitation of $3d_{3/2}$ to 4f for the M_4 edge and $3d_{5/2}$ to 4f for the M_5 edge.(Figure III.4, top) The M_4 edge has a j of 3/2 with $l = 2$ and $m = \pm 1$ and, by applying the selection rules, this leads to possible transitions into the f-states with $l = 3$ and $m = \pm 1$. These orbitals are lying in the xz and yz planes of the unit cell. However, in case of the M_5 edge j is 5/2 with $l = 2$ and $m = \pm 2$ and thus includes the possibility of the transition to the $l = 3$ and $m = \pm 2$ f states which are lying along the body diagonals of the unit cell. For circular light, the f states with $m = \pm 2$ for M_4 and $m = \pm 3$ for the M_5 edge are accessible respectively (details can be found in ref #51).[51] Since the spectra were measured in total electron yield mode (TEY) (equal to the current needed to replenish the emitted electrons), the depth information of the signal is essentially limited by the electron yield sampling depth λ_e.[52] Here we assume the X-ray penetration length λ_X to be much larger than the electron inelastic mean free

path fulfilling $\lambda_e << \lambda_X \cdot \cos\theta$. For emission methods like XPS and AES, an inelastic mean free path of 5-6 Å for energies of ~ 200 eV was measured for transition metals Cu and Au[53,54] yielding 15-18 Å probing depth (95 % signal) which is further reduced by the analyzer angles commonly used in XPS. In contrast, the mean probing depth of TEY XAS at this energy is a factor of two higher and lies around 25–30 Å.[55]

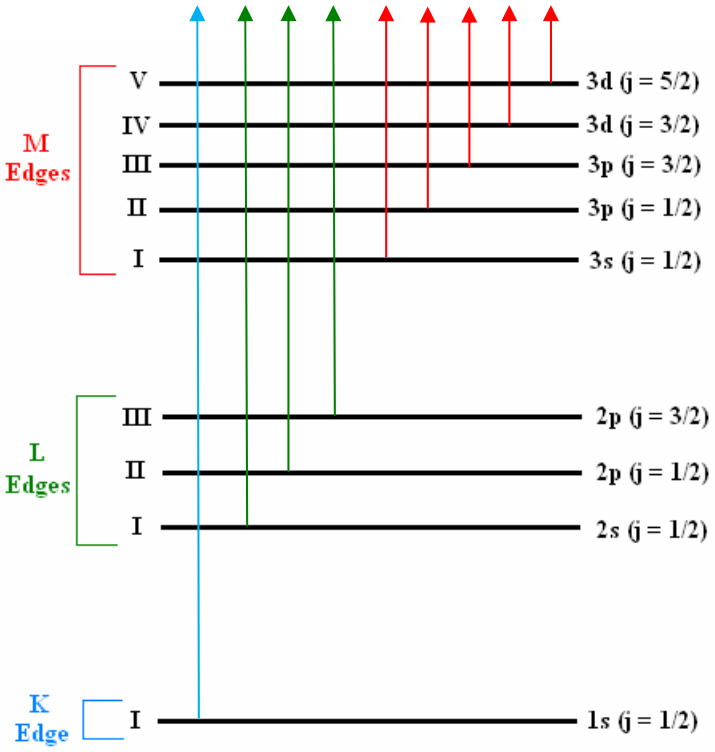

Figure III.3. Transitions that contribute to the X-ray absorption edges. The $M_{4,5}$ and the $L_{2,3}$ edges were of focus in this work.

To avoid contamination of the Zr XAS spectrum from spectral features of the O K-edge due to the transmission of higher energy photons that also satisfy the Bragg condition of the X-ray monochrometer (harmonic X-rays), XAS spectra were also acquired at ALS beamline 4.0.2 using the third harmonic of the elliptical undulator set to 100 % circular polarized light where no higher energy harmonics are present.

After background subtraction and normalization to the Zr M_5 peak intensity, the areas of both peaks were determined and the M_4/M_5 branching ratio calculated (Figure III.4 bottom). No significant change was observed for circular vs. linear polarized light and branching ratios of $M_4/M_5 = 1.55 \pm 0.04$ for reduced YSZ and $M_4/M_5 = 1.24 \pm 0.04$ for oxidized YSZ were observed. Since the peak area in a XAS spectrum represents the number of available (empty) states right above the Fermi-level, a shift in spectral weight is associated with charge transfer between these states, e.g. higher occupation means fewer available empty states for the excitation and thus a smaller integrated peak area in the XAS spectrum. As mentioned above, from the selection rules for optical excitations for linear and circular polarized light, we can determine the occupancy changes of different states upon oxidation and reduction. As determined from Figure III.4 the branching ratio of M_4/M_5 goes up upon reduction of the sample. Interestingly, this means that in the reduced sample the body diagonals of a given Zr atom are more occupied whereas in an oxidized state the body diagonals for Zr are less occupied. This result most likely arises directly from the reduction process where oxygen vacancies along the diagonal bonds for Zr allow the remaining electrons of the now + 2 charged vacancies to reside in the previously empty sates of the Zr in the host lattice. These excess electrons would also explain the increased surface conductivity of the sample and lead to the color variation. This description is supported by the observation that the M_4 to M_5 branching ratio remains the same for circular polarized light, which is however less dependent on the occupancy of the Zr diagonal bonds (circular polarization is most sensitive to the occupancy of the $f_{7/2}$ states which do not change upon reduction of the sample).

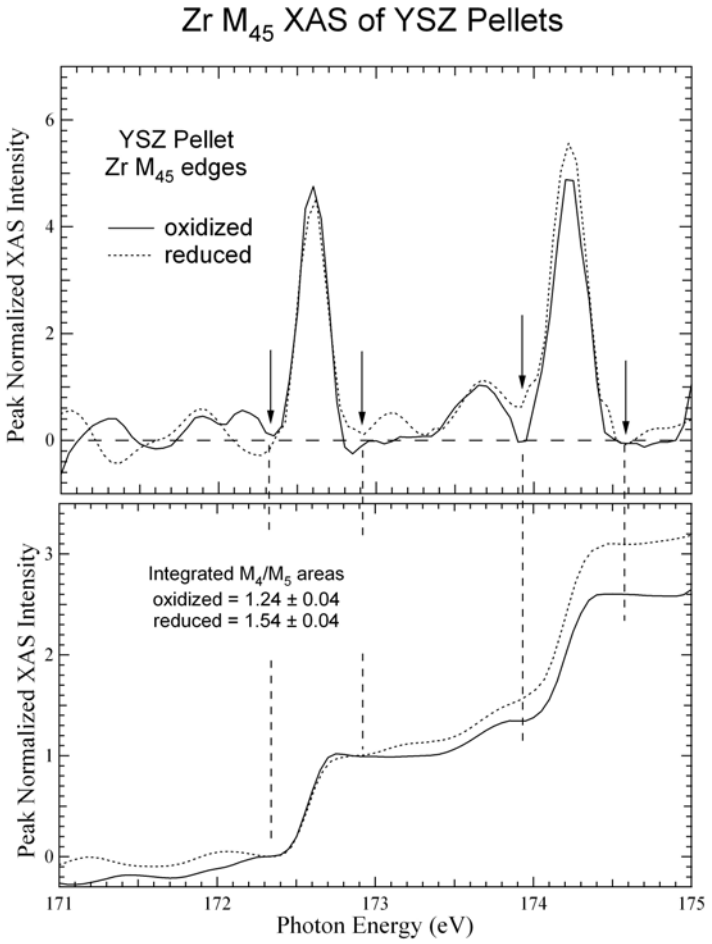

Figure III.4. (top) As collected Zr M_4 and M_5 edge XAS spectra for reduced (dashed line) and oxidized (solid line) YSZ. The data is peak height normalized after a linear background is removed. (bottom) Integral of XAS spectra for determination of branching ratio.

Charge neutrality does not necessarily require modification of the Zr electronic occupation, charge transfer may occur at the Y site, to exclude Y as possible host for the excess electrons, measurements of the Y $L_{2,3}$ edge were done at beamline 6.3.1 with photon energies above 2000 eV. The measured spectra (Figure III.5) are peak normalized (after a linear background subtraction). No significant charge redistribution (difference in branching ratios) for reduced versus

oxidized YSZ was observed. This is strong evidence that Y does not play a role in the formation of conductive surface states in reduced YSZ. Finally, the remarkable stability of these reduced surface states was observed on a sample measured one year after sample reduction where a significantly higher M_4/M_5 branching ratio was measured for Zr in comparison to the oxidized sample.

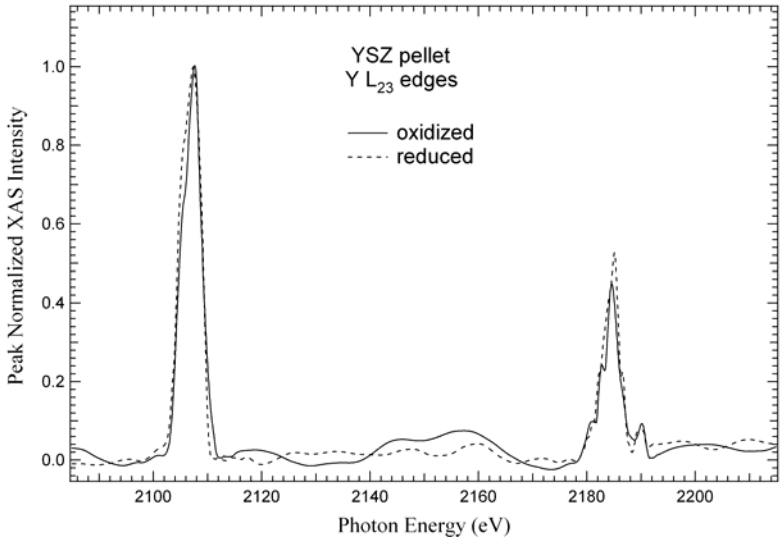

Figure III.5. Normalized XAS spectra for the Y $L_{2\,3}$ edge for reduced (dashed line) and oxidized (solid line) YSZ.

4. Conclusions

The conditions that YSZ was exposed to in these experiments were meant to mimic the environment of an operational SOFC in order to understand the role(s) that YSZ may play in surface conduction and oxidative anode processes. Using a combination of *in situ* Raman and *ex situ* XAS measurements made it possible to explore the changes in the vibrational and electronic state of either the surface reduced or oxidized samples exposed to these conditions. Using Raman spectroscopy revealed that the intensity of the YSZ F_{2g} vibrational band saw a reversible 50 % reduction with no noticeable change in the band shape suggesting that the crystal

structure remained intact, also observed by Pomfret et. al. when conducting XRD measurements of reduced and oxidized YSZ samples.[27] By correlating Raman measurements with time of exposure of an oxidizing or reducing agent provided valuable information about the kinetic information about the oxidization and reduction of YSZ. These measurements provided information that the oxidation is faster requiring < 3 min. for completion as opposed to the slower reduction reaction that required > 20 min. for completion. Another interesting finding of this work is that the excess electrons left behind in the reduction of YSZ results in a partial reduction of Zr in the crystal lattice located near the surface, this process is not seen for Y. This finding is significant providing strong evidence that only Zr plays a role in the formation of conductive surface states in reduced YSZ.

YSZ was originally chosen as an electrolyte material for SOFCs base on it high oxide ionic conductivities, thermal stability, and large resistance to electron conduction. The results from the experiments described in this paper reveal that this might not be the case for the surface of YSZ, especially on the anode side, which shows changes in the vibrational and electronic state that is different from the bulk of this material. Results from this work starts to provide quantitative benchmarks to create more accurate SOFC models describing electrochemical oxidation processes that take into account spillover chemistry onto the electrolyte thereby increasing the role of YSZ in these fuel oxidation processes.

5. References

(1) Pomfret, M.; Demircan, O.; Sukeshini, A.; Walker, R. *Environ. Sci. Technol.*, **2006**, *40*, 5574.

(2) Ormerod, R. *Chem. Soc. Rev.*, **2003**, *32*, 17.

(3) Song, C. *Catal. Today*, **2002**, *77*, 17.

(4) Douvartzides, S.; Coutelieris, F.; Demin, K.; Tsiakaras, P. *AlChE J.*, **2003**, *49*, 248.

(5) Atkinson, A.; Barnett, S.; Gorte, R.; Irvine, J.; Mcevoy, A.; Mogensen, M.; Singhal, S.; Vohs, J. *Nat. Mat.*, **2004**, *3*, 17.

(6) Coutelieris, F.; Douvartzides, S.; Tsiakaras, P. *J. Power Sources*, **2003**, *123*, 200.

(7) Minh, N. *Solid State Ionics*, **2004**, *174*, 271.

(8) Pornprasertsuk, R.; Ramanarayanan, P.; Musgrave, C.; Prinz, F. *J. Appl. Phys.*, **2005**, *98*, 103513.

(9) Vernoux, P.; Guth, M.; Li, X. *Electrochem. Solid-State Lett.*, **2009**, *12*, E9.

(10) Guo, X. *Solid State Ionics*, **1995**, *81*, 235.

(11) Haering, C.; Roosen, A.; Schichl, H. *Solid State Ionics*, **2005**, *176*, 253.

(12) Swider, K.; Worrell, W. *J. Electrochem. Soc.*, **1996**, *143*, 3706.

(13) Hattori, M.; Takeda, Y.; Sakaki, Y.; Nakanishi, A.; Ohara, S.; Mukai, K.; Lee, J.; Fukui, T. *J. Power Sources*, **2004**, *126*, 23.

(14) Hattori, M.; Takeda, Y.; Lee, J.; Ohara, S.; Mukai, K.; Fukui, T.; Takahashi, S.; Sakaki, Y.; Nakanishi, A. *J. Power Sources*, **2004**, *131*, 247.

(15) Levy, M.; Fouletier, J.; Kleitz, M. *J. Electrochem. Soc.*, **1988**, *135*, 1584.

(16) Hirabayashi, D.; Tomita, A.; Brito, M.; Hibino, T.; Harada, U.; Nagao, M.; Sano, M. *Solid State Ionics*, **2004**, *168*, 23.

(17) Fu, Q.; Mi, S.; Wessel, E.; Tietz, F. *J. Eur. Cerm. Soc.*, **2008**, *28*, 811.

(18) Hui, S.; Petric, A. *J. Electrochem. Soc.*, **2002**, *149*, J1.

(19) Zhu, H.; R. Kee, R. *J. Elecrochem. Soc.*, **2006**, *153*, A1765.

(20) Kakac, S.; Pramuanjaroenkij, A.; Zhou, X. *Int. J. Hydrogen Energy*, **2007**, *32*, 761.

(21) Manning, P.; Sirman, J.; Souza, R.; Kilner, J. *Solid State Ionics*, **1997**, *100*, 1.

(22) Hassel, B.; Boukamp, B.; Burggraaf, A. *Solid State Ionics*, **1992**, *53-56*, 890.

(23) Ridder, R.; Welzenis, R.; Brongersma, H.; Kreissig, U. *Solid State Ionics*, **2003**, *158*, 67.

(24) Svensson, A.; Sunde, S.; Nisancioglu, K. *J. Electrochem. Soc.*, **1997**, *144*, 2719.

(25) Perry, C.; Feinberg, A. *Solid State Commun.*, **1980**, *36*, 519.

(26) Perry, C.; Feinberg, A.; Currat, R. *Bull. Amer. Phys. Soc.*, **1981**, *26*, 405.

(27) Pomfret, M.; Stoltz, C.; Varughese, B.; Walker, R. *Anal. Chem.*, **2005**, *77*, 1791.

(28) Zhu, W.; Deevi, S.; *Mater. Sci. Eng. A*, **2003**, *362*, 228.

(29) Feinberg, A.; Perry, C. *J. Phys. Chem. Solids*, **1981**, *42*, 513.

(30) Lui, D.; Perry, C.; Ingel, R. *J. Appl. Phys.*, **1988**, *64*, 1413.

(31) Svensson, A.; Sunde S.; Nisancioglu, K. *J. Electrochem. Soc.*, **1998**, *145*, 1390.

(32) Sammes, N.; Cai, Z. *Solid State Ionics*, **1997**, *100*, 39.

(33) Lee, J.; Yoon, S.; Kim, B.; Kim, J.; Lee, H.; Song, H. *Solid State Ionics*, **2001**, *144*, 175.

(34) Goodenough, J. *Annu. Rev. Mater. Res.*, **2003**, *33*, 91.

(35) Devanathan, R.; Weber, W.; Singhal, S.; Gale, J. *Solid State Ionics*, **2006**, *177*, 1251.

(36) Martinez, A.; Brouwer, J. *J. Power Sources*, **2010**, *195*, 7268.

(37) Kenney, B.; Valdmanis, M.; Baker, C.; Pharoah, J.; Karan, K. *J. Power Sources*, **2009**, *189*, 1051.

(38) Janardhanan, V.; Heuveline, V.; Deutschmann, O. *J. Power Sources*, **2008**, *178*, 368.

(39) Zhu, W.; Ding, D.; Xia, C. *Electrochem. Solid-State Lett.*, **2008**, *11*, B83.

(40) Fukunaga, H.; Ihara, M.; Sakaki, K.; Yamada, K. *Solid State Ionics*, **1996**, *86-88*, 1179.

(41) Schmidt, M.; Hansen, K.; Norrman, K.; Mogensen, M. *Solid State Ionics*, **2009**, *180*, 431.

(42) Sukeshini, A.; Habibzadeh, B.; Becker, B.; Stoltz, C.; Eichhorn, B.; Jackson, G. *J. Electrochem. Soc.*, **2006**, *153*, A705.

(43) Mizusaki, J.; Tagawa, H.; Saito, T.; Kamitani, K.; Yamamura, T.; Hirano, K.; Ehara, S.; Takagi, T.; Hikita, T.; Ippomatsu, M.; Nakagawa, S.; Hashimoto, K. *J. Electrochem. Soc.*, **1994**, *141*, 2129.

(44) Li, Y.; He, D.; Zhu, Q.; Zhang, X.; Xu, B. *J. Catal.*, **2004**, *221*, 584.

(45) Eder, D.; Kramer, R. *Phys. Chem. Chem. Phys.*, **2002**, *4*, 795.

(46) Wachsman, E.; Jiang, N.; Frank, C.; Mason, D.; Stevenson, D. *Appl. Phys. A.*, **1990**, *50*, 545.

(47) Eigenbrodt, B.; Pomfret, M.; Steinhurst, D.; Owrutsky, J.; Walker, R. *J. Phys. Chem. C.*, **2011**, *115*, 2895.

(48) Pomfret, M.; Marda, J.; Jackson, G.; Eichhorn, B.; Dean, A.; Walker, R. *J. Phys. Chem. C.*, **2008**, *112*, 5232.

(49) Pomfret, M.; Owrutsky, J.; Walker, R. *J. Phys. Chem. B*, **2006**, *110*, 17305.

(50) Pomfret, M.; Owrutsky, J.; Walker, R. *Anal. Chem.*, **2007**, *79*, 2367.

(51) Stohr, J.; H.C.S., ed., *Magnetism From Fundamentals to Nanoscale Dynamics*, ISBN 3-540-30282-4, Springer

(52) Nakajima, R.; Stohr, J.; Idzerda, Y. *Phys. Rev. B*, **1999**, *59*, 6421.

(53) Jablonski, A.; Powell, C. *J. Electron. Spectrosc. Relat. Phenom.*, **1999**, *100*, 137.

(54) Jablonski, A.; Powell, C. *Surf. Sci.*, **2005**, *551*, 106.

(55) Frazer, B. *Surf. Sci.*, **2003**, *537*, 161.

Chapter 4: Direct, *In Situ* Optical Studies of Ni/YSZ Anodes in Solid Oxide Fuel Cells Operating with Methanol and Methane

1. Introduction

Solid oxide fuel cells (SOFCs) are solid state electrochemical devices that have attracted considerable attention as sources of efficient, low emission, DC electricity. In combined heating and power applications, SOFCs can operate with efficiencies as high as 80 %, and because fuel is electrochemically oxidized, these devices do not produce significant amounts of NO_x or SO_x pollutants. SOFCs are also attractive energy-producing devices because they are fuel flexible and able to operate with complex fuel mixtures, including hydrocarbons and oxygenated fuels.[1-11] The high operating temperatures of SOFCs ($\geq$ 650˚C) can lead to significant fuel reforming, meaning that higher molecular weight fuels often break down into simpler, more labile species prior to reaching electrochemically active anode sites. Fuel flexibility coupled with the relatively high tolerance to contaminants confer to SOFCs distinct advantages[9] over other devices such as polymer electrolyte membrane fuel cells (PEMFCs) and direct methanol fuel cells (DMFCs), where species such as CO deactivate electrochemically active sites. Furthermore, SOFCs can be manufactured from relatively inexpensive materials and can be integrated easily into stacked systems for use in commercial applications where CO is often a significant species in the fuel feed.[2,12-14]

While the overall description of SOFC operation is straightforward, detailed, validated mechanisms describing the processes occurring on SOFC cathodes and

anodes are more tenuous.[15,16] The high activation energy for oxygen ion diffusion through the electrolyte and the large barrier to molecular oxygen activation at the cathode require that SOFCs operate at high temperatures. This condition poses significant experimental challenges for studying SOFC chemistry *in situ* and in real time. In particular, most experimental approaches used to study SOFC chemistry are limited in their ability to identify directly mechanisms responsible for SOFC degradation and failure. Electrochemical measurements can correlate declining performance with specific operating conditions, but these studies can not isolate the chemical or structural evolution in the device responsible for the observed change(s). *Ex situ* studies provide important information about the final state of materials that comprise individual SOFC components, but these studies can be carried out only after a SOFC has been cooled and disassembled. The goal of the work presented below is to identify *in situ* and in real time the changes occurring on SOFC anodes operating with either methane (CH_4) or methanol (CH_3OH).

One major source for SOFC degradation is the formation of carbon deposits.[8,9,17,18] Carbon formed from incomplete oxidation of hydrocarbon fuels or from large carbon clusters nucleated from gas-phase pyrolysis reactions is thought to block electrocatalytic sites on SOFC anodes leading to lower overall fuel conversion efficiencies and eventual anode failure.[13,19,20] This process is particularly problematic on Ni-based anodes since they are effective hydrocarbon cracking catalysts. Models describing carbon growth have been developed without direct evidence of when and where carbon deposits start to form, how quickly deposited carbon grows, and how cell conditions affect the rates and mechanisms of carbon growth.[21-26]

Only recently have optical methods such as vibrational spectroscopy and near-infrared (NIR) imaging shown the ability to monitor carbon deposition and temperature changes associated with carbon formation and oxidation on Ni/yttria-stabilized zirconia (YSZ) cermet SOFC anodes as a function of fuel type, cell polarization, and temperature.[21,27] These studies were used to examine the formation of graphitic carbon from various low molecular weight, saturated hydrocarbons. Both Raman spectroscopy and thermal imaging of operating SOFC anodes indicated that more carbon deposition occurred with higher molecular weight hydrocarbon fuels. Optical results were correlated directly with electrochemical data acquired from the same devices. For example, vibrational Raman spectroscopy showed that polarizing a SOFC changed the structure of carbon deposited from fuels such as butane and ethylene, compared to that of carbon formed from similar exposures when the cell was at open circuit voltage (OCV).[27] In the thermal imaging experiments, endothermic cracking of hydrocarbon fuels resulted in a lower anode temperature at OCV, and the amount of carbon deposited was identified by terminating the fuel flow and tracking the temperature increase due to electrochemical oxidation of carbon and the Ni in the anode structure.[20]

In experiments described below, we combine these two optical methods, vibrational Raman spectroscopy and NIR imaging, to compare the effects of CH_4 and CH_3OH at the anode on SOFC performance and the tendency of each fuel to form carbon deposits. Previous work has shown that CH_4 is relatively unreactive in SOFCs with more than 50 % of a dry CH_4 feed passing through the anode region without undergoing oxidation.[28] Subsequent kinetic modeling showed that under most SOFC

conditions (T < 900˚C) CH_4 does not undergo gas-phase pyrolysis.[29] Finally, *in situ* spectroscopic data demonstrated that even under OCV conditions Ni-based cermet anodes were not very susceptible to carbon formation when exposed to a direct, dry CH_4 feed for up to one hour.[10]

The behavior of CH_3OH as a fuel in SOFC applications is less well understood. When used dry, oxygenated fuels can be less prone to forming carbon than similarly sized saturated hydrocarbons.[21,30-33] However, since oxygenated fuels also have lower bond dissociation enthalpies, they can more rapidly chemisorb to surfaces, thereby increasing surface carbon coverage and the opportunity for carbon deposition.[34,35] Studies by Jiang and Virkar reported no evidence of carbon penetration into SOFC anodes based on *ex situ* SEM data from anodes that had operated with a direct CH_3OH feed.[36] More recently, Mat et al. reported that at temperatures below 600˚C CH_3OH does not form carbon on SOFC anodes, but ethanol does.[37] These latter experiments used Ni/YSZ-doped ceria composite materials rather than the simple Ni/YSZ cermets employed by Jiang and Virkar.

In contrast to these findings, numerous other authors have observed that CH_3OH used directly as a fuel can form graphite on SOFC anodes unless operating temperatures are > 800°C or if the fuel feed is mixed with steam.[33,38,39] Whether these carbon deposits form from methanol itself or from products of methanol reforming, remains an open question. Several studies have quantified the equilibrium distributions of products resulting from CH_3OH pyrolysis,[32,38-40] but whether the reactants in SOFC fuel feeds reach equilibrium or contain a nonequilibrium distribution of species will depend sensitively on device design, flow rates, and partial

pressures and device load. At temperatures above 1000˚C, CH_3OH converts mostly into CO and H_2.[39] At lower temperatures (< 800˚C), dry CH_3OH will form a mixture of products that show a strong tendency to form carbon deposits on Ni-based anode materials.[32,38] Interpreting data from CH_3OH-operated SOFCs, therefore, requires careful characterization of the specific experimental assembly and operating conditions.

What is clear from the comparisons cited above is that the mechanism(s) responsible for carbon formation on Ni-based cermet anodes in SOFCs are largely inferential without direct evidence about when, how, or where carbon forms, if, in fact, carbon even forms at all. Data from our *in situ* optical experiments show that CH_4 and CH_3OH have markedly different effects on anode processes as indicated by systematic changes in anode temperatures as well as the propensity to form carbon deposits. While the adverse effects of CH_4 on SOFC performance are minimal and consistent with previous reports, CH_3OH forms significant amounts of carbon on Ni cermet anodes, and these deposits degrade the device's performance. These results begin to resolve questions of whether or not oxygenated fuels can form carbon on operational SOFC anodes and how the tendency of these fuels to form carbon depends on cell polarization conditions.

2. Experimental

2A. SOFC Membrane Electrode Assembly

The electrolyte-supported SOFCs used in these experiments are similar to those used in previous studies.[10,27,41] The electrolyte-supported membrane electrolyte assemblies (MEAs) consist of a 30 ± 5 μm thick, sintered, Ni/YSZ cermet anode

(50 % Ni by mass) and a 30 ± 5 μm thick, sintered, LSM/YSZ cermet cathode. The electrolytes are ~ 2.5 cm in diameter and 0.80 ± 0.02 mm thick YSZ disks and are fabricated in our laboratories. Details regarding the actual construction of these devices can be found in refs 10, 27, and 41. Platinum paste (Heraeus) was used to attach platinum mesh (Alfa Aesar) and gold wire (Alfa Aesar) to the cathode as a current collector, while gold paste (Heraeus) and gold wire were used as a current collector on the anode.

2B. Electrochemical Measurements

All electrochemical measurements and overpotential conditioning experiments were carried out using a Gamry Instrument PCI4 Potentiostat/Galvanostat/ZRA. In a typical experiment, the SOFC was first tested with a mixture of 108 sccm argon and 100 sccm hydrogen. Similar measurements were performed throughout an experimental run and compared to initial benchmark results to assess device durability. Linear sweep voltammetry (LSV) and electrochemical impedance spectroscopy (EIS) measurements were taken over a 30 min. period to examine how the fuels in question affected electrochemical performance over time. Graphite growth kinetics was monitored at OCV and two different overpotentials, 0.30 and 0.60 V, where overpotential refers to the polarization across the cell relative to OCV (-1.15 ± 0.05 V).

2C. Optically Accessible SOFCs

A unique requirement of these studies compared to more traditional SOFC experiments is the need for optical access so that Raman and thermal imaging experiments can be performed. Two systems were used in the studies reported below.

One assembly is designed for Raman studies[27,41] and the other for thermal imaging.[20] The Raman assembly employs a microscope for excitation and scattering collection normal to the anode. Even though a long working distance objective (15 mm) is used, the objective itself sits reasonably close to the cell, requiring the MEA to be < 720˚C to avoid thermal damage to the collection optics. This requirement is met by heating the furnace so that the middle of the assembly reaches a temperature of 1000˚C. A consequence of this design is that the fuel traverses this high temperature region on its way to the anode.

In contrast to the Raman spectrometer assembly, the detector used for thermal imaging operates in free space and can be up to a meter from the heated anode. In the thermal imaging assembly, the MEA is often situated in the center of the furnace in the highest-temperature region (715˚C). As noted below, while it is possible for reforming to occur, especially with methanol reforming to make CO, CO_2, and H_2, we have confirmed that the fuel incident on the anode is primarily methanol in both experimental assemblies. Furthermore, several control experiments were carried out on the Raman instrument where both Raman and thermal imaging data were acquired simultaneously. The imaging data were of slightly poorer quality because of geometric constraints, but results verified that conclusions drawn from the individual experimental assemblies were internally and quantitatively consistent.

2D. *In situ* Raman SOFC Assembly

The complete SOFC assembly has been described previously.[27,41] As indicated above, a quartz optical window covers the anode for optical access. In Raman scattering experiments, 488 nm light (8 mW) is focused onto the anode, and

the backscattered signal is detected with a microscope/charge-coupled detector (CCD) assembly (Renishaw inVia). The anode temperature was maintained at 715˚C by direct thermocouple monitoring. The SOFC assembly is surrounded by an open-ended, high-temperature furnace whose center is kept at 1000˚C. The thermal gradient between the middle of the furnace and the exposed anode window is responsible for the 715˚C MEA operating temperature. All gases to the cathode and to the anode pass through the high temperature region of the furnace, meaning that the CH_3OH fuel spends ~ 0.03 sec. above 900˚C. To determine the composition of the gas mixture reaching the SOFC anode, exhaust composition was quantified using FTIR spectroscopy. These measurements showed that for the conditions used in these studies, ~ 80 % of the CH_3OH survived transit through the high temperature region of the furnace and reached the anode intact, Figure VI.1. The balance of the fuel mixture consisted primarily of CO and, presumably, H_2.

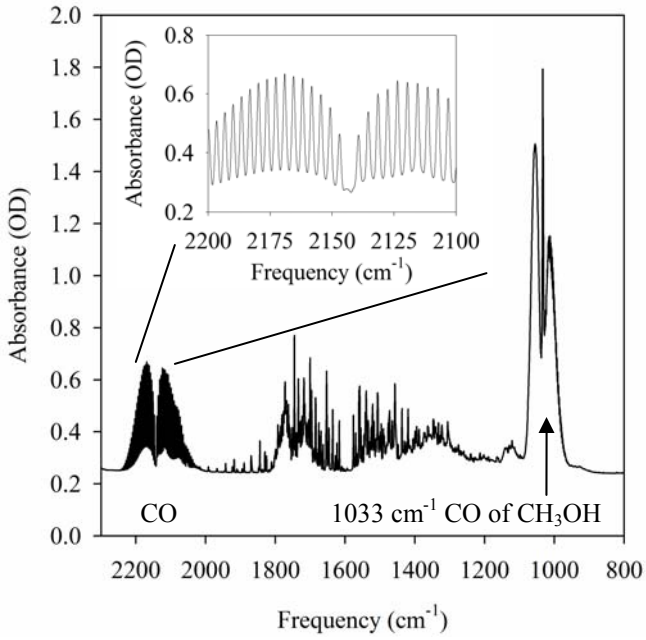

Figure IV.1. IR spectrum of a 150 sccm CH_3OH/Ar flow after passing through an open-ended furnace with a set temperature of 1000˚C in the center.

2E. Gas Flows for Raman Measurements

Air (to the cathode) and argon/fuel mixture (to the anode) flows were controlled using rotameters. CH_3OH was introduced to the SOFC using a bubbler. A carrier gas of argon was used to transport the vapor into the fuel cell chamber at a flow rate of 108 sccm through 4.5 mm inner-diameter feed tubes. Given CH_3OH's vapor pressure of 97 Torr at 20˚C, the amount of CH_4 (with a backing pressure of 1 atm) was adjusted to ensure that cells operated with the two fuels feeds containing equivalent carbon loads.

2F. Thermal Imaging Measurements

Thermal images were acquired with a 14-bit, 656 by 492 pixel, CCD camera (Allied Vision Technologies, Stingray F033B ASG) with a telephoto lens (Navitar, Zoom 7000) using collection software written in-house in LabView v8.5. A long-pass filter (Hoya R72), with a nominal cutoff wavelength of 720 nm, was used to block visible light from the anode and surrounding surfaces. Details, including temperature and spatial resolutions for this system, have been reported previously.[20,42] In the *in situ* Raman assembly, the intensity reading on the camera was calibrated to a thermocouple located adjacent to the anode. Intensity readings were taken while the furnace was set to 950˚C (thermocouple temperature of ~ 635˚C) and 1000˚C (thermocouple temperature of ~ 670˚C), and a linear calibration was generated based on these two temperature readings. All data were collected at 2-5 Hz, stored as intensity per pixel, and displayed as temperature-calibrated images and time series. Full details of this assembly and system calibration have been published previously in ref 20.

3. Results

3A. Electrochemical Characterization

Figure IV.2 shows the electrochemical performance of cells with CH_3OH (a and b) and CH_4 (c and d) as measured by LSV (a and c) and EIS (b and d). EIS data are acquired with cells polarized at 0.10 V relative to OCV. Cells exposed to CH_3OH suffer a ~ 15 % reduction in power and show significant changes in their impedance spectra. Exposure to CH_4 also leads to a modest reduction in SOFC performance as shown in the LSV data, but the impedance characteristics are largely unchanged. All observed effects are reversible. When the anode is oxidized (with air) and reconstituted with H_2, device performance recovers to the initial benchmarks measured with H_2 at the beginning of the experiment.

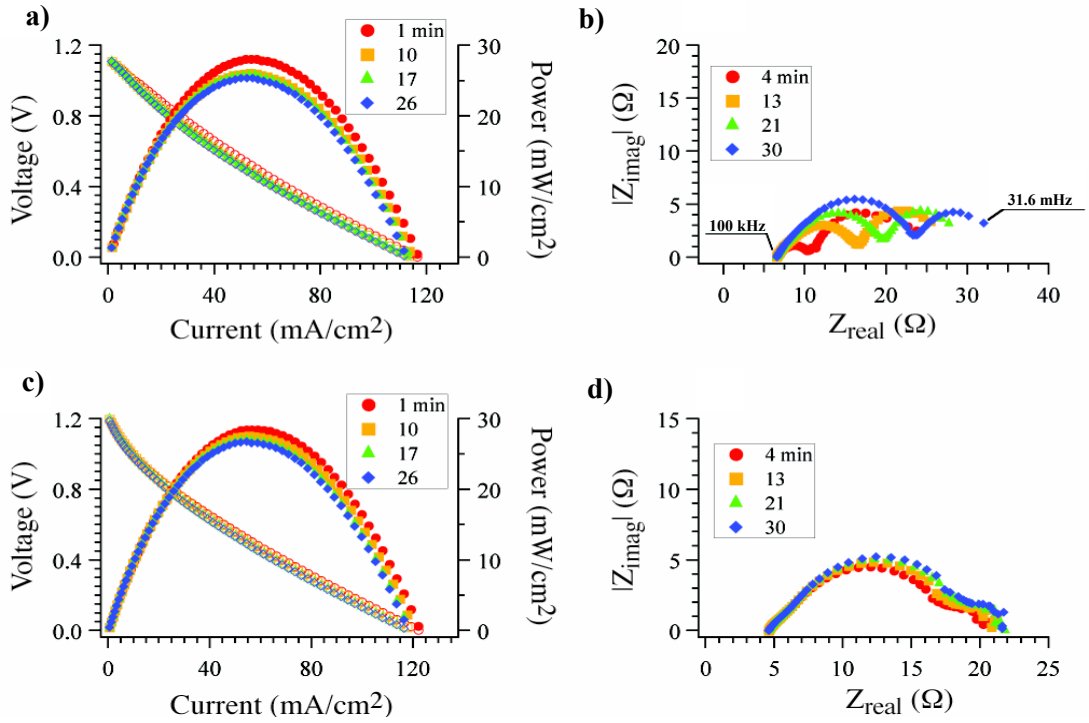

Figure IV.2. Electrochemical data for SOFCs operating with CH_3OH (a and b) and CH_4 (c and d). Experiments were carried out in a sequential manner as noted in the legends under constant exposure to the fuel. Impedance measurements (b and d) were performed with MEAs polarized to 0.1 V vs OCV with an amplitude of 10 mV on the AC impedance wave. The frequency of the impedance wave varied between 100 kHz (at low impedance) and 31.6 mHz (at high impedance). Peak frequencies for methanol: ~ 100 Hz (high frequency arc), ~ 12.5 Hz (middle frequency arc), and ~ 63.1 mHz (low frequency arc). Peak frequencies for methane: ~ 63 Hz (high frequency arc), ~ 6.3 Hz (middle frequency arc), and ~ 320 mHz (low frequency arc)

EIS data from the cell exposed to CH_3OH show striking changes as a function of exposure time. On the basis of previous studies,[43,44] the EIS data shown in Figure IV.2 are fit to four elements in series in an equivalent circuit (Scheme IV.1, Table IV.1). The bulk resistance (R_{Bulk}) refers simply to the resistance associated with oxide diffusion through the electrolyte. The other three elements are RC circuits, and the frequency dependence of these three elements is assigned to different processes occurring in the working SOFC.[43,44] From numerous experiments, we infer

that the highest frequency arc, at low Z_{real} impedances, is associated with cathodic processes and remains unchanged from prolonged exposures to carbon containing fuels. Also from these experiments we observe that with the formation of graphite from prolonged exposures to these same fuels there is an increase in both impedance components in the middle and high frequency arcs inferring that these arcs are associated with anodic processes. While the CH_4 EIS data remain insensitive to the degree of exposure, the total polarization resistance, defined as the impedance between the two x-intercepts, grows significantly as a function of exposure to CH_3OH. Table VI.1 summarizes the EIS data. We note that quantitative details (such as polarization and bulk resistances and the absolute magnitudes of the individual impedances) can vary from cell to cell, but the observed behaviors and relative magnitude of the changes are general and reproducible. The single quantity most responsible for the changing impedance spectra is the magnitude of R_2, the intermediate frequency arc assigned to changes in the chemistry occurring at the SOFC anode. As will be noted below, this growth in impedance correlates directly with the kinetics of graphite growth observed in the *in situ* Raman data acquired from the same assembly.

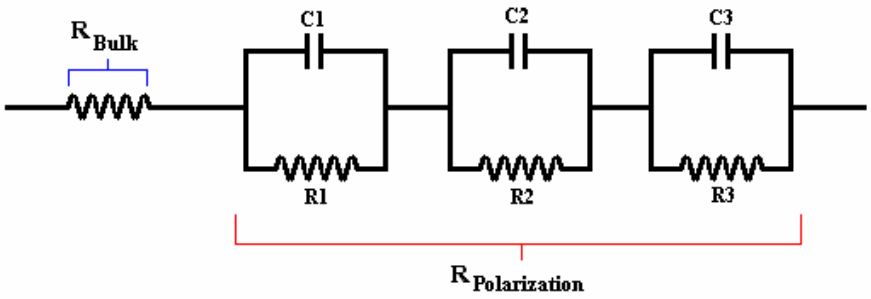

Scheme IV.1. Equivalent circuit used in the modeling of EIS spectra. Results are tabulated below in Table IV.1.

Methanol						
	R_{bulk}	R_{pol}	R_1	R_2	R_3	%C
4 min	6.75 ± 0.1	12.70	2.11 ± 0.2	2.06 ± 0.3	8.53 ± 0.7	17.74
13 min	6.62 ± 0.1	18.24	2.58 ± 0.3	6.97 ± 0.3	8.69 ± 0.8	72.60
21 min	6.68 ± 0.1	20.80	2.90 ± 0.3	9.44 ± 0.4	8.46 ± 0.9	86.79
30 min	6.73 ± 0.1	24.29	3.57 ± 0.3	12.39 ± 0.4	8.33 ± 1.0	100.00
Methane						
	R_{bulk}	R_{pol}	R_1	R_2	R_3	%C
4 min	4.61 ± 0.1	15.10	1.88 ± 0.1	9.39 ± 0.2	3.83 ± 0.3	36.22
13 min	4.64 ± 0.1	15.86	1.90 ± 0.1	10.12 ± 0.2	3.84 ± 0.3	78.75
21 min	4.67 ± 0.1	16.25	1.90 ± 0.1	10.39 ± 0.3	3.96 ± 0.3	90.75
30 min	4.68 ± 0.1	16.62	1.93 ± 0.1	10.80 ± 0.3	3.89 ± 0.3	100.00

Table IV.1. Impedance values determined from fitting EIS spectra shown in Figure VI.2 to a model that has a resistive element followed by three consecutive RC circuit elements in series. Here, R_{bulk} refers to the high-frequency intercept of the impedance data with the x-intercept. R_{pol} or the polarization resistance represents the sum of R_1, R_2, and R_3. These individual resistances are associated with cathodic, anodic, and mass transfer processes, respectively. % C is calculated by *in situ* Raman measurements and related to the relative graphite peak intensity compared to the absolute asymptotic peak intensity created by prolonged exposures of either methanol or methane.

3B. Near Infrared Thermal Imaging

Differences in the condition of anodes exposed to CH_3OH and CH_4 are clearly evident in the thermal imaging experiments. Figure IV.3 shows the thermal characteristics of SOFCs exposed to both fuels at OCV. Figure IV.3a is a false-color, temperature-calibrated image of a cell operating with a H_2/Ar fuel feed. Figure IV.3b is the image of the same cell after 10 min. of CH_4 flow. The small temperature change is hardly noticeable in the image as the anode appears only slightly more blue indicating that the anode surface has cooled by only -0.5 ± 0.7˚C. This temperature

change is considerably less than previously reported for CH_4 in anode-supported SOFCs, this is most likely attributed to the reduced anode volume of the electrolyte-supported cells.[20] Figures IV.3c and 3d show data for an anode exposed to H_2 and after 10 min. of CH_3OH, respectively. In contrast to the methane data, anodes exposed to CH_3OH show a large temperature change ($-5.5 \pm 0.7^{\circ}C$) when the fuel is changed from H_2 to CH_3OH. This result corroborates Raman data shown below and implies that the endothermic hydrocarbon cracking and carbon growth are occurring much faster with CH_3OH than with CH_4. Spatially, the $\sim 12\ mm^2$, triangular area immediately in front of the fuel inlet (the inlet is located in the center just out of frame of the bottom of the image) appears to be the coolest part of the anode, suggesting, not surprisingly, that more carbon deposition is occurring in the region having the highest relative fuel density.

Figure IV.3e shows the evolution of anode surface temperature for each of the cells described above. The time profiles of the cells vary greatly with the fuel used. In the cell operated with CH_4 (red trace), the temperature initially rises, probably due to temporary fuel abundance as the anode gas mixture transitions from H_2 to CH_4. As discussed above, CH_4 is relatively unreactive (compared to other fuels such as H_2, CO, C_2H_2, etc.) and forms only limited amounts of carbon on Ni cermet anodes. Once carbon formation begins, the cell cools to a steady-state temperature just below the initial cell temperature. The blue trace shows the anode temperature over the course of 10 min. while operating with CH_3OH. Unlike with CH_4, the cermet anode cools immediately upon introduction of CH_3OH, and the temperature change is 10-fold greater than observed for CH_4.

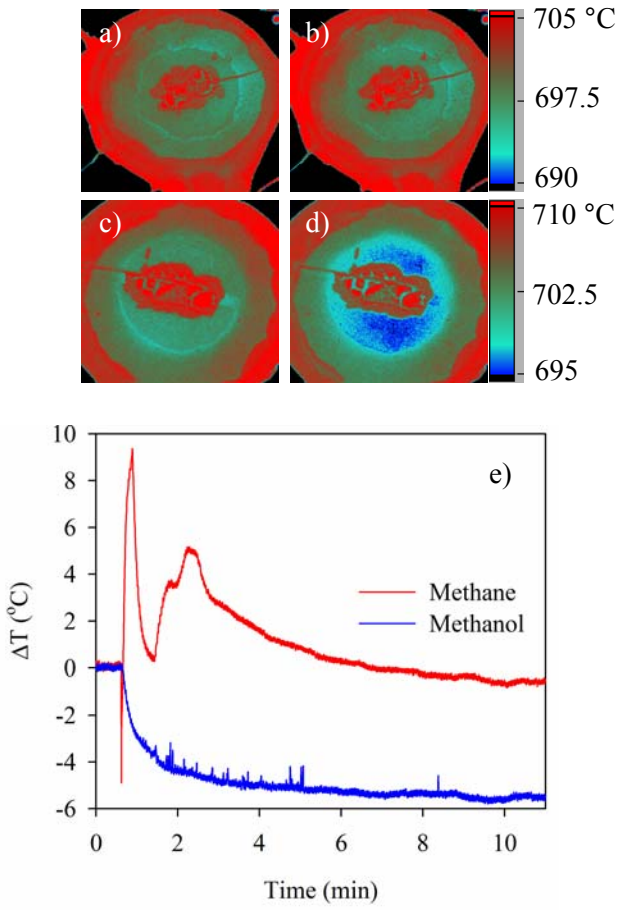

Figure IV.3. Thermal images of SOFCs at OCV are shown (a) while H_2 is used as a fuel prior to CH_4 use, (b) after 10 min. of exposure to CH_4 fuel, (c) while H_2 is used as a fuel prior to CH_3OH use, and (d) after 10 min. of exposure to CH_3OH. The changes in anode surface temperature that resulted from CH_4 and CH_3OH fuel flows over the course of 11 min. are plotted in (e).

3C. *In Situ* Vibrational Raman Spectroscopy

While imaging methods can resolve spatial variations in the thermal conditions across SOFC components, these techniques cannot identify with material or molecular specificity the species present. Optical spectroscopy, vibrational spectroscopy in particular, is uniquely well suited for *in situ* observation of specific molecular and material species. Figures IV.4a and 4b show a sequence of spectra that indicate the relative amounts of carbon on Ni/YSZ cermet anodes held at OCV and

exposed to either CH_3OH (Figure IV.4a) or CH_4 (Figure IV.4b). Each spectrum represents a 1 min. acquisition. Only every fifth spectrum is shown for clarity. Several observations stand out. First, the strongest feature observed in both series of spectra is a sharp band at ~ 1560 cm^{-1}. This is often referred to as the "G" band in the literature and is characteristic of highly ordered graphite having very few defects and/or grain boundaries.[10,27,41] The fact that this feature appears for both fuels provides definitive evidence that both fuels, CH_3OH and CH_4, are capable of forming carbon deposits on Ni/YSZ cermet anodes and that these carbon deposits consist of primarily sp^2 hybridized carbon. The spectra allow us to say that, within our detection limits, very little if any saturated carbon grows on the cermet anode, given the absence of any observable intensity in the 2800-3100 cm^{-1} region of the spectrum (data not shown).

The second observation is that higher sensitivity spectra with longer acquisition times show evidence of a small feature at ~ 1340 cm^{-1} in the Raman data of the graphite formed only by CH_3OH (Figure IV.4c). This feature, the "D" peak, is a signature of carbon with nongraphitic characteristics, including disorder in the extended graphite network due to vacancies and grain boundaries. Figure IV.4d plots the intensity of the 1560 cm^{-1} band for both fuels as a function of exposure in 1 min. intervals and highlights a third observation: under the conditions tested in these studies, CH_3OH forms much more carbon on the Ni/YSZ cermet anode than CH_4. Furthermore, graphite growth from both fuels appears to be self-limiting, as both traces approach asymptotic limits. Net graphite growth from CH_3OH slows after ~ 20 min. and ceases after 30 min. Net graphite growth from CH_4 reaches its terminal

limit after ~ 5 min. A final interesting observation from the data plotted in Figure IV.4d is that at early times (≤ 5 min.) the kinetics of graphite growth are very similar regardless of fuel identity. This similarity implies that carbon deposits formed by each fuel form initially via a similar mechanism but that a second mechanism provides the more reactive fuel with additional pathways for carbon growth.

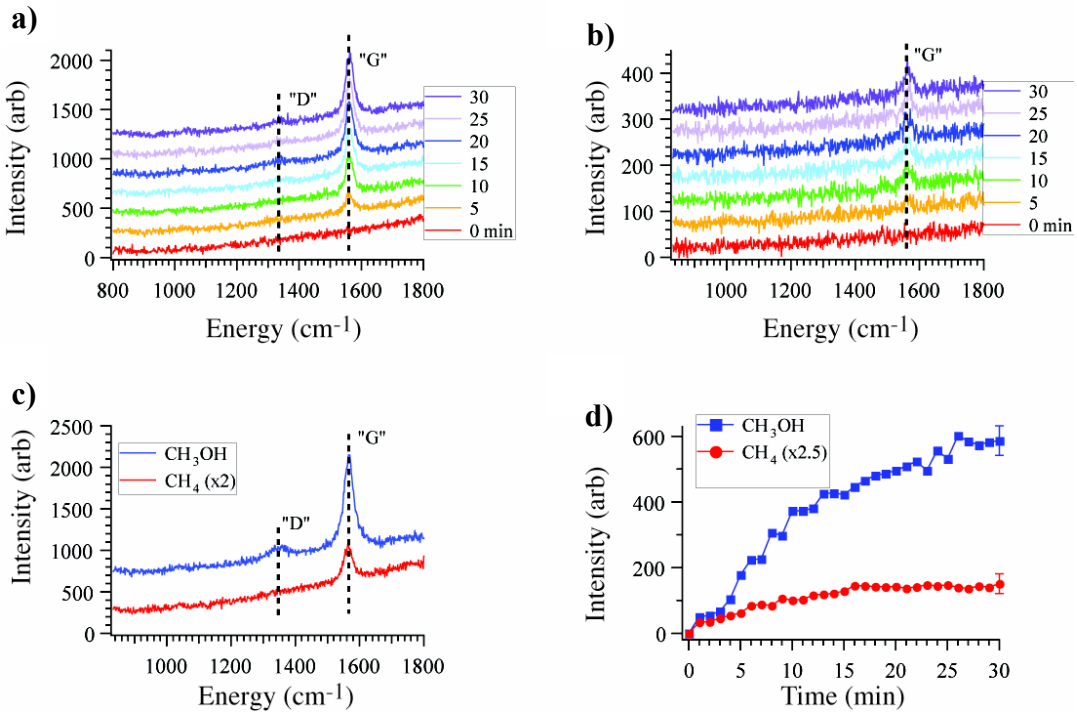

Figure IV.4. *In situ* Raman measurements taken at 715˚C under OCV conditions. (a) Graphite growth as a function of exposure to CH_3OH. From bottom to top, each spectrum represents a ~ 1 min. acquisition acquired after every 5th min. (b) Same as (a) except for exposure to CH_4. (c) Higher-resolution scans of anodes after 30 min. of exposure to CH_3OH (blue) and CH_4 (red). Each scan represents a 2.5 min. acquisition. (d) Intensity of the graphite G band at ~ 1560 cm^{-1} as a function of time for anodes exposed to CH_3OH (blue) and CH_4 (red).

3D. Polarization Dependence of Carbon Formation

The data in Figure IV.5 show that the temperature changes become slightly less negative for both fuels when the cell is polarized. This effect is likely the result

of the added oxide flux leading to increased (exothermic) fuel oxidation and diminished carbon deposition. Overall, however, the temperature of operating SOFC anodes still shows a net decrease indicating that fuel cracking and carbon deposition remain the dominant contributors to the anode temperature. Additional thermal imaging data showing temperature changes resulting from operating the device under "fuel deficient" conditions are presented in the Figure IV.6.

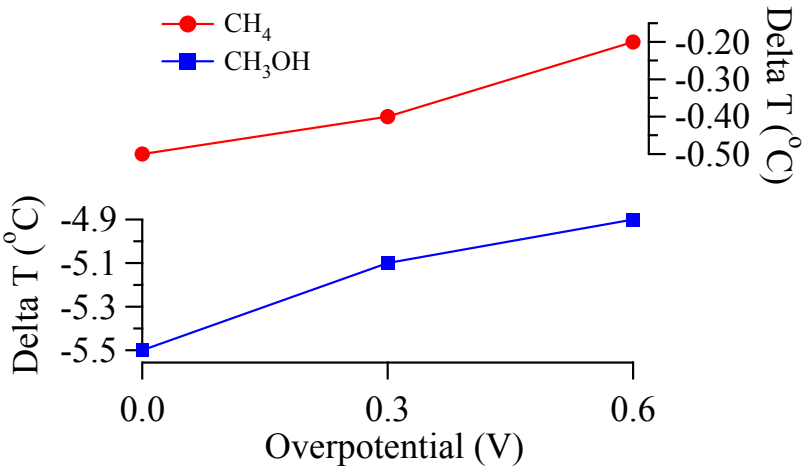

Figure IV.5. Changes in steady state anode temperature after exposure to (a) CH_4 and (b) CH_3OH on SOFC anodes (at ~ 700˚C), while the cells are held at OCV and polarized to overpotentials of 0.30 and 0.60 V. Uncertainties in the ΔT values are ± 0.7˚C.

Thermal imaging results have primarily been described in terms of the anode temperature changes associated with endothermic internal reforming or cracking of methanol and, to a lesser extent, methane fuels. As indicated briefly in the paper, the relative amount of carbon can be indirectly evaluated from the temperature rise that accompanies electrochemical oxidation of the deposited carbon after exposure to carbon-containing fuels. This method has been previously described with regards to anode-supported SOFCs operating on hydrogen, methane and propane.[20,42] In the

present case of the electrolyte-supported cells, they are polarized such that approximately 65 % of the maximum current is drawn (approximately 100 mA, with an overpotential of ~ 0.8 V) and all fuel flows are terminated so that the anode is under Ar exclusively. Under these conditions, the oxide flux through the electrolyte oxidizes the Ni in the anode and any material – i.e., carbon – that is present on the anode. Figure IV.6 shows the time series for this set of experiments on anodes that had previously been exposed to (a) CH_4 and (b) CH_3OH. The plot shows that as the carbon deposits are burned off, both anodes heat. Once the exothermic oxidation of the anode and the deposited carbon are complete the surface cools as expected. Two features of the plot that indicate there is more carbon on the anode that has been exposed to CH_3OH are: The increase in temperature is ~ 0.5˚C more with CH_3OH compared to CH_4 and the anode exposed to CH_3OH takes ~ 1 min. longer than the anode exposed to CH_4 to return to the initial temperature. These heating profiles are a direct measurement of oxidation processes on the SOFC anode and further support the results that suggest more carbon forms with CH_3OH than with CH_4, as seen in the Raman data and the temperature decrease under fuel conditions.

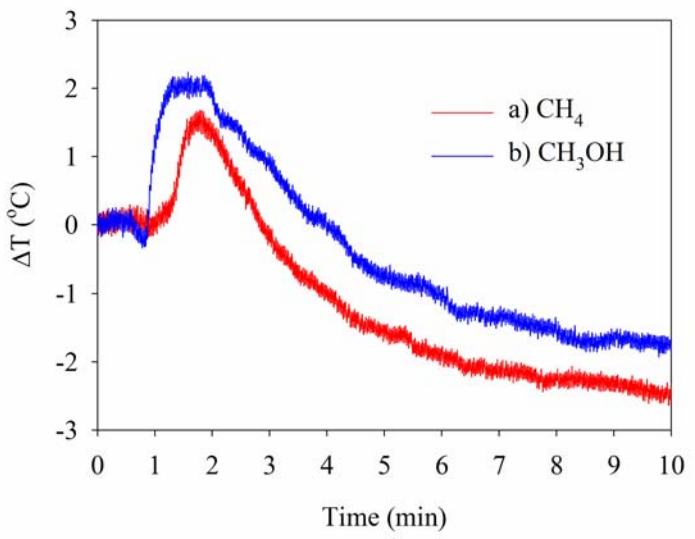

Figure IV.6. Changes in steady state anode temperature as 100 mA is drawn from the cell under fuel deficient conditions. The data are taken after the anodes have been exposed to a) CH_4 and b) CH_3OH.

The thermal imaging results imply that less graphite forms on the anode when the cell is polarized. *In situ* Raman data shown in Figure IV.7 independently confirm this assertion. Graphite growth kinetics for SOFCs at OCV and polarized to 0.30 and 0.60 V are shown in Figure IV.7. Again, plotted data refer to the peak intensity of the 1560 cm^{-1} "G" band in Raman spectra acquired once every minute from anodes exposed to CH_3OH (top) and CH_4 (bottom). The kinetic traces show a clear reduction in the total amount of graphite formed as the cell is subjected to higher overpotentials. This effect is much more pronounced for CH_3OH than for CH_4. Graphite formed from CH_3OH shows a 4-fold reduction in the 1560 cm^{-1} feature at 0.60 V polarization as compared to OCV. Intermediate amounts of graphite accumulate at a cell overpotential of 0.30 V. Polarizing cells exposed to CH_4 appear to have little effect on the amount of graphite formed. Even at high overpotential (0.60 V), the amount of carbon formed on the Ni/YSZ cermet anode is only slightly less than the amount of carbon formed at OCV. These data are summarized in Figure IV.8, where the

asymptotic intensity limits of the 1560 cm^{-1} band scaled to intensities measured at OCV are plotted versus overpotential. These polarization and fuel-dependent differences observed in the Raman spectra support and provide additional insight into the thermal data reported in Figure IV.5: negative changes in temperature due to the introduction of fuel correlate directly with the relative amount of graphite being formed, and polarizing the cell leads to less graphite formation and correspondingly smaller temperature changes.

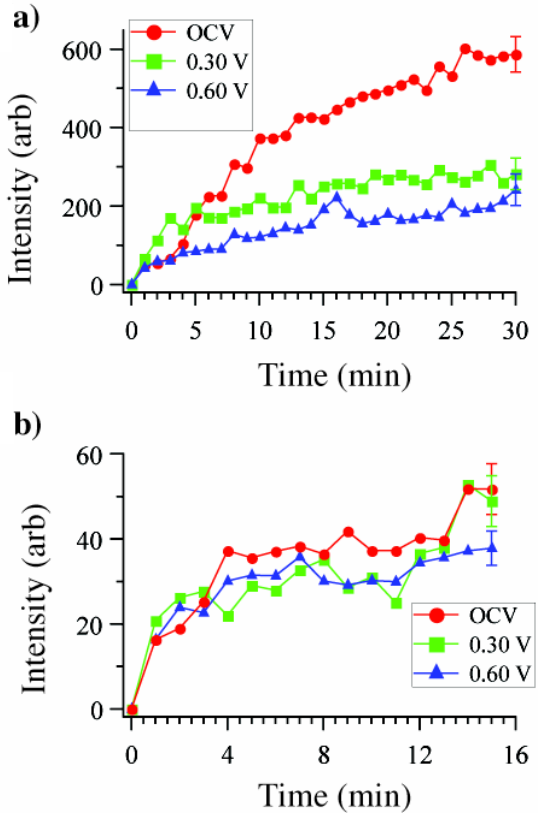

Figure IV.7. Kinetic data showing the growth of the graphite "G" band at ~ 1560 cm^{-1} for SOFC anodes exposed to CH_3OH (a) and CH_4 (b). The anodes are held at OCV (red) or polarized to overpotentials of 0.30 V (green) or 0.60 V (blue). Each point represents the peak intensity measured after a 60 sec. acquisition.

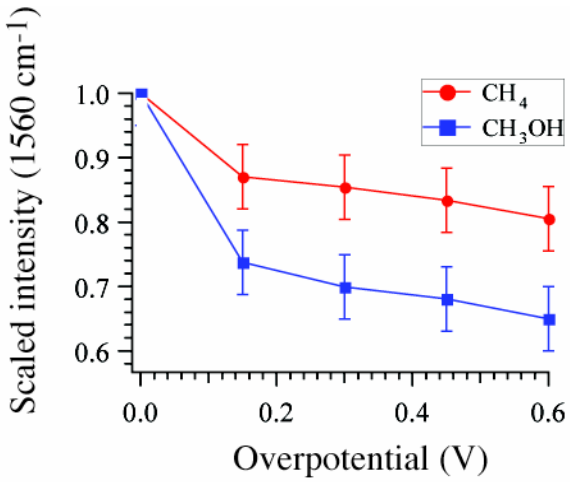

Figure IV.8. Scaled intensities of the graphite G band after the kinetic traces shown in Figure IV.7 have reached their asymptotic limits. Additional data not included in Figure IV.7 (0.15 and 0.45 V overpotentials) are included.

4. Discussion

4A. Complementary Thermal Imaging and Vibrational Raman Scattering Information

The *in situ* thermal imaging and vibrational studies of carbon growth on SOFC anodes are instructive and provide benchmark data that can be used to calibrate models of how SOFCs perform with different carbon containing fuels. Answering questions about the effects of carbon growth from these fuels requires knowing what is happening, and where, during operation. From the results described above, one can see that these two optical techniques provide detailed, complementary information about carbon deposition and the resulting consequences for SOFC operation. Raman spectroscopy is a species-specific, spatially localized measurement that identifies the relative amount and type of carbon present on the anode surface. While thermal imaging does not provide direct information about material composition, this technique does offer a component level view of the physical changes that occur due to the deposition process. For instance, anode cooling is observed from endothermic

fuel reactions on the anode, and the relative amount of carbon can be indirectly evaluated both from the temperature decrease observed across the anode and from the temperature rise that accompanies electrochemical oxidation of the deposited carbon after the fuel source has been turned off. The temperature of the anodes that had been exposed to CH_3OH rises approximately $\sim 2.0^{\circ}C$ under electrochemically oxidative conditions, while anodes exposed to CH_4 heat up by only $\sim 1.5^{\circ}C$. The larger temperature increase after CH_3OH is a direct indication that there is more carbon on the surface to be electrochemically oxidized. Data are shown in the Figure IV.6.

Thermal changes observed in the NIR imaging data can be used to determine the relative activity of endothermic reactions that involve carbon-containing species. These reactions include reforming and cracking and are responsible for anode coking. Our results show that CH_3OH and, to some extent, the reformate resulting from dry CH_3OH have a significant and systematic impact on the anode's condition. In contrast, CH_4 forms modest amounts of carbon, but conditions across the anode remain largely unchanged. These NIR imaging results provide direct, spatially resolved information regarding where activity is occurring on the anode surface. Furthermore, the relative changes in temperature suggest specific mechanisms responsible for changing anode conditions. For example, carbon formation from CH_3OH is likely the result of CH_3OH reforming on the anode. Had the CH_3OH fuel reformed entirely to H_2 and CO or if graphitic species had formed in the gas phase and simply deposited on the anode, the anode temperature would not have dropped as much as was observed in Figures IV.3e and 5.

The NIR imaging data provide a global, component level picture of how the physical properties across anodes change as a function of exposure to CH_3OH and CH_4. Raman spectra identify materials-specific information and can differentiate between mechanisms responsible for carbon formed from CH_3OH and CH_4. CH_3OH forms much more carbon under the conditions tested. Quantifying the amount of carbon deposited from the two fuels is difficult with Raman spectroscopy, but repeated experiments show that the terminal intensity of the "G" band from CH_3OH-formed graphite is always ~ 5-6 times greater than the "G" band from CH_4-formed graphite.

Finally, as noted in the previous section, the rate at which graphite grows on the anode held at OCV is identical for both CH_4 and CH_3OH for the first ~ 5 min. of exposure. However, just as intensity in the graphite vibrational spectrum from methane levels off, a new pathway for graphite formation becomes accessible to CH_3OH. This new carbon growth coincides approximately with the first evidence of disordered carbon (assigned to the 1360 cm^{-1} feature). A final observation from the graphite-growth kinetics from a CH_3OH feed is that this second mechanism for carbon deposition does not appear in data from polarized cells using CH_3OH. Data in Figure IV.7 from SOFCs held at 0.30 and 0.60 V show that the amount of graphite formed approaches an asymptotic limit without any evidence of two-stage carbon deposition.

4B. Determining Fuel Utilization and Carbon Deposition Mechanisms

Previous studies, both experimental and theoretical, have suggested that CH_3OH reforms extensively at SOFC operating temperatures. Cimenti and Hill have

published thorough thermodynamic analyses predicting that at typical SOFC temperatures CH_3OH quantitatively decomposes to CO and H_2 and other minor species including CH_4, CO_2, H_2O, and graphite.[38] However, Cimenti and Hill also recently published experimental results indicating that a CH_3OH feed passing through a furnace at 700˚C remains more than 20 % CH_3OH.[32] In the Raman accessible SOFC assembly, the fuel feed spends 0.03 sec. above 900˚C and 0.20 sec. total in the furnace prior to reaching the anode.[10] Gas-phase Fourier-transform IR studies of the anode side flow through our furnace have been used to determine that nearly 80 % of the CH_3OH in the initial fuel feed reaches anodes in our assemblies intact. Gas flows in the thermal imaging system remain at temperatures lower than ~ 715˚C, in a regime that is less likely to promote CH_3OH reforming.

Vibrational Raman spectra provide direct support for proposed mechanisms of CH_3OH and CH_4 activity in SOFCs that reflect Ni's catalytic activity and propensity for breaking C-H bonds.[23,31,32,35-37,45] These mechanisms do not require the presence of any gas-phase graphitic precursors because nearly 100 % of CH_4 fuel reaches the anode intact[10] as does most of the CH_3OH. The difference in the amount and type of carbon formed with the two fuels results from CH_3OH having lower bond enthalpies than CH_4 on Ni.[33] Given the relatively low current densities of our devices and the high mobility of H atoms adsorbed to Ni surfaces, one might reasonably assume that as C-H bond cleavage occurs adsorbed atomic hydrogen quickly diffuses to the electrochemically active region. The carbon is less mobile and remains behind on the surface and begins to form graphite. Due to the lower activity of CH_4, the carbon accumulates slowly and forms highly ordered graphite; CH_3OH's chemistry is more

involved, due in part to the weaker C-O bond that is more easily cleaved and also due to the additional (minor) gas-phase components present due to reforming and catalytic processes. The most important of these species is CO that can form graphite through the well established Boudouard mechanisms.[23]

The kinetically resolved spectroscopic data imply that graphite begins to grow on Ni anodes via a single, well-defined mechanism during the first few minutes of exposure to both CH_4 and CH_3OH, and this graphite is highly ordered. The more reactive fuel mix, however, induces a second mechanism for graphite growth that becomes apparent during longer exposures. Given the correlation between the onset of this second mechanism for graphite growth and the appearance of the "D" band in the *in situ* Raman spectra, we propose that the additional graphite that forms does so at grain boundaries and other defect sites on an existing, ordered graphitic substrate. We note that polarizing the SOFC diminishes the role of this second carbon formation mechanism, supporting previous observations that disordered graphite is more susceptible to electrochemical oxidation than highly ordered graphite.[27] These *in situ*, real-time data provide insight and direct confirmation that significant amounts of carbon form in SOFCs operating with CH_3OH at 700˚C, especially under low fuel utilization conditions.[33,38,46]

Figures IV.5 and IV.7 show that polarizing the cells decreases the amount of carbon deposition for both fuels, although the effect is much more significant for CH_3OH than for CH_4. This result is attributed to the exothermic oxidation of fuels and surface species. The persistence of significant intensity in the vibrational spectra and the fact that exposure to both fuels still leads to anode cooling at relatively high

overpotentials confirm that carbon deposition never ceases under conditions tested in these studies. We acknowledge that cells used in this work have relatively low power densities, and the anode side is exposed to fuel-rich conditions. As such, the cells likely do not operate under the carbon-free set of conditions proposed by Cimenti and Hill.[38]

5. Conclusions

The combination of NIR thermal imaging and vibrational Raman spectroscopy has been used to measure *in situ* and in real time the growth of carbon deposits on SOFC Ni/YSZ anodes at 715˚C operating with direct CH_4 and CH_3OH fuel feeds. While carbon deposition from these C_1 fuels is not as detrimental to the anode as other, higher-weight fuels studied previously,[10,31,47,48] the deposits do lead to decreased performance as determined from electrochemical experiments. The effects of carbon deposits on electrochemical oxidation are much more pronounced for CH_3OH than for CH_4. Independent, *ex situ* IR absorbance measurements show that given the conditions used in these studies methanol does not undergo extensive reforming on transit to the anode. This result implies that devices intended to operate with CH_3OH should employ steps to ensure that the fuel has undergone sufficient preprocessing to inhibit carbon growth. Such steps can include steam reforming,[35,39,49] CO_2 reforming,[50] and, in the case of methanol, operating at higher temperatures.[38,46]

The two optical techniques used together construct a more complete picture of the chemistry occurring on SOFC anodes than either method can on its own. NIR thermal imaging data show in real time how and where conditions across the anode

change as a function of fuel composition and operating overpotential. Specifically, the introduction of carbon containing fuels at OCV leads to a cooling of the anode surface, and this effect is much more pronounced for methanol ($\Delta T = -5.5^{\circ}C$) compared to methane ($\Delta T = -0.5^{\circ}C$). Polarizing the cell mitigates this phenomenon, but the effects are small. The reduction in temperature is assigned to endothermic reactions such as C-H and C-O bond cleavage occurring on the anode surface leading to carbon deposition. *In situ* Raman data identify the carbon deposits as graphitic with deposits formed from CH_4 being highly ordered and those formed from CH_3OH having a small degree of disorder. The Raman data can be analyzed further to quantify the growth kinetics of these carbon deposits. At early times, the carbon formed from CH_4 and CH_3OH grows at identical rates. Net graphite formation from CH_4 is self-terminating given that the Raman spectral intensity stops growing after ~ 5 min. Graphite formed from CH_3OH, however, appears to form from multiple pathways given the rapid onset of additional intensity in the Raman spectra acquired after ~ 5-7 min. This result is interpreted in terms of the relatively greater reactivity of the CH_3OH-based fuel mixture as well as the weaker bond enthalpies in CH_3OH. Both effects, gas-phase fuel composition and weaker bonds, can lead to more complex and varied surface chemistry.

Unlike traditional electrochemical measurements or *ex situ* analyses, the optical methods employed in this work provide real time, materials-specific *in situ* information about the chemistry occurring in operating SOFCs. Such data provide the quantitative benchmarks needed to test proposed models of electrochemical oxidation in these devices. More importantly, being able to differentiate mechanisms

of SOFC operation as a function of fuel identity and cell polarization can help guide the development of new SOFC materials and architectures.

6. References

(1) Brett, L.; Atkinson, A.; Brandon, N.; Skinner, J. *Chem. Soc. Rev.*, **2008**, *37*, 1568.

(2) Kendall, K. *Int. Mater. Rev.*, **2005**, *50*, 257.

(3) Mogensen, M.; Kammer, K. *Annual Rev. Mater. Res.*, **2003**, *33*, 321.

(4) Gorte, R.; Park, S.; Vohs, J.; Wang, C. *Adv. Mater.*, **2000**, *12*, 1465.

(5) Gorte, R.; Kim, H.; Vohs, J. *J. Power Sources*, **2002**, *106*, 10.

(6) Kee, R.; Zhu, H.; Goodwin, D. *Proc. Combust. Inst.*, **2005**, *30*, 2379.

(7) Liu, J. *Prog. Chem.*, **2006**, 18, 1026.

(8) McIntosh, S.; He, H.; Lee, S.; Costa-Nunes, O.; Krishnan, V.; Vohs, J.; Gorte, R. *J. Electrochem. Soc.*, **2004**, *151*, A604.

(9) McIntosh, S.; Vohs, J.; Gorte, R. *J. Electrochem. Soc.*, **2003**, *150*, A470.

(10) Pomfret, M.; Marda, J.; Jackson, G.; Eichhorn, B.; Dean, A.; Walker, R. *J. Phys. Chem. C*, **2008**, *112*, 5232.

(11) Randolph, K.; Dean, A. *Phys. Chem. Chem. Phys.*, **2007**, *9*, 4245.

(12) Jiang, S.; Chan, S. *J. Mater. Sci.*, **2004**, *39*, 4405.

(13) Ormerod, R. *Chem. Soc. Rev.*, **2003**, *32*, 17.

(14) Zhu, W.; Deevi, S. *Mater. Sci. Eng. A*, **2003**, *362*, 228.

(15) Kakac, S.; Pramuanjaroenkij, A.; Zhou, X. *Int. J. Hydrogen Energy*, **2007**, *32*, 761.

(16) Zhu, H.; Kee, R. *J. Electrochem. Soc.*, **2006**, *153*, A1765.

(17) Macek, J.; Novosel, B.; Marinnsek, M. *J. Eur. Ceram. Soc.*, **2007**, *27*, 487.

(18) Norinaga, K.; Deutschmann, O. *Ind. Eng. Chem. Res.*, **2007**, *46*, 3547.

(19) Sun, C.; Stimming, U. *J. Power Sources*, **2007**, *171*, 247.

(20) Pomfret, M.; Steinhurst, D.; Kidwell, D.; Owrutsky, J. *J. Power Sources*, **2010**, *195*, 257.

(21) Coutelieris, F.; Douvartzides, S.; Tsiakaras, P. *J. Power Sources*, **2003**, *123*, 200.

(22) Dokmaingam, P.; Assabumrungrat, S.; Soottitantawat, A.; Laosiripojana, N. *J. Power Sources*, **2010**, *195*, 69.

(23) Nikooyeh, K.; Jeje, A.; Hill, J. *J. Power Sources*, **2007**, *171*, 601.

(24) Rakass, S.; Oudghiri-Hassani, H.; Rowntree, P.; Abatzoglou, N. *J. Power Sources*, **2006**, *158*, 485.

(25) Suwanwarangkul, R.; Croiset, E.; Entchev, E.; Charojrochkul, S.; Pritzker, M.; Fowler, M.; Douglas, P.; Chewathanakup, S.; Mahaudom, H. *J. Power Sources*, **2006**, *161*, 308.

(26) Walters, K.; Dean, A.; Zhu, H.; Kee, R. *J. Power Sources*, **2003**, *123*, 182.

(27) Pomfret, M.; Owrutsky, J.; Walker, R. *Anal. Chem.*, **2007**, *79*, 2367.

(28) Pomfret, M.; Demircan, O.; Sukeshini, A.; Walker, R. *Environ. Sci. Technol.*, **2006**, *40*, 5574.

(29) Gupta, G.; Hecht, E.; Zhu, H.; Dean, A.; Kee, R. *J. Power Sources*, **2006**, *156*, 434.

(30) Assabumrungrat, S.; Sangtongkitcharoen, W.; Laosiripojana, N.; Arpornwichanop, A.; Charojrochkul, S.; Praserthdam, P. *J. Power Sources*, **2005**, *148*, 18.

(31) Cimenti, M.; Hill, J. *J. Power Sources*, **2010**, *195*, 3996.

(32) Cimenti, M.; Hill, J. *J. Power Sources*, **2010**, *195*, 54.

(33) Liu, M.; Peng, R.; Dong, D.; Gao, J.; Liu, X.; Meng, G. *J. Power Sources*, **2008**, *185*, 188.

(34) Kim, T.; Ahn, K.; Vohs, J.; Gorte, R. *J. Power Sources*, **2007**, *164*, 42.

(35) Laosiripojana, N.; Assabumrungrat, S. *J. Power Sources*, **2007**, *163*, 943.

(36) Jiang, Y.; Virkar, A. *J. Electrochem. Soc*., **2001**, *148*, A706.

(37) Mat, M.; Liu, X.; Zhu, Z.; Zhu, B. *Int. J. Hydrogen Energy*, **2007**, *32*, 796.

(38) Cimenti, M.; Hill, J. *J. Power Sources*, **2009**, *186*, 377.

(39) Sasaki, K.; Watanabe, K.; Teraoka, Y. *J. Electrochem. Soc.*, **2004**, *151*, A965.

(40) Cimenti, M.; Hill, J. *Energies*, **2009**, *2*, 377.

(41) Pomfret, M.; Owrutsky, J.; Walker, R. *J. Phys. Chem. B*, **2006**, *110*, 17305.

(42) Pomfret, M.; Steinhurst, D.; Kidwell, D.; Owrutsky, *J. Electrochem. Soc. Trans.*, **2009**, *25*, 839.

(43) Hofmann, P.; Panopoulos, K. *J. Power Sources*, **2010**, *195*, 5320.

(44) Laurencin, J.; Delette, G.; Sicardy, O.; Rosini, S.; Lefebvre-Joud, F. *J. Power Sources*, **2010**, *195*, 2747.

(45) Cimenti, M.; Alzate-Restrepo, V.; Hill, J. *J. Power Sources*, **2010**, *195*, 4002.

(46) Saunders, G.; Preece, J.; Kendall, K. *J. Power Sources*, **2004**, *131*, 23.

(47) Gupta, G.; Dean, A.; Ahn, K.; Gorte, R. *J. Power Sources*, **2006**, *158*, 497.

(48) McIntosh, S.; Gorte, R. *J. Chem. Rev.*, **2004**, *104*, 4845.

(49) Cocco, D.; Tola, V. *J. Eng. Gas Turbines Power*, **2007**, *129*, 478.

(50) Pillai, M.; Lin, Y.; Zhu, H.; Kee, R.; Barnett, S. *J. Power Sources*, **2010**, *195*, 271.

Chapter 5: *In Situ* Raman and Electrochemical Impedance Investigations of the Oxidative and Steam Reforming of Methane in Solid Oxide Fuel Cells

1. Introduction

Fuels cells have attracted considerable attention because of their ability to provide electricity cleanly and efficiently.[1-3] Since fuel cells convert fuel directly into electrical energy, fuel cell efficiencies can be as high as 80 % with minimal NO_x and SO_x pollutants produced.[2] Of the various types of fuel cells, solid oxide fuel cells (SOFCs) stand out for their versatility and ability to use a wide variety of fuels including H_2, CO, alcohols, and even medium-sized hydrocarbons.[2,4-15] Fuel flexibility and high tolerance to contaminants afford SOFCs distinct advantages over other devices such as polymer electrolyte membrane fuel cells (PEMFCs) and direct methanol fuel cells (DMFCs), where trace amounts of species such as CO can deactivate catalytic sites leading to eventual device failure.[1,11,16] An additional benefit of SOFCs is that they can be manufactured from relatively inexpensive materials and can be easily integrated into stacked systems for commercial application.[2,13,17-25]

While the overall description of SOFC operation is straight forward, the detailed mechanisms associated with processes occurring at the SOFC anode and cathode can be more tenuous.[1-3,26-33] The high activation energies associated with oxide diffusion through the electrolyte (100 kJ/mol)[34] and molecular oxygen activation at the cathode (223 kJ/mol)[35] require that these device run at elevated

temperatures (≥ 650˚C). These extreme environments also pose significant experimental challenges that limit the methods that can be used to study SOFC chemistry *in situ* and in real time. Experiments described in this work couple newly developed, *in situ* vibrational Raman spectroscopy with electrochemical impedance spectroscopy (EIS) to study the chemistry of reformed fuel mixtures on Ni-YSZ cermet anodes of electrolyte-supported SOFCs operating at 715˚C. Findings from these *in situ* measurements provide insight into mechanisms responsible for SOFC operation *and* component degradation.

Of the different carbon containing fuels that have been used in SOFCs, methane (CH_4) is one of the most common.[36-41] CH_4 is an abundant natural resource and, more importantly, CH_4 can be considered a renewable fuel when derived from biomass.[36-41] However the average C-H bond enthalpy in CH_4 is 416 kJ/mol meaning that methane is relatively inert at temperatures commonly encountered in SOFCs (700-1000˚C).[42] Consequently, SOFC anodes typically consist of electrocatalytic, conducting materials (such as Ni) and CH_4 is often "pre-treated" and partially oxidized before reaching the membrane electrode assembly (MEA).[36,38] Recent reports have found that at temperatures typically encountered in SOFCs, on average only ~ 25-50 % of the incident methane reacts, and the majority of the fuel leaves the system in the exhaust.[3,43] Catalysts lower the barrier to electrochemical methane oxidation but this process also runs the risk of driving carbon formation on the SOFC anode (Eq. 1).[2,13,17-22] Carbon formation on SOFC anodes represents a primary mechanism responsible for SOFC degradation by decreasing porosity, increasing tortuosity, and blocking active Ni catalysts.[1,9,10,13,22,44-51] Recent reports have also

suggested this low percentage of CH_4 conversion can be increased to as high as ~ 70-90 % in the presence of a reformer introduced into the CH_4 fuel feed.[2,36,39,43,46,48,52-54] Reforming is often employed to create a favorable fuel mixture of CO and H_2 that can be oxidized more readily at the anode.[2,36,37,39,43,46,48,52-54]

$$CH_{4(g)} \rightarrow C_{(ads)} + 4H_{(ads)} \quad \textbf{(Eq. 1)}$$

Reforming can be accomplished in several different ways. One is to humidify the CH_4 with H_2O and another method is to add O_2 into the fuel feed. These processes are known as steam and oxidative reforming, respectively, and the reactions associated with these processes are shown in Eq. 2 and Eq 3.[2,36,37,39,43,46,48,52-54]

$$CH_{4(g)} + O_{2(g)} \rightarrow CO_{2(g)} + 2H_{2(g)} \quad \textbf{(Eq. 2)}$$

$$CH_{4(g)} + H_2O_{(g)} \rightarrow CO_{(g)} + 3H_{2(g)} \quad \textbf{(Eq. 3)}$$

Converting the methane into H_2 and CO prior to the fuel reaching the electrochemically active region can prevent a lowering of the open circuit voltage (OCV) brought about by overpotential losses associated with the energy needed for the activation of methane oxidation.[55] Preventing such losses can improve SOFC performance and fuel utilization.[55] These effects are more significant for oxidative reformed methane. An important point to note is that complete oxidation of methane to form CO_2 does not improve device efficiency because CO_2 can not be further oxidized electrochemically. By limiting the amount of O_2 introduced in the oxidative

reforming process, CO_2 formation can be limited and CO formation can be promoted (Eq. 4).[2,38,43,54] Similar effects can be observed when excess H_2O is added to the fuel feed again promoting CO_2 formation at the expense of CO (Eq. 5).[2,46,49] One must be cautious, however, when considering how much CO should be in a fuel feed, for while CO can be electrochemically oxidized to form CO_2 and electricity, CO can also be a source of carbon formation via the Boudouard process, Eq. 6.[48]

$$CH_{4(g)} + 1/2O_{2(g)} \rightarrow CO_{(g)} + 2H_{2(g)} \quad \textbf{(Eq. 4)}$$

$$CH_{4(g)} + 2H_2O_{(g)} \rightarrow CO_{2(g)} + 4H_{2(g)} \quad \textbf{(Eq. 5)}$$

$$2CO_{(ads)} \rightarrow C_{(ads)} + CO_{2(g)} \quad \textbf{(Eq. 6)}$$

Carbon formation can be prevented by either polarizing the cell to increase the oxide flux to the anode or by providing additional reformer to the incident fuel feed so that any graphite that does form can be subsequently oxidized.[55,56] The goal of the work described below is to identify directly *in situ* and in real time the changes occurring on SOFC anodes operating with direct methane, or methane that has undergone both oxidative and steam reforming. These studies use vibrational spectroscopy to monitor the appearance, growth and suppression of graphitic carbon on Ni/YSZ cermet anodes, and optical data are correlated with electrochemical measurements. Coupling these two methods –vibrational spectroscopy and electrochemical measurements– affords us the ability to monitor directly how device performance depends on molecular and material species present *in operando*.

2. Experimental

2A. SOFC Membrane Electrode Assembly

The electrolyte supported MEAs used in the experiment described in this paper are similar to those that have been used in previous studies.[11,27,56,57] These MEAs consisted of an yttria-stabilized zirconia (YSZ) electrolyte (Tosoh Corporation) with a Ni/YSZ cermet anode and a lanthanum strontium manganate (LSM)/YSZ cermet cathode (Fuel Cell Materials Inc.) that were constructed in-house. The YSZ powder use in construction of the electrolyte consisted of 8 % Y_2O_3 (by mole fraction of Y relative to Zr). A mass of 2.0 g of the YSZ powder was loaded into a 1.1 inch die and pressed at 20,000 psi for five minutes to produce an YSZ disc that was then sintered at 1500˚C for one hour in ambient air with a heat up and cool down rate of 1˚C/min. The resulting electrolyte disc had a diameter of 25 mm and a thickness of 0.80 ± 0.02 mm. A tape casting method was used to apply a 30 μm thick layer of the cathode paste, consisting of 50 % by weight of $(La_{0.8}Sr_{0.2})_{0.98}MnO_{3-x}$ to YSZ. The electrolyte and cathode were then sintered at 1150˚C for one hour in ambient air with a heat up and cool down rate of 1˚C/min. The same tape casting method was also used to apply a 30 μm thick layer of the anode paste, consisting of 50 % by weight of Ni to YSZ, to the newly sintered electrolyte with cathode. The electrolyte, cathode and anode were then sintered again at 1350˚C for three hours in ambient air with a heat up and cool down rate of 1˚C/min. Platinum paste (Heraeus) was used to attach platinum mesh (Alfa Aesar) and gold wire (Alfa Aesar) to the cathode as a current collector, while gold paste (Heraeus) was used to attach silver mesh (Alfa Aesar) and gold wire to the anode to act as the anode current collector.

2B. *In situ* Raman SOFC Assembly

Details regarding the construction of these devices have been described previously.[11,27,56,57] Alumina paste was used to attach the SOFC MEA atop a alumina tube that was encased inside a optically transparent quartz tube so that *in situ* Raman measurements could be performed on the anode surface. A network of alumina tubes were used to direct specific gas flows to the anode and cathode. This whole system is surrounded by a split tube furnace to maintain MEA surface temperatures of 715˚C while also allowing for optical viewing for the Raman spectrometer. The Raman assembly utilizes custom built microscope optics that was used both for excitation and collection of scattered radiation normal to the anode. In the Raman scattering experiments, 488 nm light (8mW) is focused onto the anode, and backscattered light is collected and sent to the charged couple device (CCD) detector (Renishaw, inVia). Even though a 15 mm long working distance objective is used, the objective itself sits close to the cell limiting MEA operational temperatures to < 730˚C. (The microscope objective heats up to ~ 180˚C). Temperatures are maintained by positioning the anode near the top of an open-ended tube furnace and heating the center of the furnace to 1000˚C. A consequence of this design is that the fuel being studied traverses a high-temperature region in the middle of the furnace and spends ~ 0.03 seconds at temperatures ≥ 900°C. At these temperatures significant reforming can occur, so *ex situ* FTIR spectroscopy was used to quantify the chemical composition of the gas mixture reaching the anode.

2C. Gas Flows

All gas flows on both sides of the MEA, with the exception of H_2O, were controlled by rotameters (Omega). An air (100 sccm) and argon (100 sccm) mixture was sent to the cathode. A variety of gas mixtures were used at the anode including CH_4, CH_4:H_2O, and CH_4:O_2. For oxidative reforming, a variety of CH_4:O_2 molar ratios were used. The CH_4:O_2 molar ratios used in these experiments were 2:1, 4:1, and 8:1. These CH_4:O_2 molar ratios are similar to those employed by Ishihara et. al.[43] where in their studies they used CH_4:O_2 molar ratios of 2:1 and 4:1. With every CH_4:O_2 molar ratio, CH_4 remained constant at 50 sccm to ensure the same carbon load for each fuel mixture. The flow rates that were used for O_2 were 25 sccm for 2:1, 12.5 sccm for 4:1, and 6.25 sccm for a 8:1 molar ratio, a balance of argon was adjusted accordingly. Experiments evaluating the effects that steam reforming on CH_4, routed the CH_4/Ar feed through an H_2O bubbler held at a temperature of 0˚C and 21˚C before entering into the SOFC. The temperature of the bubbler controlled the vapor pressure of H_2O. The H_2O vapor pressures of 5.9×10^{-3} atm at 0˚C produced a flow rate of 0.89 sccm and a CH_4:H_2O molar ratio of ~ 56:1 and 2.5×10^{-2} atm at 21˚C resulting in a H_2O flow rate of 3.8 sccm and molar ratio of ~ 13:1.

2D. Explanation of *Ex Situ* FTIR Measurements

The extent of reforming that occurs prior to a fuel reaching an SOFC anode will depend sensitively on the original gas mixture composition, flow rates and temperature. An important point to note is that the fuel mixtures that reach the anode very well may not have compositions predicted by thermodynamics. In order to interpret our *in situ* spectroscopic and electrochemical data, we carefully quantified

the gas phase composition of the reforming mixtures used with *ex situ* FTIR measurements. These exhaust measurement were characterized by using an FTIR (Jasco). The gas mixtures (at the same flow rates as explained in the gas flow section of this paper) were sent through a split tube furnace whose center was heated to 1000˚C in order to duplicate the flow path taken by the gas mixture to the anode in the *in situ* Raman SOFC assembly. The exiting gas mixture was collected in a 5 cm IR gas cell (Buck Scientific) and then measured in the FTIR spectrometer.

2E. Explanation of Electrochemical Measurements

All electrochemical measurements and overpotential conditioning experiments were performed using a Princeton Applied Research VMC-2 potentiostat/galvanostat/FRA. In a typical experiment, the SOFC was first tested, operating with H_2 (in Ar) as the fuel, using linear sweep voltammetry (LSV) and electrochemical impedance spectroscopy (EIS) measurements. Similar measurements were performed at various times during an experimental run and compared to initial benchmark results to assess device durability. To observe the changes in electrochemical performance when using the different fuel mixtures, EIS measurements were performed continuously and concurrently with *in situ* Raman spectroscopic measurements. The chemistry and performance of the SOFC were studied at different cell polarizations including open circuit voltage (OCV), 0.30 V and 0.60 V. During impedance measurements, the potentiostat polarized the SOFC to well-defined overpotentials with respect to OCV. Here, overpotential (V_{OP}) refers to the difference between OCV and the voltage across the operating cell ($V_{OP} = V_{CELL} - V_{OCV}$). Separate and independent LSV measurements were also taken

of the SOFC running on each fuel mixture, to understand effects that these fuel mixtures will have on overall cell voltage, current and power.

2F. Explanation of *In situ* Raman Measurements

In situ electrochemical measurements and *ex situ* analytical methods can provide valuable information about SOFC performance but since electrochemical measurements can only measure changes in performance and *ex situ* measurements are performed after the device has operated, they both can not provide a direct correlation between changes in electrochemical performance and specific chemical and material changes occurring in the SOFC. *In situ* Raman spectroscopy overcomes these limitations. In the experiments presented below, vibrational Raman spectra from SOFC anodes are acquired continuously and simultaneously with temporal resolution as short as ~ 5 sec. The Raman measurements were performed during exposure of the SOFC anode to direct CH_4, oxidative reformed CH_4, and steam reformed CH_4. Spectra show time dependent changes in anode composition, including the growth and oxidation of graphitic deposits and the oxidation of the Ni electrocatalyst.

3. Results and Discussion

3A. *Ex Situ* FTIR Exhaust Measurements

Methane reforming –both steam and oxidative– will form a mix of CO, H_2, CO_2, and H_2O.[2,36,37,39,48,53,54] The IR spectra of the various reformed gas mixtures are shown in Figure V.1. Also included, is the FTIR spectrum of direct methane passing through the furnace. The neat methane spectrum shows no sign of additional species,

confirming that CH_4 does not undergo gas phase pyrolysis under these conditions.[11,40,51,58]

Oxidative reforming of the CH_4 fuel resulted in the formation of CO (2140 cm^{-1}) and CO_2 (2330 cm^{-1}). The amount of each species was dependent on the original molar ratios of CH_4 and O_2. Changing the CH_4:O_2 molar ratios from 2:1 to 4:1 leads to little change in the relative amounts of CO_2 and CO being produced. This balance changes dramatically, however when the CH_4:O_2 ratio is raised to 8:1. Under these fuel-rich conditions, CO concentration rises 4-fold while CO_2 concentration falls by a factor of 6, Figure V.2a. At the two molar ratios tested for steam reforming, only CO was observed with the amount of CO increasing with the amount of H_2O vapor originally present in the fuel feed. This trend is shown in Figure V.2b. The extent of CH_4 reforming impacts electrochemical performance and the susceptibility of the Ni/YSZ anodes to carbon formation.

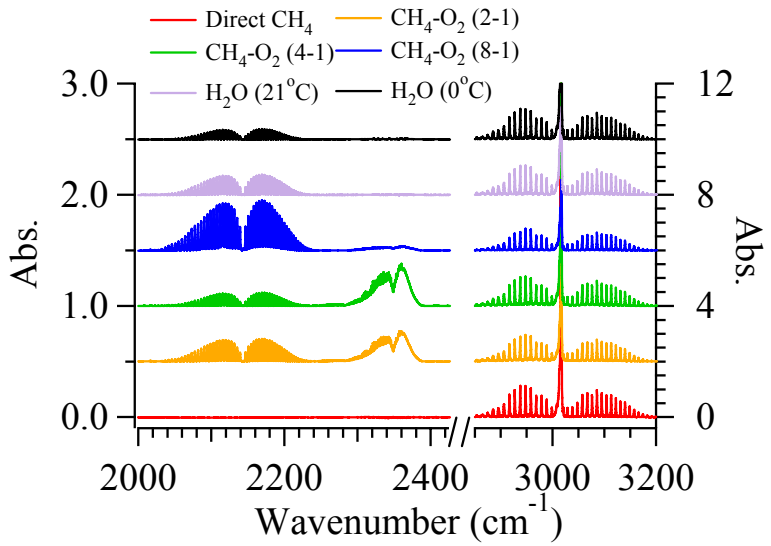

Figure V.1. Real time vibrational-rotational IR measurements. IR spectra displaying the CO, CO_2, and CH_4 regions taken with different fuel mixtures (spectra are offset for clarity).

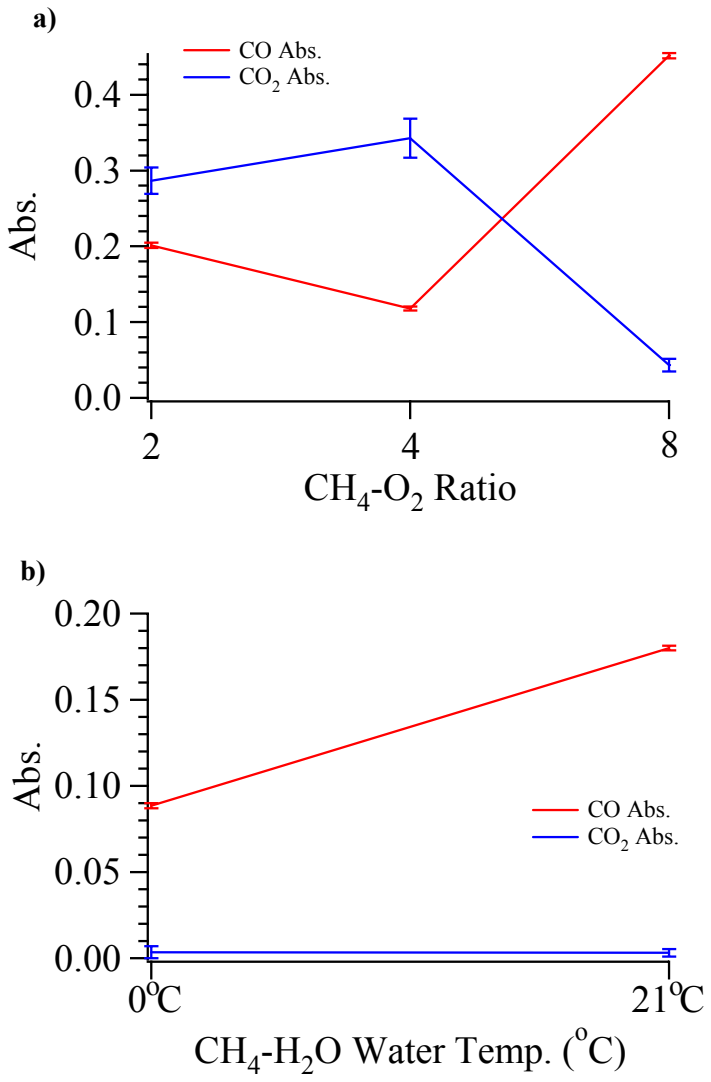

Figure V.2. a) Comparison of the R branch peak intensity for CO and CO_2 in the presence of varying ratios of CH_4:O_2. b) Comparison of R branch peak intensity for CO and CO_2 resulting from flowing CH_4 through a H_2O bubbler at 0˚C and 21˚C.

3B. Linear Sweep Voltammetry Measurements

In a typical V-I plot there are three distinct regions, each reflecting different aspects of the electrochemistry occurring in the SOFC.[55] These regions are associated with overpotentials required to overcome activation, ohmic, and concentration losses.[55] The region of interest most relevant to our studies is the low

current, low overpotential region of the V-I data as these conditions reflect the energy needed to drive electrochemical oxidation of CH_4 in the forward direction.[55] For a direct (dry) CH_4 fuel feed the measured OCV is relatively high at -1.30 ± 0.05 V. The OCV magnitude diminishes when O_2 and H_2O reformers are added into the CH_4 fuel. When using O_2 as a reformer, OCV was -0.94 V with a CH_4:O_2 molar ratio of 2:1. When the fuel mixture became more fuel rich With a CH_4:O_2 ratio of 8:1 the measured OCV was -1.09 V. Both of these trends are exhibited in Figure V.3. A similar trend was observed in Figure V.4, when H_2O was added into the fuel feed resulting in a measured OCV of -1.01 V for a CH_4:H_2O ratio of 13:1 and -1.07 V for a 56:1 ratio. These reductions in OCV for both oxidative and steam reforming conditions also resulted in lower activation energies needed to drive electrochemical oxidation.

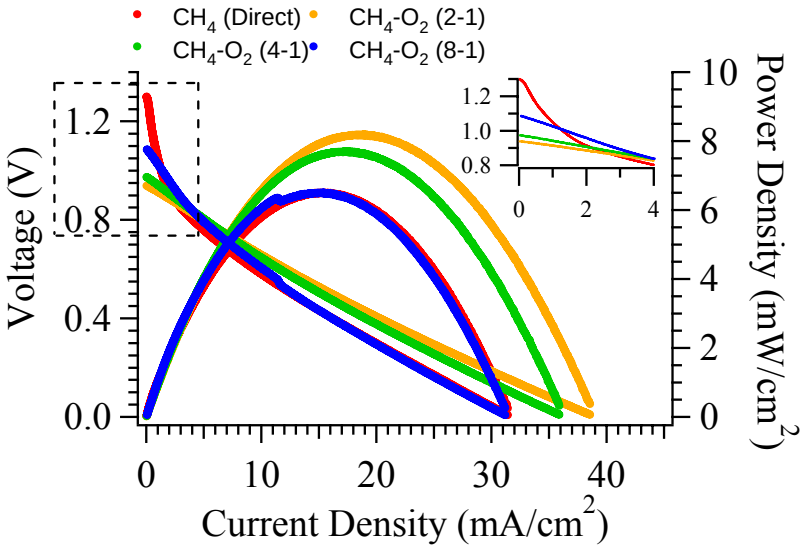

Figure V.3. Voltammetry data from different CH_4:O_2 fuel mixtures with direct CH_4 used as a reference. Inset in graph is a zoomed in region of the V-I curve associated with activation of the fuel mixtures.

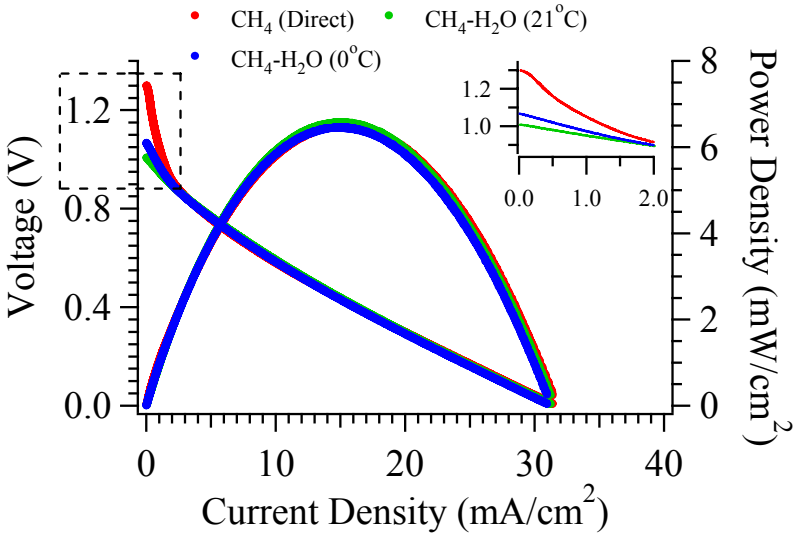

Figure V.4. Voltammetry data showing the differences in direct CH_4 when H_2O is added into the fuel at different H_2O bubbler temperatures. Inset in graph is a zoomed in region of the activation area of the V-I curve.

3C. Real Time Electrochemical Impedance Spectroscopy Measurements

Repeated EIS measurements were made to observe how electrochemical performance evolved with exposure to direct CH_4 and the reformate mixtures created by the oxidative and steam reforming of CH_4. These measurements were conducted with different cell polarizations. All values for R_{bulk} and R_{pol} are tabulated in Table V.1 and were determined from fitting the 180-360 sec. EIS data presented in Figure V.5 and Figure V.6 for the various fuel mixtures at OCV, 0.30 V and 0.60 V overpotentials. The model used consisted of an equivalent circuit having a resistor (R_{bulk}), and three consecutive RC circuit elements (R_1/C_1 , R_2/C_2, R_3/C_3) in series.[23,55] R_{pol} is the sum of all three resistive elements in the RC circuit elements ($R_{pol} = R_1 + R_2 + R_3$).

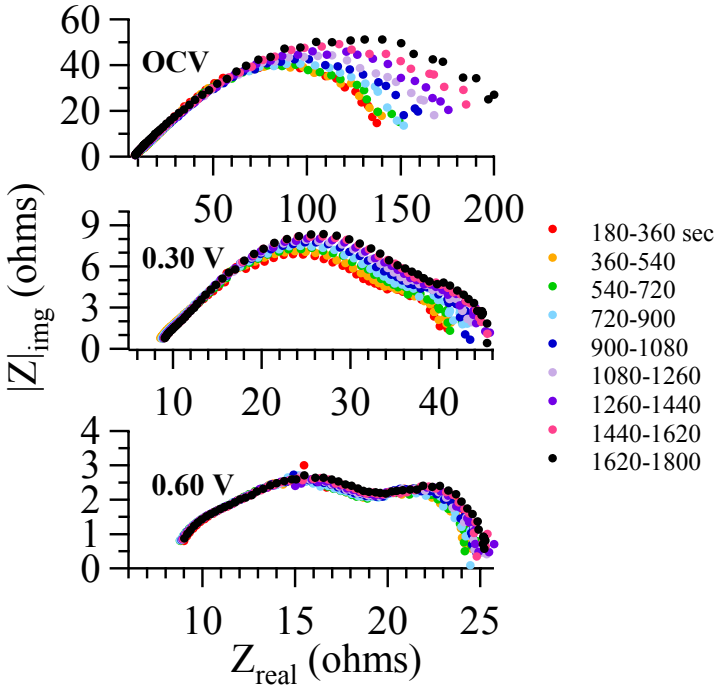

Figure V.5. Electrochemical impedance data from direct CH_4 operating at various cell overpotentials. The frequency of the impedance wave varied between 100 kHz (at low impedance) and 32 mHz (at high impedance). Peak frequencies: ~ 320 Hz (high frequency arc), ~ 6.3 Hz (middle frequency arc), and ~ 320 mHz (low frequency arc)

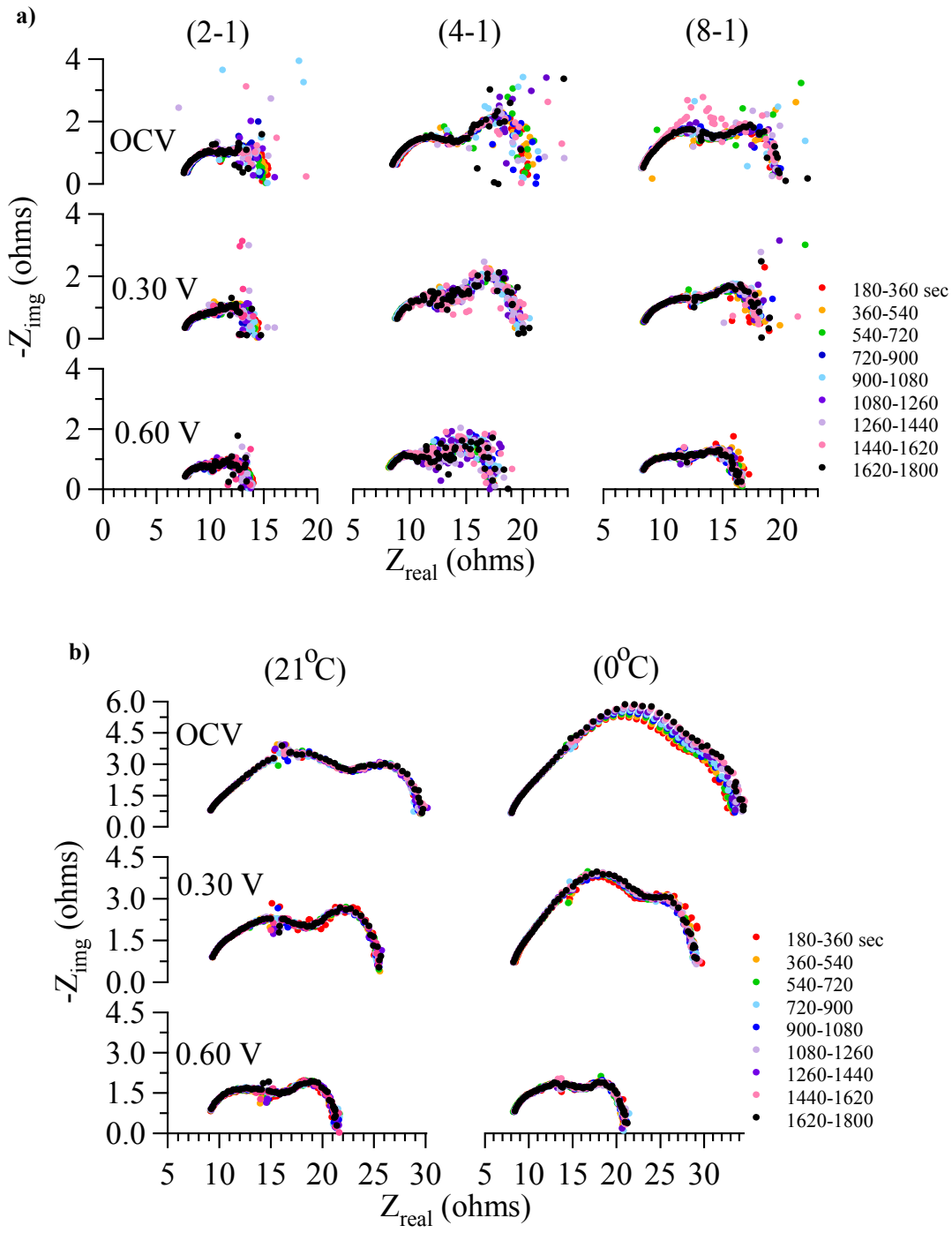

Figure V.6. Electrochemical impedance data from various fuel mixtures taken at OCV, 0.30 V, and 0.60 V overpotentials. a) CH_4 with varying amounts of O_2, b) CH_4 humidified with H_2O from a bubbler at 0˚C and 21˚C. The frequency of the impedance wave varied between 10 kHz (at low impedance) and 32 mHz (at high impedance). Peak frequencies for CH_4:O_2 (2:1): ~ 1000 Hz (high frequency arc), ~ 40 Hz (middle frequency arc), and ~ 790 mHz (low frequency arc). Peak frequencies for CH_4:O_2 (4:1): ~ 160 Hz (high frequency arc), ~ 13 Hz (middle

frequency arc), and ~ 400 mHz (low frequency arc). Peak frequencies for CH_4:O_2 (8:1): ~ 63 Hz (high frequency arc), ~ 5.0 Hz (middle frequency arc), and ~ 250 mHz (low frequency arc). Peak frequencies for CH_4:H_2O (21˚C): ~ 501 Hz (high frequency arc), ~ 40 Hz (middle frequency arc), and ~ 320 mHz (low frequency arc). Peak frequencies for CH_4:H_2O (0˚C): ~ 320 Hz (high frequency arc), ~ 6.3 Hz (middle frequency arc), and ~ 320 mHz (low frequency arc)

	R_{bulk} (Ω)	R_1 (Ω)	R_2 (Ω)	R_3 (Ω)	R_{pol} (Ω)
CH_4-O_2 (2-1) OCV	**8.1 ± 0.1**	**2.1 ± 0.1**	**2.1 ± 0.1**	**2.8 ± 0.1**	**7.0**
0.30 V	8.1 ± 0.1	1.7 ± 0.1	2.0 ± 0.1	2.4 ± 0.1	6.1
0.60 V	8.0 ± 0.1	1.6 ± 0.1	1.8 ± 0.1	2.3 ± 0.1	5.7
CH_4-O_2 (4-1) OCV	**9.1 ± 0.1**	**2.8 ± 0.2**	**3.1 ± 0.2**	**5.1 ± 0.2**	**11.0**
0.30 V	9.0 ± 0.1	2.8 ± 0.1	2.8 ± 0.2	4.8 ± 0.2	10.4
0.60 V	8.3 ± 0.1	2.6 ± 0.1	2.5 ± 0.1	3.6 ± 0.2	8.7
CH_4-O_2 (8-1) OCV	**8.6 ± 0.1**	**2.9 ± 0.1**	**3.3 ± 0.1**	**4.7 ± 0.1**	**10.9**
0.30 V	8.6 ± 0.1	2.3 ± 0.2	2.8 ± 0.2	3.9 ± 0.3	9.0
0.60 V	8.4 ± 0.1	2.2 ± 0.1	2.4 ± 0.2	3.3 ± 0.2	7.9
CH_4-H_2O (21˚C) OCV	**9.6 ± 0.1**	**3.9 ± 0.2**	**8.0 ± 0.3**	**7.3 ± 0.4**	**19.2**
0.30 V	9.6 ± 0.1	3.6 ± 0.2	5.4 ± 0.2	6.4 ± 0.3	15.4
0.60 V	9.3 ± 0.1	3.2 ± 0.2	3.5 ± 0.2	4.8 ± 0.2	11.5
CH_4-H_2O (0˚C) OCV	**8.4 ± 0.1**	**4.5 ± 0.3**	**10.1 ± 0.5**	**8.8 ± 0.6**	**23.4**
0.30 V	8.9 ± 0.1	4.3 ± 0.2	8.3 ± 0.3	7.4 ± 0.4	20.0
0.60 V	8.4 ± 0.1	3.1 ± 0.2	4.1 ± 0.2	4.8 ± 0.2	12.0
CH_4 (Direct) OCV	**9.3 ± 0.2**	**6.9 ± 0.5**	**22.9 ± 1.8**	**90.5 ± 3.3**	**120.3**
0.30 V	9.2 ± 0.2	5.1 ± 0.3	14.2 ± 0.6	10.9 ± 0.8	30.2
0.60 V	9.2 ± 0.1	3.6 ± 0.2	5.6 ± 0.3	5.8 ± 0.2	15.0

Table V.1. Impedance values modeled from data presented in Figure V.5 and Figure V.6. Highlighted values are from the OCV cases of each fuel mixture.

EIS is a valuable technique when observing changes in overall electrochemical performance of SOFCs because the technique not only highlights changes in impedance but also can provide detailed information about specific mechanisms assigned to frequency dependent SOFC processes.[23,55] Information about SOFC processes can be inferred from the different arcs (R_1, R_2, and R_3) and the purely ohmic bulk resistance (R_{bulk}) exhibited in a typical EIS spectrum.[23,55] R_{bulk} is the frequency independent x-intercept at low resistances and is associated with the

temperature dependent, ohmic process of oxide transfer through the electrolyte.[23,55] For an electrolyte-supported SOFC, there are three different arcs associated typically with cathodic processes, and anodic processes.[23,55] From numerous experiments, we infer that the highest frequency arc, at low Z_{real} impedances, is associated with cathodic processes and remains unchanged from prolonged exposures to carbon containing fuels. Also from these experiments we observe that with the formation of graphite from prolonged exposures to these same fuels there is an increase in both impedance components in the middle and high frequency arcs inferring that these arcs are associated with anodic processes.

When observing the EIS measurements taken during the continuous exposure to direct CH_4, several interesting observations arise (Figure V.5). The first observation is that R_{pol} is significantly greater at OCV (120.2 Ω) when compared to polarized cells, 30.2 Ω (0.30 V) and 15.0 Ω (0.60 V). The value for R_{pol} decreases significantly when non-equilibrium conditions are imposed by increasing cell polarization, diminishing the need for CH_4 oxidation activation. The final observation to be made from Figure V.5 is that R_{pol} increases with prolonged exposure of the MEA to the direct CH_4 feed at each overpotential, signifying degradation in the electrochemical performance. The largest changes in the impedance occur in the second and third EIS arcs, and these are the arcs generally assigned to anode processes. An increase in these arcs suggests that with prolonged exposure to methane, anodic deposits of graphite reduce the anode's overall electrocatalytic ability.[56] This increase in R_{pol} that occurs with prolonged exposures to CH_4 is lessened as cell overpotential is increased. Polarizing the cell increases the

oxide flux to the anode and promotes electrochemical oxidation thereby inhibiting the formation of carbon deposits and other unwanted species that can degrade electrochemical performance.[55,56]

The same EIS measurements were also performed during prolonged exposures of the oxidative and steam reformed mixtures (Figure V.6a and Figure V.6b, respectively). The findings from these measurements differ noticeably from observations made with direct CH_4. The first observation from EIS data from the reformed mixtures is that they have significantly smaller values of R_{pol} at OCV, with an average of 9.6 Ω and 21.3 Ω for oxidative reformed and steam reformed mixtures, respectively. In addition, the change in R_{pol} at higher overpotentials was much smaller compared to data from the direct CH_4 feed.

An interesting finding in the EIS measurements made with the oxidative reformed CH_4 was an increase in the degree of scattering in the arcs acquired at lower frequencies. Similar scatter *was not* observed in EIS data acquired from the SOFCs operating with direct CH_4 or steam reformed CH_4. For each molar ratio of CH_4:O_2 at early times the EIS spectra exhibited well defined EIS arcs, but as the exposure to O_2 persisted these arcs became much noisier. The variability observed in these EIS measurements could arise from fluctuations in fuel utilization and/or continuous oxidation and reduction of Ni particles throughout the anode.[55,59] R_{pol} shows no visible signs of increase with prolonged exposures at all molar ratios of CH_4:O_2 implying that any scatter should be associated with reversible chemistry occurring at the SOFC anode. Similarly, for the reformate formed by the 13:1 ratio of CH_4: H_2O, R_{pol} remained constant as a function of exposure time. The same can not be said for

the molar ratio of 56:1 CH_4:H_2O (0˚C) where a modest but systematic increase in R_{pol} with prolonged exposure of the fuel can be observed both at OCV and at V_{OP} = 0.30 V once again indicating that unwanted changes are occurring at the SOFC anode.[56]

3D. *In Situ* Raman Spectroscopy Measurements

In situ Raman measurements were conducted concurrently with EIS measurements. Raman spectra acquired from the SOFC anode operating with direct CH_4 at OCV, 0.30 V, and 0.60 V are shown in Figure V.7a. Each spectrum represents a ~ 30 sec. acquisition, and for clarity only three spectra taken at different exposures times (0, 89, 1753 sec.) are shown for each cell polarization. Several observations stand out. The first observation is the appearance of a strong, sharp feature at ~ 1560 cm^{-1} in selected spectra. This feature is referred to as the "G" band of graphite and is characteristic of a highly ordered, sp^2 hybridized carbon network with minimal defects and/or grain boundaries.[11,27,57] This observation correlates the formation of graphite on the anode surface with the ~ 45 % increase in R_{pol} with 30 min. of exposure to direct CH_4 at OCV observed in Figure V.5. A second observation is that polarizing the cell reduces the amount of graphite formed, and this result coincides with a minimal increase in R_{pol} of ~ 13 % for 0.30 V and ~ 4 % for 0.60 V resulting from prolonged exposures (30 min.) of the MEA to the direct CH_4 feed also presented in Figure V.5. We believe that the higher overpotentials promote carbon oxidation and limit graphite accumulation at the anode.[56] The third observation is that the kinetics of graphite formation depends on cell overpotential. Rapid graphite growth is observed for SOFCs at OCV and 0.30 V, but when the cell

is polarized to 0.60 V, graphite formation is minimized with very little graphite appearing at 89 sec. and the total graphite seen at 1753 sec. is measurably less than what was observed at lower overpotentials. The growth kinetics of graphite is shown in more detail in Figure V.7b where the peak height of the graphite "G" band is plotted with respect to time. The data are fitted to a simple first order growth model.[56] In the kinetic data we observe two distinct regions: at earlier times (< 100 sec.) the spectra show slower growth that is followed by a second region at later times exhibiting faster graphite growth. This pattern is observed for both OCV and 0.30 V_{OP} conditions. At 0.60 V overpotential graphite growth is slowed and the maximum graphite growth extends ~ twice as long before reaching an asymptotic limit.

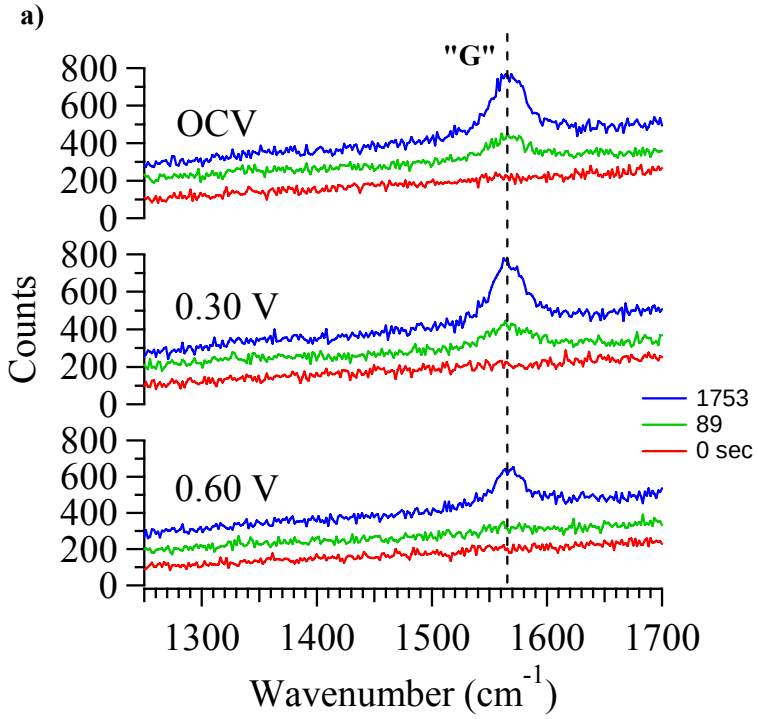

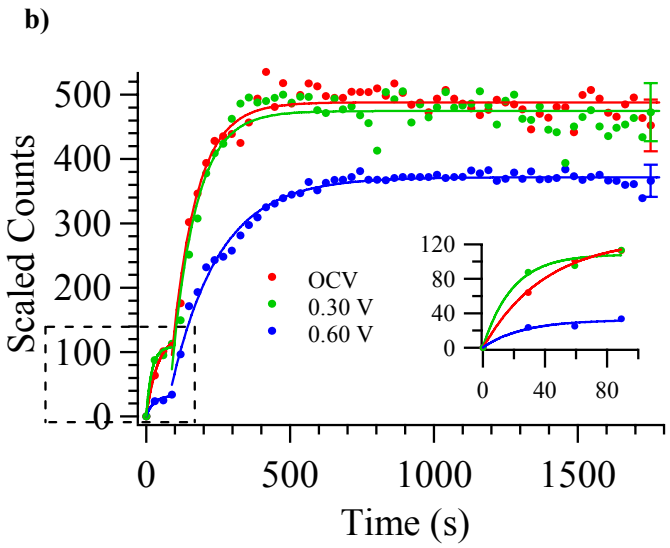

Figure V.7. *In situ* Raman measurements taken at 715˚C under various overpotential conditions with direct CH_4. a) Showing graphite growth as a function of CH_4 exposure and polarization. Each spectrum represents a 30 sec. acquisition. For clarity the 0, 89 and 1753 sec. are chosen for each overpotential case and the 89 and 1753 sec. spectra are offset for clarity. b) *In situ* Raman analysis of the general kinetics of graphite growth induced by the direct CH_4 fuel feed. Data shown plots the intensity of the graphite "G" band at 1560 cm^{-1} with respect to exposure time of CH_4 at various overpotentials. Data are fit to a simple first order kinetic model. Inset in graph is a zoomed in region of the early growth kinetics at each overpotential.

In Figure V.8a we investigate the effects that O_2 and H_2O reformers have on graphite growth. For clarity only the kinetic traces and not the actual spectra are shown. With all concentrations of O_2, graphite formation is completely suppressed with the exception of 4:1 and 8:1 where graphite appears transiently in the 29 sec. spectra and is completely absent at later times. A similar case is observed for when CH_4 is reformed with H_2O with a molar ratio of 13:1, where graphite formation is also completely suppressed. These results, showing an absence of graphite growth, provide insight into the EIS measurements shown in Figure V.6a and V.6b showing little to no change in R_{pol} with fuel exposure time providing a direct correlation between graphite growth and electrochemical performance. The 0˚C CH_4:H_2O

reformate (with an original 56:1 CH_4:H_2O balance) does show a propensity to form graphite, Figure V.8b. Once again these *in situ* Raman measurements for CH_4:H_2O with a 56:1 molar ratio provide a direct correlation with EIS measurements because an increase in R_{pol} was observed along with graphite formations.

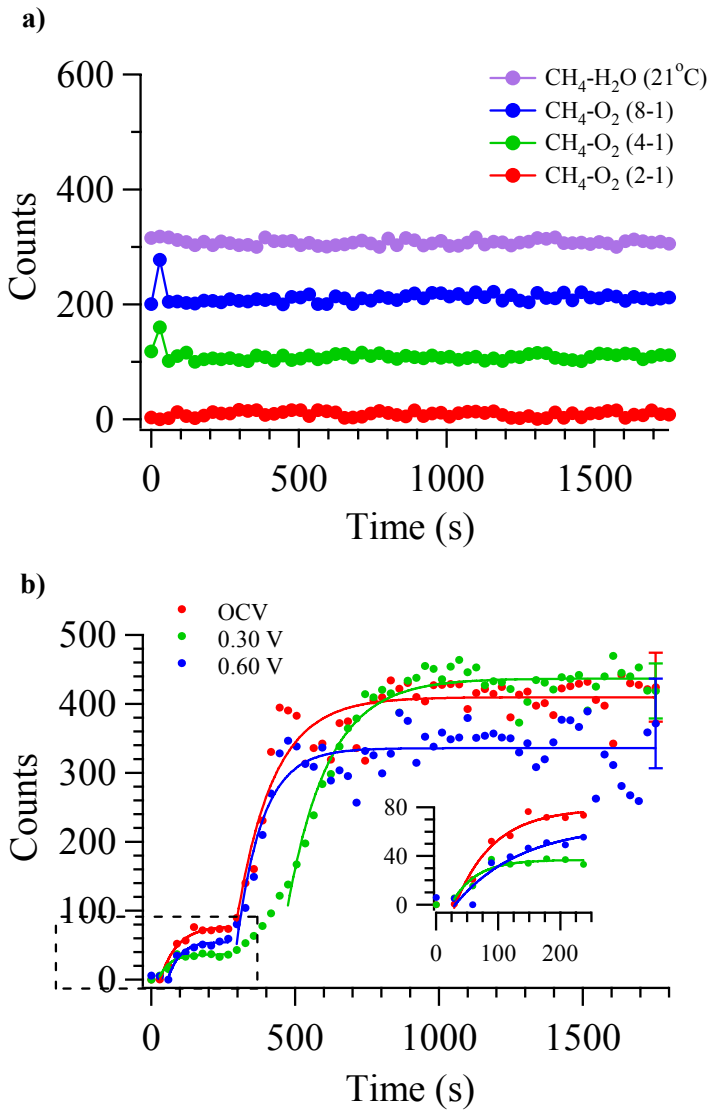

Figure V.8. *In situ* Raman measurements taken at 715˚C under various overpotential conditions with oxidative and steam reformed CH_4. a) *In situ* Raman analysis of the general kinetics of graphite growth at OCV induced by CH_4:O_2 with 2:1, 4:1, and 8:1 ratios and CH_4 humidified with H_2O with a bubbler temperature of 21˚C. b) Plot of the general kinetics of graphite growth induced by a CH_4 fuel feed humidified with H_2O at 0˚C. Inset in graph is a zoomed in region of the early growth kinetics at each overpotential with exposure to the humidified CH_4 fuel feed.

A direct correlation between graphite formation (observed in the Raman data) and changes in R_{pol} (EIS) is important for constructing accurate, predictive models of electrochemical oxidation in SOFCs. However, this correlation still requires that one infer what is happening at the anode from the structure within EIS arcs associated with anode processes. In particular, the Raman data presented above can not distinguish why EIS data show significant low frequency scatter when O_2 is used as a reformer but not with the steam reformate.

To help develop additional insight into these systems, we studied the effects that O_2 and H_2O themselves (without CH_4) had on the anode and on graphite formations created by 30 min. of exposure to direct CH_4. Representative spectra are shown in Figure V.9a and V.9b for O_2 with a flow rate of 6.25 sccm and H_2O with a flow rate of 0.89 sccm. When O_2 at a flow rate of 6.25 sccm is passed over the Ni/YSZ anode we see that the graphite formed from CH_4, is quickly oxidized and, at the same time, we begin to see the appearance of the NiO band centered at ~1100 cm^{-1}. This result can be seen in more detail in the kinetic traces presented in Figures V.10a and V.10b. O_2 as a reformer not only has the ability to oxidize graphite but also oxidizes the Ni catalyst. Ni oxidation can lead to anode delamination, a loss of catalytic activity, and a reduction in electronic conducting ability.[60-62] All of these consequences contribute to a decrease in fuel utilization that can explain the scatter in the EIS data shown in Figure V.6a. When H_2O at a flow rate of 0.89 sccm is sent over the Ni/YSZ anode we see that oxidation of the same graphite formations is delayed (~ 260 sec). What is interesting about these results is that the total volume of H_2O that was required to induce graphite oxidation is

comparable for both temperatures (~ 3.9 cm^3) and also compares favorably to the amount of oxygen in the oxidative reformed CH_4 required to oxidize the pre-formed carbon deposits. In both cases of H_2O as a reformer we observe no appearance of the NiO band at ~ 1100 cm^{-1}, further supporting the notion that scatter observed in the EIS measurements results from reversible, oxygen-induced chemistry occurring within the anode.

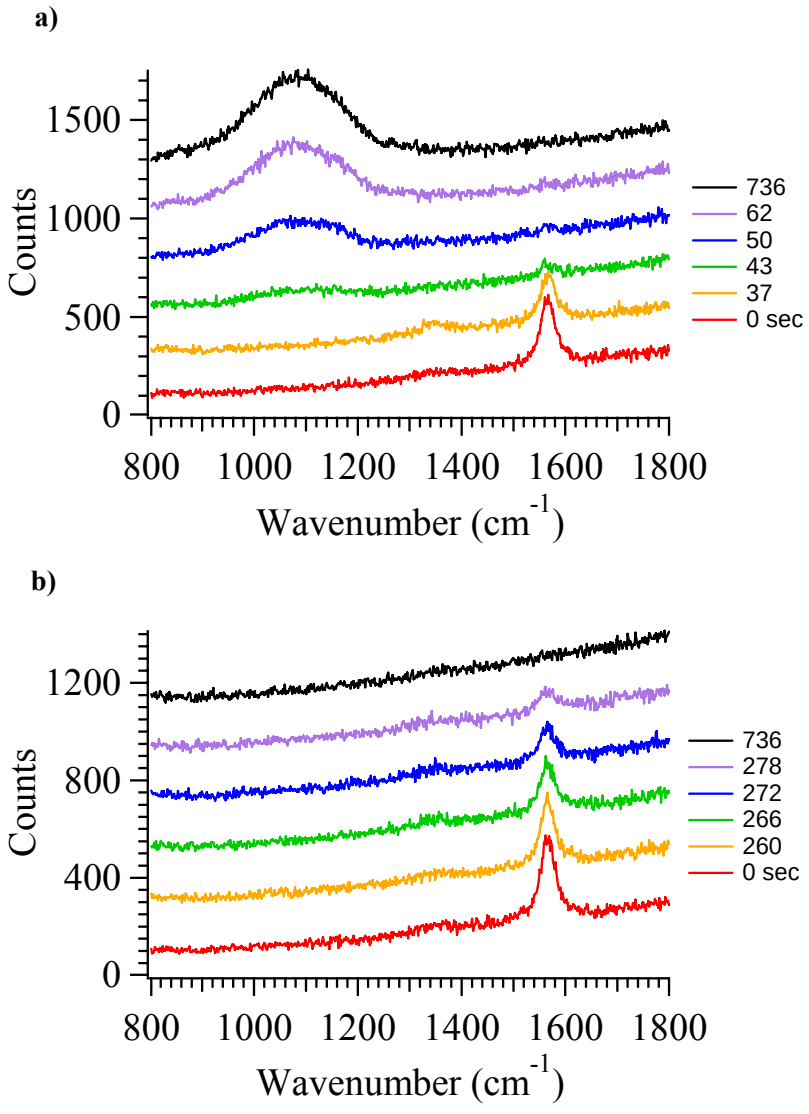

Figure V.9. *In situ* Raman measurements showing the oxidation of graphite formed from 30 min. of exposure time from direct CH_4 with a) 6.32 sccm of O_2 and b) Ar humidified with H_2O with a bubbler temperature of 0˚C.

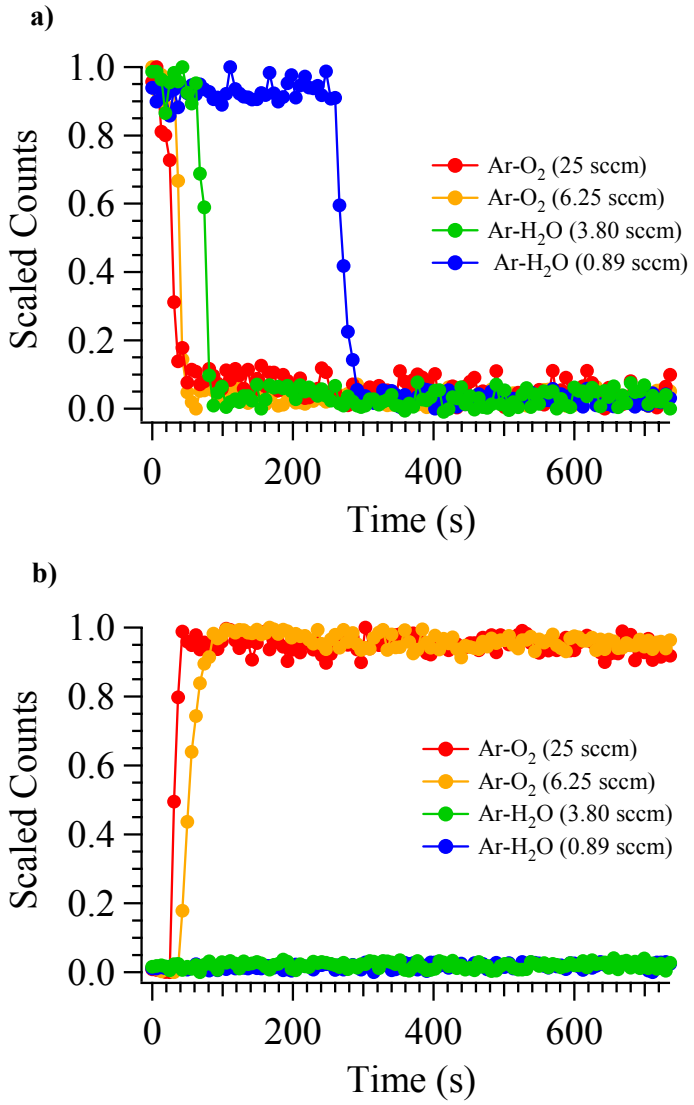

Figure V.10. *In situ* Raman analysis of the general kinetics of a) graphite oxidation and b) Ni oxidation induced by 25.0 and 6.32 sccm of O_2 and argon humidified with H_2O with bubbler temperatures of 0˚C and 21˚C. Data shown plots the intensity of the graphite "G" band at 1560 cm^{-1} (a), and the NiO band at 1100 cm^{-1} (b) with respect to exposure time of the various reformer. Spectra are acquired every ~ 5 sec.

4. Conclusions

A combination of *in situ* vibrational Raman spectroscopy and real time electrochemical impedance measurements have been used simultaneously to correlate changes observed in the electrochemical performance to real time material and

chemical changes occurring at the anode in SOFCs operating with direct and reformed methane at 715˚C. *Ex situ* FTIR measurement provided a measure of the chemical composition of the oxidative and steam reformates of methane that were impinging on the SOFC anode. Coupled *in situ* Raman and EIS measurements provided insight into the different reformate fuel mixtures and how they affected the voltage, current and power of the SOFC. Combining all these methods has led to a direct correlation between how MEA properties change and the effects these changes will have on device performance.

Voltammetry measurements revealed low fuel utilization corresponded to steep overpotential losses associated with the energy needed to activate neat methane oxidation at the anode. *In situ* Raman measurements showed that the small amount of methane that did react in the SOFC led to clearly observed deposits of highly ordered graphite. These carbon formations coincided with diminished electrochemical performance as shown by real time EIS measurements. These EIS measurements exhibited an increase in R_{pol} with respect to exposure to the direct fuel, and these changes were localized in the EIS arcs associated with anode processes.

With the introduction of an O_2 and a H_2O as reformers data showed a reduction in the magnitude of the measured OCV and a corresponding decrease in the overall potential losses associated with activation of methane. The extent of these changes was dependent on actual fuel-reformer molar ratios. FTIR measurements showed that the methane fuel was converting into a mixture of CO and CO_2 (and (H_2) for oxidative reformed methane and only CO (and H_2) for steam reformed methane. The identity of the reformate had noticeable effects on the EIS data. Oxidative

reformed methane resulted in large scatter observed in the low frequency EIS data while no such effect was observed for steam reformed methane. Both reformed mixtures led to little change in R_{pol} with extended exposure to fuel. These observations were supported by *in situ* Raman measurements showing that graphite formations were fully suppressed with high concentrations of O_2 and H_2O and at high levels of cell polarizations. The only exceptions to these observations were at early times of fuel exposures of 4:1 and 8:1 CH_4:O_2 at OCV that showed transient appearance of graphitic deposits. These responses were completely suppressed at later exposure times. The other exception to the observed trends was with CH_4:H_2O with a molar ratio of 56:1 where graphite formed and persisted on the anode.

In situ Raman measurements showed that O_2 was capable of oxidizing the Ni catalyst to NiO. In contrast, H_2O did not react with the anode to form NiO. We attribute these differences in reactivity to the cause of scatter observed in the EIS data. Other researchers have attributed fluctuations in EIS data with fluctuations in fuel utilization as might be expected if the CH_4 and the O_2 in an oxidative reforming mixture is not sufficiently mixed or allowed time to reach a thermodynamic distribution of products.

The work described in this paper was a comprehensive analysis of the oxidative and steam reforming processes taking place in SOFCs operating with methane. Introducing reformers into the methane fuel feed was beneficial because the resulting mixture increased fuel utilization *and* suppressed carbon formation. Unlike previous experimental studies of anode behavior with different fuel mixtures, the use of *in situ* Raman spectroscopy provided unprecedented insight in the material-

specific information needed to test proposed models of electrochemical oxidation of these devices. We hope that the ability to differentiate mechanisms of SOFC operation as a function of fuel identity and cell polarization will help guide the development of new SOFC materials and architectures.

5. References

(1) Song, C. *Catal. Today*, **2002**, *77*, 17.

(2) Ormerod, R. *Chem. Soc. Rev.*, **2003**, *32*, 17.

(3) Pomfret, M.; Demircan, O.; Sukeshini, M.; Walker, R. *Environ. Sci. Technol.*, **2006**, *40*, 5574.

(4) Brett, D.; Atkinson, A.; Brandon, N.; Skinner, S. *Chem. Soc. Rev.*, **2008**, *37*, 1568.

(5) Kendall, K. *Int. Mater. Rev.*, **2005**, *50*, 257.

(6) Gorte, R.; Park, S.; Vohs, J.; Wang, C. *Adv. Mater.*, **2000**, *12*, 1465.

(7) Gorte, R.; Kim, H.; Vohs, J. *J. Power Sources*, **2002**, *106*, 10.

(8) Kee, R. Zhu, H.; Goodwin, D. *Proc. Combust. Inst.*, **2005**, *20*, 2379.

(9) McIntosh, S.; Vohs, J.; Gorte, R. *J. Electrochem. Soc.*, **2003**, *150*, A470.

(10) McIntosh, S.; He, H.; Lee, S.; Costa-Nunes, O.; Krishnan, V.; Vohs, J.; Gorte, R. *J. Electrochem. Soc.*, **2004**, *151*, A604.

(11) Pomfret, M.; Marda, J.; Jackson, G.; Eichhorn, B.; Dean, A.; Walker, R. *J. Phys. Chem. C*, **2008**, *112*, 5232.

(12) Randolph, K.; Dean, A. *Phys. Chem. Chem. Phys.*, **2007**, *9*, 4245.

(13) Atkinson, A.; Barnett, S.; Gorte, R.; Irvine, J.; Mcevoy, A.; Mogenson, M.; Singhal, S.; Vohs, J. *Nat. Mat.*, **2004**, *3*, 17.

(14) Mogensen, M.; Kammer, K. *Annual Rev. Mater. Res.*, **2003**, *33*, 321.

(15) Liu, J. *Prog. Chem.*, **2006**, *18*, 1026.

(16) Minh, N. *Solid State Ionics*, **2004**, *174*, 271.

(17) Qiao, J.; Sun, K.; Zhang, N.; Sun, B.; Kong, J.; Zhou, D. *J. Power Sources*, **2007**, *169*, 253.

(18) Rossmeisl, J.; Bessler, W. *Solid State Ionics*, **2008**, *178*, 1694.

(19) Decaluwe, S.; Zhu, H.; Kee, R.; Jackson, G. *J. Electrochem. Soc.*, **2008**, *155*, B538.

(20) Kakac, S.; Pramuanjaroenkij, A.; Zhou, X. *Int. J. Hydrogen Energy*, **2007**, *32*, 761.

(21) Zhu, H.; Kee, R. *J. Electrochem. Soc.*, **2006**, *153*, A1765.

(22) Zhu, W.; Deevi, S. *Mater. Sci. Eng. A.*, **2003**, *362*, 228.

(23) Bieberle, A.; Gauckler, L. *Solid State Ionics*, **2000**, *135*, 337.

(24) Bieberle, A; Meier, L.; Gauckler, L. *J. Electrochem. Soc.*, **2001**, *148*, A646.

(25) Sukeshini, A.; Habibzadeh, B.; Becker, B.; Stoltz, C.; Eichhorn, B.; Jackson, G. *J. Electrochem. Soc.*, **2006**, *153*, A705.

(26) Zhu, H.; Kee, R.; Janardhanan, V.; Deutschmann, O.; Goodwin, D. *J. Electrochem. Soc.*, **2005**, *152*, A2427.

(27) Pomfret, M.; Owrutsky, J.; Walker, R. *Anal. Chem.*, **2007**, *79*, 2367.

(28) Pomfret, M.; Stoltz, C.; Varughese, B.; Walker, R. *Anal. Chem.*, **2005**, *77*, 1791.

(29) Swider, K; Worrell, W. *J. Electrochem. Soc.*, **1996**, *143*, 3706.

(30) Sammes, N.; Cai, Z. *Solid State Ionics*, **1997**, *100*, 39.

(31) Lee, J.; Yoon, S.; Kim, B.; Kim, J.; Lee, H.; Song, H. *Solid State Ionics*, **1997**, *144*, 175.

(32) Svensson, A.; Sunde, S.; Nisancioglu, K. *J. Electrochem. Soc.*, **1998**, *145*, 1390.

(33) Nielsen, J.; Jocobsen, T. *Solid State Ionics*, **2008**, *178*, 1769.

(34) Goodenough, J. *Annu. Rev. Mater. Res.*, **2003**, *33*, 91.

(35) Devanathan, R.; Weber, W.; Singhal, S.; Gale, J. *Solid State Ionics*, **2006**, *177*, 1251.

(36) Douvartzides, S.; Coutelieris, F.; Demin, K.; Tsiakaras, P. *AlChE J.*, **2003**, *49*, 248.

(37) Laosiripojana, N.; Assabumrungrat, S. *J. Power Sources*, **2007**, *163*, 943.

(38) Staniforth, J.; Ormerod, R. *Green Chemistry*, **2001**, *3*, G61.

(39) Murray, E.; Tsai, T.; Barnett, S. *Nature*, **1999**, *400*, 649.

(40) Muradov, N. *Energy & Fuels*, **1998**, *12*, 41.

(41) Finnerty, C.; Coe, N.; Cunningham, R.; Ormerod, R. *Catal. Today*, **1998**, *46*, 137.

(42) Blanksby, S.; Ellison, B. *Acc. Chem. Res.*, **2003**, *36*, 255.

(43) Ishihara, T.; Hiei, Y.; Takita, Y. *Solid State Ionics*, **1995**, *79*, 371.

(44) Macek, J.; Novosel, B.; Marinnsek, M. *J. Eur. Ceram. Soc.*, **2007**, *27*, 487.

(45) Norinaga, K.; Dutschmann, O. *Ind. Eng. Chem. Res.*, **2007**, *46*, 3547.

(46) Coutelieris, F.; Douvartzides, S.; Tsiakaras, P. *J. Power Sources*, **2003**, *123*, 200.

(47) Dokmaingam, P; Assabumrungrat, S.; Soottitantawat, A.; Laosiripojana, N. *J. Power Sources*, **2010**, *171*, 69.

(48) Nikooyeh, K.; Jeje, A.; Hill, J. *J. Power Sources*, **2007**, *171*, 601.

(49) Rakass, S.; Oudghiri-Hassani, H.; Rowntree, P.; Abatzoglou, N. *J. Power Sources*, **2006**, *158*, 485.

(50) Suwanwarangkul, R.; Croiset, E.; Entchev. E.; Charojrochkul, S.; Pritker, M.; Fowler, M.; Douglas, P.; Chewathanakup, S.; Mahaudom, H. *J. Power Sources*, **2006**, *161*, 308.

(51) Walters, K.; Dean, A.; Zhu, H.; Kee, R. *J. Power Sources*, **2003**, *123*, 182.

(52) Recknagle, K.; Ryan, E.; Koeppel, B.; Mahoney, L.; Khaleel, M. *J. Power Sources*, **2010**, *195*, 6637.

(53) Li, Y.; Chen, J.; Qin, Y.; Chang, L. *Energy & Fuels*, **2000**, *14*, 1188.

(54) Finnerty, C.; Tompsett, G.; Kendall, K.; Ormerod, R. *J. Power Sources*, **2000**, *86*, 459.

(55) Hofmann, P.; Panopoulos, K. *J. Power Sources*, **2010**, *195*, 5320.

(56) Eigenbrodt, B.; Pomfret, M.; Steinhurst, D.; Owrutsky, J.; Walker, R. *J. Phys. Chem. C*, **2011**, *115*, 2895.

(57) Pomfret, M.; Owrutsky, J.; Walker, R. *J. Phys. Chem. B*, **2006**, *110*, 17305.

(58) Matheu, D.; Dean, A.; Grenda, J.; Grean, W. *J. Phys. Chem. A*, **2003**, *107*, 8552.

(59) Cimenti, M.; Biriss, V.; Hill, J. *Fuel Cells*, **2007**, *5*, 377.

(60) Tikekar, N.; Armstrong, T.; Virkar, A. *J. Electrochem. Soc.*, **2006**, *153*, A654.

(61) Fouquet, D.; Muller, A.; Weber, A.; Ivers-Tiffte, E. *Ionics*, **2003**, *9*, 103.

(62) Stathis, G.; Simwonis, D.; Tietz, F.; Moropoulou, A.; Naoumides, A. *J. Mater. Res.*, **2002**, *17*, 951.

Chapter 6: *In situ* Optical Studies of Solid Oxide Fuel Cells Operating with Dry and Humidified Ethanol

1. Introduction

Solid oxide fuel cells (SOFCs) are attractive energy producing devices because they are fuel flexible and able to operate with complex fuel mixtures, including hydrocarbons and oxygenated fuels.[1-4] The high operating temperatures of SOFCs ($\geq 650^{\circ}C$) can lead to significant fuel reforming meaning that higher molecular weight fuels often break down into simpler, more labile species prior to reaching electrochemically active sites on the anode.[5,6] Fuel flexibility coupled with the relatively high tolerance to contaminants confer to SOFCs distinct advantages over other devices such as polymer electrolyte membrane fuel cells (PEMFCs) and direct methanol fuel cells (DMFCs), where species such as CO deactivate electrochemically active sites.[7] Furthermore, SOFCs can be manufactured from relatively inexpensive materials and can be integrated easily into stacked systems for use in commercial applications where CO is often a significant species in the fuel feed.[8]

While the overall description of SOFC operation is straightforward, detailed, validated mechanisms describing the processes occurring on SOFC cathodes and anodes can be more tenuous. The high activation energy for oxygen-ion diffusion through the electrolyte (100 kJ/mol) and the large barrier to molecular oxygen activation at the cathode (223 kJ/mol) require that SOFCs operate at high temperatures.[9,10] This condition poses significant experimental challenges for

studying SOFC chemistry in situ and in real time. In particular, most experimental approaches used to study SOFC chemistry are limited in their ability to identify directly mechanisms responsible for SOFC degradation and failure. Electrochemical measurements can correlate declining performance with specific operating conditions, but these studies can not isolate the chemical or structural evolution responsible for the observed change(s) in device performance. Ex situ studies provide important information about the final state of materials that comprise individual SOFC components but these studies can be carried out only after a SOFC has been cooled and disassembled.

One major cause of SOFC degradation is the formation of carbon deposits.[7] Carbon formed from incomplete oxidation of hydrocarbon fuels or from large carbon clusters formed from gas phase pyrolysis is thought to block active sites on SOFC anodes leading to lower overall fuel conversion efficiencies and eventual anode failure.[8,11] This process is particularly problematic on Ni-based anodes since they are effective hydrocarbon cracking catalysts.[8] Models describing carbon growth have been developed without direct evidence of when and where carbon deposits start to form, how quickly deposited carbon grows and how cell conditions affect the rates and mechanisms of carbon growth.[12,13]

One strategy for inhibiting carbon growth on SOFC anodes is to use oxygenated and/or humidified fuels.[12,14] Methanol and ethanol, in particular, are popular fuels given their ease of storage, relatively high energy densities and active reforming chemistry.[6,15] Previous work has shown, however, that methanol has a much greater tendency to form graphite in operating SOFCs compared to the

analogous alkane, methane.[16] In addition, several reports have noted that SOFC operation with ethanol can be unstable but adding humidity to an ethanol fuel feed improves SOFC anode durability.[6,17]

The differing effects of the dry and humidified ethanol fuel feeds on SOFC performance and durability have been observed previously in electrochemical measurements and have been modeled extensively.[6,17] However, conclusions from these studies depend either on data that report only indirectly of species present on the SOFC anode during operation or on ex situ, post mortem analyses performed after the device has been disassembled.[6,17]

In experiments described below, we use a combination of ex situ FTIR exhaust measurements, in situ Raman vibrational measurements and electrochemical impedance analyses to compare the behaviors of dry and humidified ethanol fuel feeds in SOFCs operating at 715˚C. The two compositions that were used consisted of a 100 % direct ethanol (dry) fuel feed (diluted in Argon) and a, 50:50 (by % vol) mixture of ethanol/H_2O (humidified) fuel feed (also diluted in Argon). IR analysis of the SOFC exhaust provides insight into the reforming products produced by each original fuel feed and reveals that dry ethanol decomposes to form –among other species– acetylene, a known gas phase precursor to rapid carbon growth. Adding H_2O to the fuel feed minimizes the formation of acetylene.

Data from in situ Raman experiments show that SOFCs operating close to open circuit conditions suffer rapid graphite deposition from both dry and humidified ethanol and that these conditions also lead to the most significant decrease in performance as evidenced by EIS measurements. Polarizing reduces the rate of

graphite formation, and in some cases, graphite formation is completely suppressed. These results demonstrate that the tendency of carbon containing fuels to form graphitic deposits depends sensitively on cell polarization and gas phase composition. The work described below demonstrates the ability of analytical optical and electrochemical methods to provide unprecedented insight into the kinetics and consequences of SOFC chemistry.

2. Experimental

2A. SOFC Membrane Electrode Assembly

The electrolyte-supported SOFCs used in these experiments are similar to those used in previous studies.[4,16] The electrolyte-supported membrane electrolyte assemblies (MEAs) consist of a 30 ± 5 μm thick, sintered NiO/yttria-stabilized zirconia (YSZ) cermet anode (66 % NiO by mass) and a 30 ± 5 μm thick, sintered lanthanum strontium manganite (LSM)/YSZ cermet cathode (50 % LSM by mass). The electrolytes are ~ 2.5 cm in diameter and 0.80 ± 0.02 mm thick YSZ disks and are fabricated in our laboratories. Details regarding the actual construction of these devices can be found in refs.[4,16] Platinum paste (Heraeus) was used to attach platinum mesh (Alfa Aesar) and gold wire (Alfa Aesar) to the cathode as a current collector, while gold paste (Heraeus) was used to attach silver mesh (Alfa Aesar) and gold wire to the anode to be used as the current collector.

2B. Gas Flows

Air/argon (to the cathode) and fuel/argon (to the anode) flows were controlled using rotameters. Dry and humidified ethanol was introduced into the SOFC using a

bubbler filled with either 100 % ethanol or 50:50 (% vol.) mixture of ethanol/H_2O. A carrier gas of argon was used to transport the vapor into the fuel cell chamber at a flow rate of 94 sccm through 4.5 mm inner-diameter feed tubs. Total pressures on both sides of the MEA were approximately 1 atm. Our original measurements found that the use of dry ethanol led to rapid degradation of the Ni/YSZ anode at 715°C. We assumed that this effect resulted from Ni's catalytic capability that promoted extensive carbon growth and subsequent delamination of the anode from the electrolyte. (Figure VI.1) Setting the bubbler in an ice bath lowered the flow rate of pure ethanol from 5.4 sccm at 20˚C to 1.5 sccm at 0˚C and allowed the anode to survive longer to perform measurements. When compared to the dry ethanol fuel feed, the humidified fuels vapor pressures were reduced with addition of H_2O. The total flow rate of the humidified fuel was 0.85 sccm with a vapor composition of 60:40 (mol %) of ethanol to H_2O.

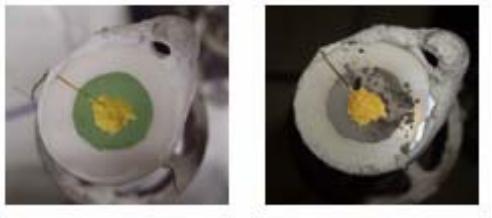

Figure VI.1. (Left) Picture of NiO/YSZ anode before operation under ethanol conditions. (Right) Picture of same anode after operation with ethanol. This SOFC was cooled down under reducing conditions (H_2/Ar) leaving behind the partially delaminated Ni/YSZ anode.

2C. Electrochemical Measurements

All electrochemical measurements and overpotential conditioning experiments were performed using a Princeton Applied Research VMC-2 potentiostat/galvanostat/FRA. In a typical experiment, the SOFC was first tested

using linear sweep voltammetry and electrochemical impedance spectroscopy (EIS), with a mixture of 94 sccm argon and 100 sccm hydrogen on the anode side and 100 sccm air and 94 sccm argon on the cathode side. Similar measurements were performed at various times during an experimental run and compared to initial benchmark results to assess device durability. To observe the changes in electrochemical performance when using either the dry or humidified ethanol fuel feeds, EIS measurements were performed continuously and concurrently with *in situ* Raman spectroscopic measurements. The chemistry and performance of the SOFC were studied at different cell overpotentials using the two different fuel feeds. During impedance measurements, the potentiostat polarized the SOFC to well-defined overpotentials with respect to open circuit voltage (OCV). OCV typically measured -1.15 ± 0.05 V, and the overpotentials used in these experiments were 0.30, 0.45, and 0.60 V. Here, overpotential (V_{OP}) refers to the difference between OCV and the voltage across the operating cell ($V_{OP} = V_{CELL} - V_{OCV}$).

2D. *In situ* Raman Measurements

An important requirement of these studies is the need for optical access into the device. This condition was met by surrounding the entire SOFC with an optically transparent quartz tube so that *in situ* Raman measurements could be performed on the anode surface. This assembly has been described in more detailed previously.[4,16,18] The Raman assembly utilizes custom built microscope optics used both for excitation and collection of scattered radiation normal to the anode. In the Raman scattering experiments, 488 nm light (8mW) is focused onto the anode, and backscattered light is collected and sent to the charged couple device (CCD) detector

(Renishaw, inVia). Even though a 15 mm long working distance objective is used, the objective itself sits close to the cell limiting MEA operational temperatures to < 730˚C. (The microscope objective heats to ~180˚C). Temperatures are maintained by positioning the anode near the top of an open-ended tube furnace. A consequence of this design is that the fuel being studied traverses a high-temperature region in the middle of the furnace and spends ~ 0.03 seconds at temperatures ≥ 900˚C. These temperatures can lead to significant reforming, so *ex situ* FTIR spectroscopy was used to quantify exhaust composition.

3. Results and Discussion

At the elevated temperatures found in operating SOFCs, ethanol tends to form C_2 pyrolysis products that are known to be precursors for rapid graphite growth on Ni anode surfaces.[4,19] To quantify the gas phase fuel composition reaching our Ni-YSZ cermet anode, FTIR spectroscopy was used to analyze the products formed from dry ethanol and the ethanol-water mixture after the fuels had made a single pass through the high temperature region of the furnace. Results are shown in Figure VI.2. Both the dry and humidified fuels formed acetylene (C_2H_2) and CO. The dry ethanol feed formed approximately two times more C_2H_2 and 25 % more CO than the humidified fuel. The humidified feed contained significantly more CO_2. Quantifying these results using a Beer's Law analysis shows that CO and CH_4 are the primary pyrolysis products. Partial pressures of CO, CH_4 and C_2H_2 for the dry (wet) feed were 0.14 atm (0.11 atm), 0.07 atm (0.04 atm) and 0.007 atm (0.002 atm) respectively.[20] Noteworthy is the absence of any ethanol in the fuel feed after passing through the high temperature region of the furnace. The relatively large amounts of acetylene

formed by the dry ethanol virtually assure that this fuel will lead to rapid graphite formation and irreversible anode degradation.[4,19]

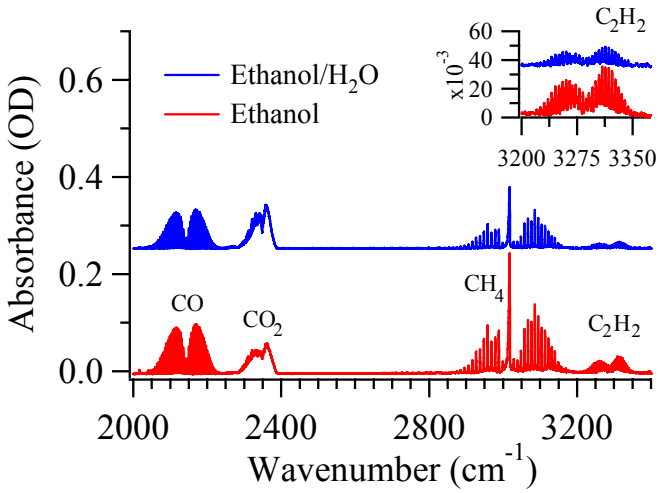

Figure VI.2. *Ex situ* FTIR spectra of SOFC exhaust where the SOFC operates with a pure ethanol (in Ar) feed (blue) or humidified ethanol (red). The top inset shows blown up region of the C_2H_2 band center at 3285 cm^{-1}. Humidified spectra have been offset for clarity.

Knowing the gas phase composition of the fuel mixture reaching the anode, we can begin to interpret the *in situ* changes in molecular and material species taking place in the SOFC assembly. Vibrational Raman spectra acquired from SOFC anodes operating at different overpotentials show that the humidified ethanol feed leads to graphite formation at OCV and 0.30 V overpotential, but not at 0.60 V overpotential. (Figure VI.3) Each spectrum represents a ~ 5 sec. acquisition, and for clarity only three spectra taken at different exposures are shown for each cell polarization. Several observations stand out. The first observation is the appearance of a strong sharp feature at ~ 1560 cm^{-1} in most of the spectra, especially those acquired at OCV. This feature is referred to as the "G" band of graphite and is characteristic of a highly

ordered, sp^2 hybridized carbon network with minimal defects and/or grain boundaries.[4,16] A second observation from these spectra is that the probability of forming graphite on the anode surface increases as the voltage approaches open circuit conditions and is completely suppressed at higher overpotentials (0.60 V). We propose that these higher overpotentials drive enough electrochemical oxidation to keep carbon from accumulating at the anode active sites. The third observation implicit in these individual spectra is that the kinetics of graphite formation depends on cell overpotential. Little change is observed in the spectra acquired at 200 and 843 sec. when the SOFC is at OCV, but when the cell is polarized to 0.30 V overpotential, the graphite is clearly continuing to grow over the course of ~ 10-12 minutes.

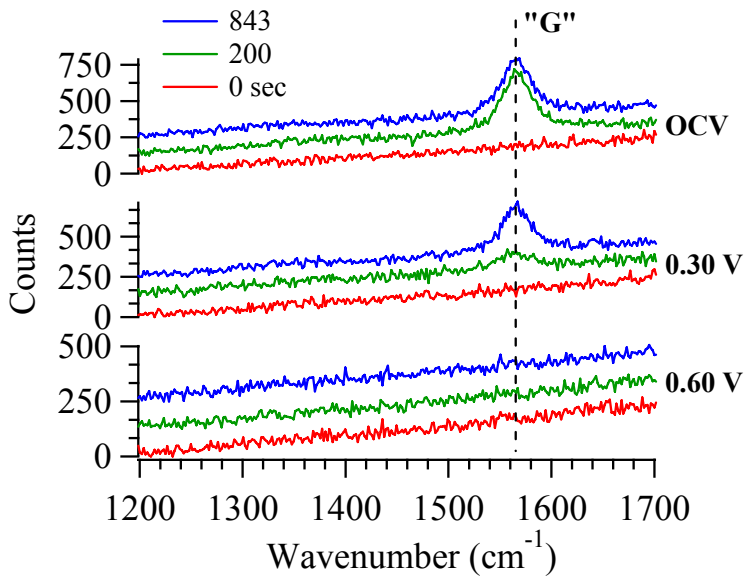

Figure VI.3. *In situ* Raman measurements taken at 715˚C under various overpotential conditions with humidified ethanol. Showing graphite growth as a function of exposure to ethanol/H_2O and polarization. Each spectrum represents a 5 sec. acquisition. For clarity the 0, 200 and 843 sec. are chosen for each overpotential case a) OCV, b) 0.30 V, c) 0.60 V. 200 & 843 sec. spectra are offset for clarity.

Figure VI.4 highlights these differences in graphite growth kinetics. The data show the intensity of the 1560 cm^{-1} band with respect to time. Spectra were acquired

continuously in ~ 5 sec. intervals with the cell polarized to different overpotentials. At OCV graphite forms immediately, accumulates quickly, and reaches an asymptotic limit after ~ 150 sec. These data can be described quite well with a simple, first order kinetic model. As the SOFC is polarized, the onset of graphite formation is delayed and graphite growth kinetics is more complicated. Such behavior is consistent with autocatalytic mechanisms that require the nucleation of a seed followed by rapid growth.[8,11] A point worth noting is that higher overpotentials appear to inhibit the initial onset of graphite growth and growth is inhibited completely at the highest overpotential tested in this work (0.60 V).

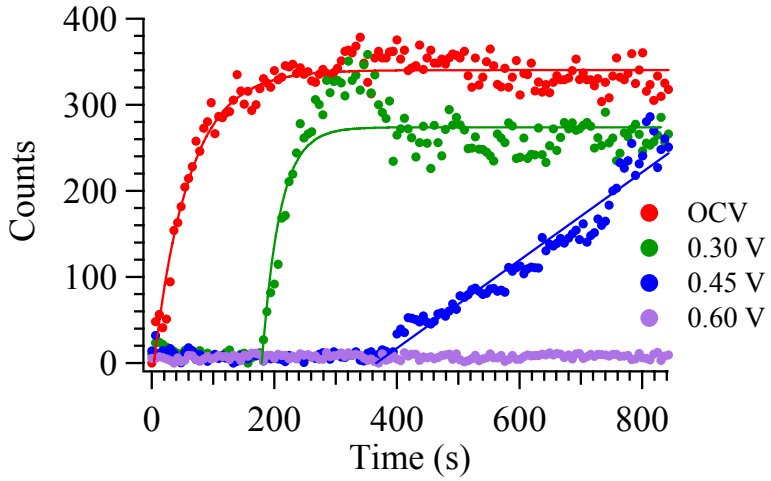

Figure VI.4. *In situ* Raman analysis of the general kinetics of graphite growth induced by a humidified ethanol feed. Data shown plots the intensity of the graphite "G" band at 1560 cm^{-1} with respect to exposure time of the humidified fuel feed at various overpotentials. Spectra are acquired every 5 sec.

Coupling these in situ Raman spectra with EIS measurements acquired simultaneously provides insight into how graphite formation affects SOFC electrochemical performance. Figure VI.5 shows EIS data from SOFCs at OCV, 0.30 V and 0.60 V overpotentials exposed to the 50:50 ethanol:water fuel feed. There

is a direct correlation between rapid graphite formation and the increase in device impedance (corresponding to diminished performance). Graphite growth is most rapid in SOFCs held at OCV. As the graphite forms, EIS measurements show a ~ 28 % increase in the polarization resistance (R_{pol}) taken at OCV. The entire MEA is modeled by a Randle's circuit with three separate RC elements in series,[21] the growth of R_{pol} is associated primarily with an increase in the second (middle) arc. This second arc is associated with charge transfer reactions occurring at the anode.[21] An increase in this arc indicates that the graphite formations are blocking sites and disrupting connectivity throughout the anode.

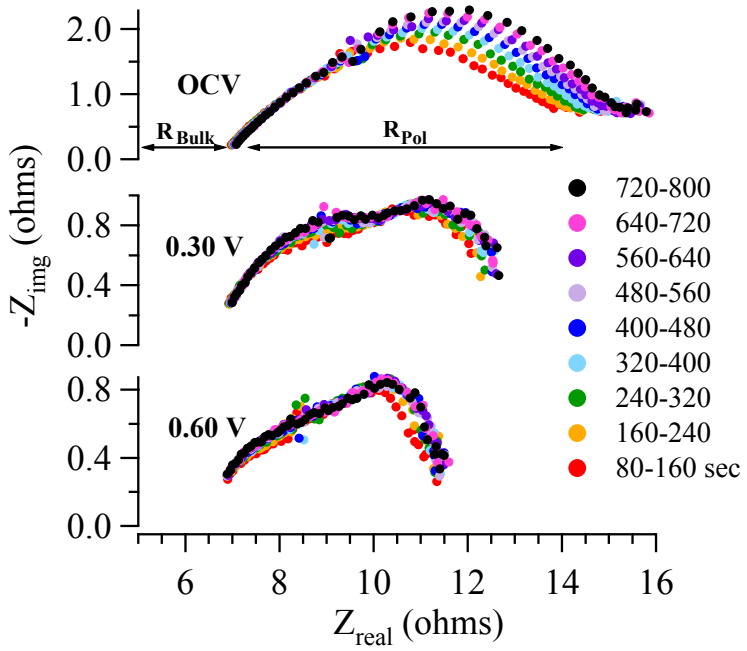

Figure VI.5. Real time EIS measurement taken simultaneously with *in situ* Raman measurements at different overpotentials with humidified fuel feed. EIS measurements were taken at a) OCV, b) 0.30 V and, c) 0.60 V. Peak frequencies: ~ 25 Hz (high frequency arc), ~ 4.0 Hz (middle frequency arc), and ~ 500 mHz (low frequency arc)

Just as polarizing the cell affected the extent and rate of graphite formation, polarizing the cell also has profound affects on SOFC performance as observed in the EIS data. Polarized MEAs exposed to humidified ethanol show minimal to no change in the R_{pol}, with a $\sim 10\,\%$ increase of $0.30\,V$ and $\sim 5\,\%$ increase for $0.60\,V$. Therefore, we conclude that in polarized cells, even though the Raman data show that graphite is forming on the anode surface, these deposits have minimal affects on the electrochemically active sites associated with charge transfer and electrochemical fuel oxidation.

Similar measurements were performed with SOFCs operating with a dry ethanol fuel feed at various overpotentials. Just like the humidified feed, we observe the same peak at $\sim 1560\,cm^{-1}$ being formed, representing highly ordered carbon deposits. (Figure VI.6a) Here, we note that our experiments were unable to monitor graphite formation in SOFCs at OCV exposed to a dry ethanol feed. Under these conditions, the anode underwent rapid, visible degradation and delamination. Consequently, we used an overpotential of $0.15\,V$ to slow the rate of anode degradation and allow experiments to measure rates of carbon formation and growth of R_{pol}.

The first point to note from the data shown in Figure VI.6 is that no applied polarization is large enough to prevent the graphite formation in these SOFCs exposed to dry ethanol. However, graphite growth appears to stem from two separate growth mechanisms, a slow first order step and a faster first order reaction, Figure VI.6b. Whether or not one mechanism can be favored over another by means of operating conditions is an interesting question that deserves further investigation.

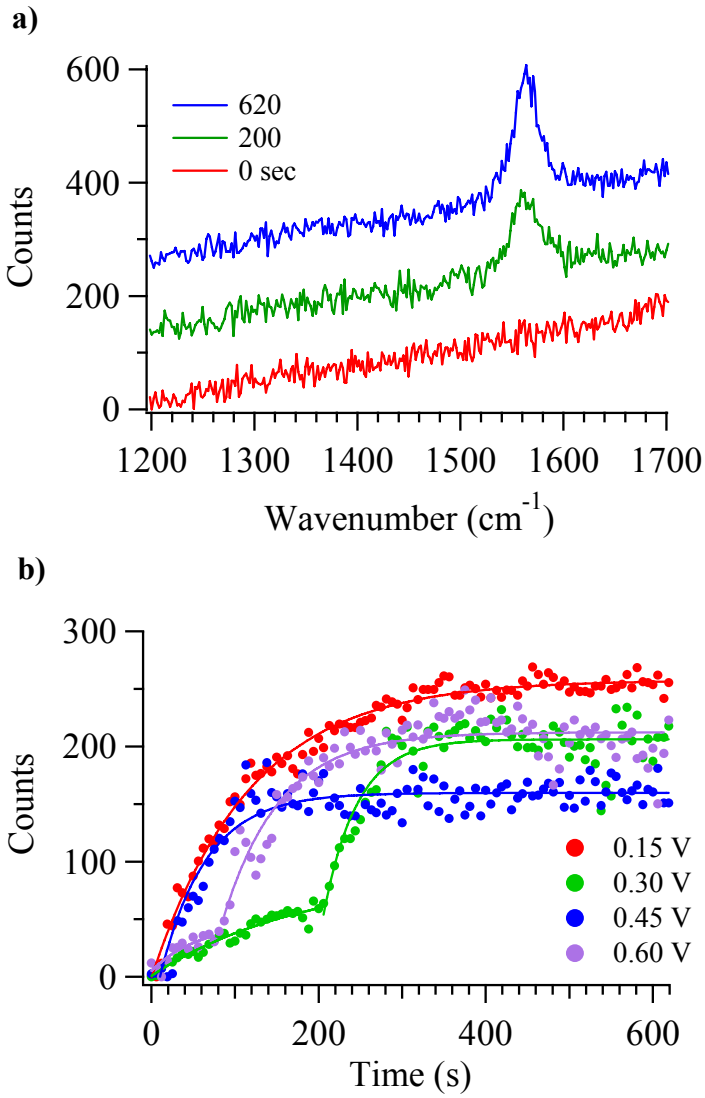

Figure VI.6. *In situ* Raman measurements taken at 715˚C of SOFC anode operating with dry ethanol fuel feed. a) Raman spectra taken of SOFC operating at 0.60 V overpotential, each spectrum represents a 5 sec acquisition. For clarity the 0, 200 and 620 sec. were chosen. b) Monitoring the height of the graphite "G" band at ~ 1560 cm^{-1} with respect to exposure time and various overpotentials.

It is first noticed in Figure VI.7 that the relative values for R_{bulk} and R_{pol} are larger for the dry than compared to what was observed for the humidified fuel, although these values might vary from cell to cell, this pattern remains consistent. At the lowest overpotential sampled (0.15 V), graphite formation is again accompanied by significant growth in R_{pol}. (Figure VI.7) The observed increase in R_{pol} is much

larger than what was observed for the OCV anode exposed to humidified ethanol with a ~ 66 % increase. Polarizing the cell again diminishes the changes to R_{pol} induced by carbon formation. One final observation from the EIS measurements in Figure VI.7 is that R_{bulk} changes in SOFCs exposed to dry ethanol. Such changes were not observed with the humidified fuel. This change in R_{bulk} implies that the connection between the anode and the electrolyte is becoming compromised with exposure to dry ethanol.

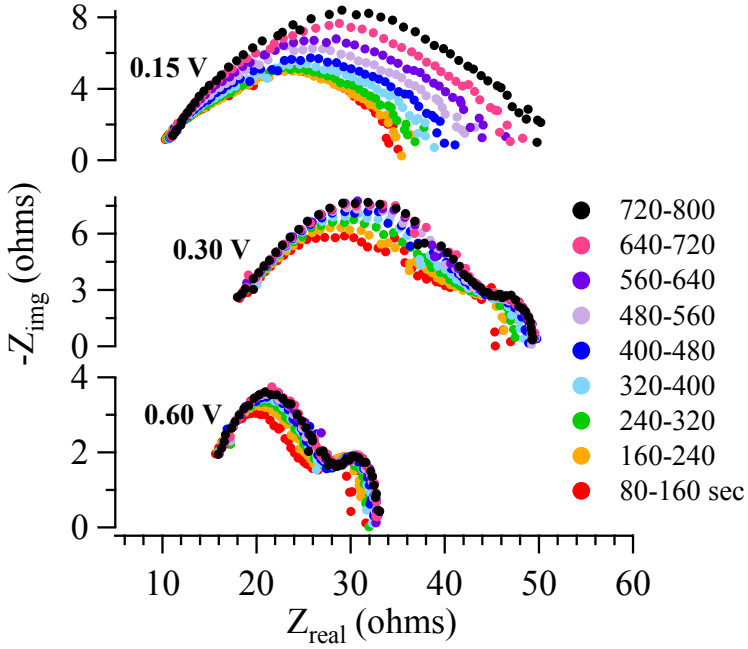

Figure VI.7. Real time EIS measurement taken simultaneously with *in situ* Raman measurements at different overpotentials with dry fuel feed. EIS measurements were taken at a) OCV, b) 0.30 V and, c) 0.60 V. Peak frequencies: ~ 630 Hz (high frequency arc), ~ 10 Hz (middle frequency arc), and ~ 158 mHz (low frequency arc)

4. Conclusions

The combination of ex situ FTIR, in situ Raman, and EIS measurements were used to examine the effects that dry and humidified ethanol have on SOFC performance. It was found that both dry and humidified ethanol form a mixture of CO, CH_4, CO_2, and C_2H_2 before reaching the anode. Humidified ethanol (60:40 ethanol:water by mole fraction) led to rapid growth of graphitic carbon when the cell was held at OCV, but polarizing the device slowed carbon growth. Graphite growth was completely suppressed at the highest overpotentials (0.60 V). EIS measurements showed that rapid carbon growth was accompanied by significantly diminished electrochemical performance. This effect was much less noticeable in polarized cells, even when Raman data showed the clear presence of carbon depositions. Dry ethanol feeds contained significantly more C_2H_2 as a pyrolysis product and these feeds led to instantaneous graphite formation and rapid growth, regardless of cell polarization. These direct in situ optical measurements coupled with corresponding data from electrochemical measurements are beginning the provide the information necessary for testing proposed mechanisms of carbon deposition and device degradation in SOFCs operating with oxygenated fuels.

5. References

(1) Brett, D.; Atkinson, A.; Brandon, N.; Skinner, S. *J. Chem. Soc. Rev.*, **2008**, *37***,** 1568.

(2) Kee, R.; Zhu, H.; Goodwin, D. *Proc. Combust. Inst.*, **2005,** *30***,** 2379.

(3) Mogensen, M.; Kammer, K. *Annual Rev. Mater. Res.*, **2003,** *33***,** 321.

(4) Pomfret, M.; Marda, J.; Jackson, G.; Eichhorn, B.; Dean, A.; Walker, R. *J. Phys. Chem. C*, **2008,** *112***,** 5232.

(5) Pomfret, M.; Demircan, O.; Sukeshini, M.; Walker, R. *Environ. Sci. Technol.*, **2006,** *40***,** 5574.

(6) Cimenti, M.; Hill, J. *J. Power Sources*, **2009,** *186***,** 377.

(7) McIntosh, S.; He, H.; Lee, S.; Costa-Nunes, O.; Krishnan, V.; Vohs, J.; Gorte, R. *J. Electrochem. Soc.*, **2004,** *151***,** A604.

(8) Ormerod, R. *Chem. Soc. Rev.*, **2003,** *32***,** 17.

(9) Erning, J.; Hauber, T.; Stimming, U. Wippermann, K. *J. Power Sources*, **1996,** *61***,** 205.

(10) Goodenough, J. *Annual Rev. Mater. Res.*, **2003,** *33***,** 91.

(11) Sun, C.; Stimming, U. *J. Power Sources*, **2007,** *171***,** 247.

(12) Coutelieris, F.; Douvartzides, S.; Tsiakaras, P. *J. Power Sources*, **2003,** *123***,** 200.

(13) Dokmaingam, P.; Assabumrungrat, S.; Soottitantawat, A.; Laosiripojana, N. *J. Power Sources*, **2010**, *195***,** 69.

(14) Cimenti, Hill, J. M.; *J. Power Sources*, **2010,** *195***,** 3996.

(15) Brett, D.; Atkinson, A.; Cumming, D.; Rameriz-Cabrera, E.; Rudkin, R.; Brandon, N. *Chem. Eng. Sci.*, **2005,** *60***,** 5649.

(16) Eigenbrodt, B.; Pomfret, M.; Steinhurst, D.; Owrutsky, J.; Walker, R. *J. Phys. Chem. C*, **2011,** *115***,** 2895.

(17) Jiang, Y.; Virkar, A. *J. Electrochem. Soc.*, **2001,** *148***,** A706.

(18) Pomfret, M.; Owrutsky, J.; Walker, R. *Anal. Chem.*, **2007,** *79***,** 2367.

(19) Villano, S.; Hoffmann, J.; Carstensen, H.; Dean, A. *J. Phys. Chem. C*, **2010,** *114***,** 6502.

(20) http://webook.nist.gov, NIST Standard Reference Database, Quantitative Infrared Database.

(21) Laurencin, J.; Delette, G.; Sicardy, O.; Rosini, S.; Lefebvre-Joud, F. *J. Power Sources*, **2010,** *195***,** 2747.

Chapter 7: Conclusions and Future Directions

1. Conclusions

The research described in this thesis has investigated anode and electrolyte chemistry occurring in operating SOFCs at 715˚C. Specifically, this work uses newly developed *in situ* vibrational Raman spectroscopy to explore the effects of gas-phase fuel composition and electrochemical potential on YSZ oxidation and the susceptibility of Ni-YSZ to graphite deposition when exposed to different carbon containing fuels. The *in situ* spectroscopic data are coupled to results from traditional electrochemical techniques (EIS and LSV) and *ex situ* measurements to understand how different mechanisms and/or material changes either enhance electrochemical performance or lead to overall device degradation. Being able to exclusively identify mechanisms of device degradation provide insight into the development of new SOFC materials and architectures to better enhance performance.

1A. Electrolyte Electronic and Material Characterization

The figures of merit for solid oxide electrolytes include high oxide conductivities, a large resistance to electron conduction, and thermal and chemical stability. A combination of *in situ* Raman electrochemical studies and *ex situ* X-ray absorption experiments have been used to explore if YSZ, at the high operating temperatures required for SOFC operation, might become involved in electrochemical fuel oxidation and surface conduction processes. Initial *in situ* Raman measurements

showed a 50 % reduction in the YSZ F_{2g} peak intensity when exposed to a reducing atmosphere of H_2/Ar. A full recovery of the peak intensity was observed when the YSZ sample was then exposed to an oxidizing atmosphere (O_2/Ar), and this process was found to be reversible. Surface specific EIS measurements were then used to explore the surface conduction of YSZ, on the anode side, under different levels of cell polarization. These lateral EIS measurements exhibited a significant decrease in R_{pol} with an increase in cell overpotential, creating a partially reduced surface that had less resistance towards charge conduction. Concurrent *in situ* Raman measurements showed that the relative oxide concentration in the electrolyte immediately adjacent the anode was being depleted as the fuel cell was being driven at higher cell polarization. *Ex situ* XAS measurements were performed on reduced YSZ samples to explore and understand the extent of these conductive surface states. These measurements revealed that electrons left behind in the unfilled oxide vacancies aided in partially reducing only zirconium and not yttrium in the crystal structure, suggesting that only zirconium plays a role in the formation of surface conduction states.

1B. Alcohol Chemistry in Solid Oxide Fuel Cells

Alcohols have attracted significant interest as fuels for SOFCs due to their ease of storage, relative high energy densities, and active reforming chemistry. Furthermore, methanol can be derived from a variety of sources including biomass, *syn* gas, and methane. Methanol's behavior as a fuel in SOFC operation is not well understood. The oxygen content in the fuel is believed to suppress carbon formation,

but the lower C-O bond dissociation enthalpy makes methanol more reactive increasing the likelihood that methanol can form significant surface carbon.

In this study the behavior of methanol was directly compared to methane by using *in situ* Raman spectroscopy and *in situ* NIR thermal imaging. The data from these measurements were then coupled with simultaneous EIS measurements to gain a better understanding of the changes in electrochemical performance brought upon by prolong exposures and graphite formation from these two different fuels. *In situ* Raman measurements showed that methanol exhibited two distinct graphite growth mechanisms while methane only exhibited one. The first growth mechanism for methanol was slower and similar to that of methane; this mechanism was then followed by a second, more prolific growth mechanism. The first mechanism was associated with the beginning growth of ordered graphite in both fuel species seen at 1560 cm^{-1}. The second more aggressive growth mechanism of carbon from methanol correlated to the appearance of disordered graphite at 1360 cm^{-1}. NIR thermal imaging discovered that the graphite formation is an endothermic processes and the temperature change is proportional to the amount of graphite being formed on the anode surface. This effect was more prominent for methanol ($\Delta T = -5.5 \pm 0.7^{\circ}C$) than for methane ($\Delta T = -0.5 \pm 0.7^{\circ}C$). Real time EIS measurements data correlated with data obtained from the optical methods showed a larger increase in R_{pol} with respect to methanol fuel exposure. The change in R_{pol} was localized in the arcs associated with anode processes showing that graphite formation was interrupting chemistry occurring at these sites.

1C. Reforming of Fuels for Solid Oxide Fuel Cell Operation

Methane's abundance in natural gas and potential to be synthesized from renewable biomass makes it an attractive fuel for SOFC operation. The relatively strong bond strength and chemical stability of methane require that this fuel undergo reforming, either internally or externally, in order for a more favorable fuel mixture to reach the anode and increase the fuel utilization. The experiments explained in this thesis examined the internal oxidative and steam reforming of methane using a variety of analytical techniques. These techniques include the use of *in situ* Raman spectroscopy, real time EIS measurements, voltammetry measurements, and *ex situ* FTIR exhaust measurements.

Voltammetry measurements revealed that there was a sharp potential loss when direct methane was used as a fuel. This region is associated with the energy needed to drive the activation of methane oxidation. A decrease in the magnitude of the OCV was observed when either O_2 or H_2O were introduced as fuel reformers. An increase in this value signifies that the gas mixture reaching the anode is easier oxidized than methane by itself. This effect was dependent on the reformer concentration. *Ex situ* FTIR measurements were used to examine the chemical composition of the direct, oxidative reformed and steam reformed gas mixtures acting on the anode. Oxidative reformed methane was comprised of a mixture of CO and CO_2, while IR spectra of steam reformed methane showed only CO (and residual CH_4). (Each mixture also presumably included H_2 although this species could not be detected.)

A combination of *in situ* vibrational Raman spectroscopy and real time impedance measurements have been used simultaneously to correlate changes observed in the electrochemical performance to real time material and chemical changes occurring at the anode. When direct methane was used, *in situ* Raman measurements showed that graphite was forming aggressively on the anode surface. Correlated with Raman measurement, EIS measurements showed a significant increase in R_{pol} with respect to fuel exposure time and again these changes were localized in the arcs associated with anode processes. Oxidative and steam reforming of methane were shown to completely suppress carbon formation thereby minimizing degradation of electrochemical performance due to carbon formation.

Ethanol has been considered as a fuel for SOFC operation based on its potential to be a renewable fuel derived from agricultural processes. The C-C bond in ethanol has been known pyrolyze into fuel species such as ethylene and acetylene that can lead to rapid nucleation of graphite growth. To limit these precursors, reforming is needed to produce a favorable gas mixture of CO and H_2 and to suppress the formation of graphitic precursors. The experiments performed in this thesis investigated the effects of steam reforming ethanol compared to dry ethanol on SOFC operation. Initial FTIR exhaust measurements revealed that a dry ethanol fuel feed underwent pyrolysis to form a gas mixture of CO, CO_2, CH_4, and C_2H_2. Introduction of H_2O into the ethanol fuel feed limited the formation of C_2H_2, CH_4 and other species known to form graphite formation on the Ni-YSZ anode. In the *in situ* Raman measurements, humidified ethanol led to rapid growth of graphitic carbon when the cell was held at OCV, but polarizing the device slowed the rate of graphite growth

and sufficiently high overpotentials suppressed graphite growth completely. EIS measurements showed that rapid carbon growth was accompanied by significantly diminished performance, although this effect was much less noticeable in polarized cells, even when Raman data showed the clear presence of carbon deposits. Dry ethanol feeds led to instantaneous graphite formation and rapid growth kinetics, regardless of cell polarization. This effect also manifested itself in the EIS measurements with an increase in the EIS arcs associated with anode processes.

2. Future Directions

2A. UV-Raman Solid Oxide Fuel Cell Assembly

Currently the 488 nm Ar ion laser used in our *in situ* Raman assembly lessens but does not eliminate the contribution of the blackbody radiation to the experimentally observed background. This background often appears in spectra as a rising baseline at larger Raman shifts (or corresponding longer wavelengths relative to the incident 488 nm.) Blackbody radiation limits the sensitivity of our instrument and compromises our ability to identify low concentration, steady state intermediates that form during electrochemical fuel oxidation.

To eliminate the effects of blackbody radiation experiments must be performed using shorter wavelength excitation sources. A UV laser excitation source of 244 nm can reduce, by orders of magnitude, the contribution of blackbody radiation to experimental data. Furthermore, the intrinsic frequency dependence of non-resonant Raman scattering also predicts that using 244 nm rather than 488 nm to excite will increase signal intensity by a factor of 20-fold further improving

instrument sensitivity. The Walker Research Group will soon be installing a new UV-microscope and begin testing these predictions.

2B. Quantitative Chronopotentiometry Measurements

Our current research efforts have only allowed us to compare *relative* amounts of graphite being formed on the anode surface from hydrocarbon fuels. This relative quantity is based on the observed signal intensity in the Raman feature assigned to graphite. These measurements have not been used to quantify exactly how much graphite is actually forming throughout the entire anode during operation. *Ex situ* thermogravimetric analysis have been used to determine exactly how much graphite is on the anode, but these measurements can only be performed after the device has been completely cooled down and disassembled.

Initial *in situ* experiments in our lab have shown the changes that occur in graphite when it is used as a fuel in SOFC operation. Once graphite is formed on a Ni/YSZ anode from 1.5 L of direct methane, the fuel is turn off and allowed to evacuate the assembly while argon creates an inert environment that preserves the graphite that has formed through out the Ni/YSZ cermet anode. Having the inert atmosphere, above the anode, allows for the experiment to focus on solid carbon acting as the fuel with out the presence of any residual CH_4. Once all the fuel has been evacuated a constant current (~ 28.4 mA corresponding roughly to a cell overpotential of ~ 0.80 V) was applied to the SOFC and the resulting voltage was monitored. Simultaneously, we measure the *relative* amount of graphite remaining using the *in situ* Raman assembly.

While graphite is acting as the fuel the voltage will be negative. When the graphite fuel is being consumed, there will be a steady increase in potential approaching 0.0 V, symbolizing that the fuel is being consumed without being replenished. The steady increase in potential to 0.0 V is provided by the potentiostat to maintain the constant applied current. Once the fuel is fully consumed, the potentiostat will take control of the voltage, once again to maintain the applied current. This number will be dependent on the overpotential that was used to maintain the applied current, in our case it was ~ 0.80 V. This change in voltage was *directly* correlated to *in situ* Raman measurements monitoring the disappearance of graphite on the anode surface. It was noticed in our measurements that the longer we applied this constant current there was an additional increase in the voltage that was applied. In situ Raman measurements directly correlated this increase to the formation of NiO from the Ni catalysts in the anode. Converting the metal catalyst to an insulating metal oxide will increase the resistance to conducting a current across the anode. Using Ohm's Law the voltage will need to simultaneously increase to maintain the constant applied current.

Knowing the current drawn and the time elapsed (C), we can calculate the number of oxides that passed through the circuit, with Faraday's constant, and therefore the amount of carbon that was oxidized if we assume Eq. 1 to be factual.

$$C_{(ads)} + 2O^{2-}{}_{(YSZ)} \rightarrow CO_{2(g)} + 4e^{-} \qquad \textbf{(Eq. 1)}$$

There will be some error associated with this measurement, due impart to the possibility of CO being produced and expelled from the SOFC before it can be oxidized into CO_2. This technique can be perfected by combining it with

simultaneous FTIR exhaust measurements and/or gas chromatograph-mass spectroscopy (GCMS) measurements. These measurements can be used to verify if CO is actually being expelled from the SOFC and if so a more accurate quantity for graphite can be calculated by now including the amount of CO that was expelled found by GCMS measurements. The ability to observe how much graphite is forming during operation is beneficial in understanding fuel utilization efficiencies and mechanisms responsible for electrochemical oxidation. Initial experiments exploring this technique can be seen in Appendix IV.

2C. Electrode-Supported Solid Oxide Fuel Cells

The MEAs utilized in the experiments described in this thesis are electrolyte supported SOFCs. These systems are used due in part to the durability of a thick electrolyte. The drawbacks to using these thick electrolytes are lower current and power densities relative to anode or cathode supported cells. The thickness of our electrodes (~ 30 μm) and penetration depth of our Raman laser also prevents us from observing chemistry occurring at the active TPB, where the majority of the electrochemical fuel oxidation and oxygen reduction is taking place. When using electrode supported MEAs the electrolyte can be as thin as ~ 10 μm. At this thickness, the YSZ electrolyte becomes transparent to incident excitation and allows for the possibility of allowing the Raman laser to pass through and probe either the anode or cathode TPB. This geometry may prove to be extremely beneficial to our research efforts because experiments will provide direct, unambiguous evidence of the roles played by YSZ and each electrode in fuel oxidation and oxygen reduction

specifically at the TPB. Initial experiments using commercial anode-supported cells can be seen in Appendix V.

Appendix I: Optically Accessible Solid Oxide Fuel Cell Assembly

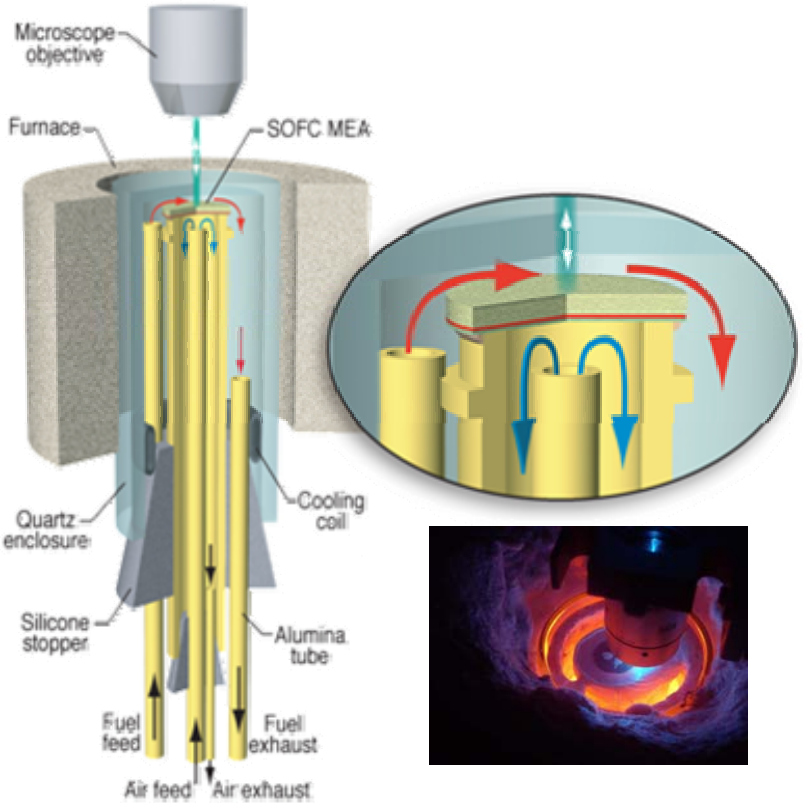

Optically accessible SOFC set up: Schematic of operational system created by Robert Kee, Colorado School of Mines. Inset is a photo taken of the actual anode surfaces and optics, looking through the top of an operational system. Bottom picture

shows the path that the Raman laser takes to measure chemistry occurring on SOFC surfaces. The back-scattered photons also travel back up the same path to go to the CCD detector.

The fuel cell rig used in chapters II-VI is shows above. This system is comprised of a main alumina tube (Omega) that the sample is pasted atop of with alumina paste. Other alumina tubes are attached to the main tube to direct fuel (H_2, hydrocarbons) and oxidant (air, O_2) to the anode and cathode, respectively. Alumina tubes are also used to exhaust cathode and anode gases away from the furnace. A silicone stopper (McMaster Carr) is used to create a seal with the inside fuel cell set up with the surrounding quartz tube (Quark Glass) to prevent fuel from leaking out into the furnace. The temperature rating of this silicone stopper is 600˚C. To prolong the life of the silicone stopper and maintain the seal, a coolant coil is used to cool the area where the seal is created to maintain the temperature of the silicone stopper. The quartz tube serves an additional role by having a smooth optical bottom that allows for light to enter in while allowing back-scattered light to exit the assembly to conduct the *in situ* Raman measurements. This whole system is then surrounded by a split tube furnace (Thermcraft) that heats the center of the apparatus to 1000˚C. The thermal gradient created by exposing the top of the furnace to air allows for the SOFC to reach temperatures ≤ 715˚C. Custom built optics are used to move the microscope objective (Lieca) in and out of the assembly as to focus the laser. This whole system is then attached to a XYZ translational stage to allow for testing of various spots on the SOFC surfaces.

Appendix II: Temperature Dependence on YSZ F_{2g} Peak Migration

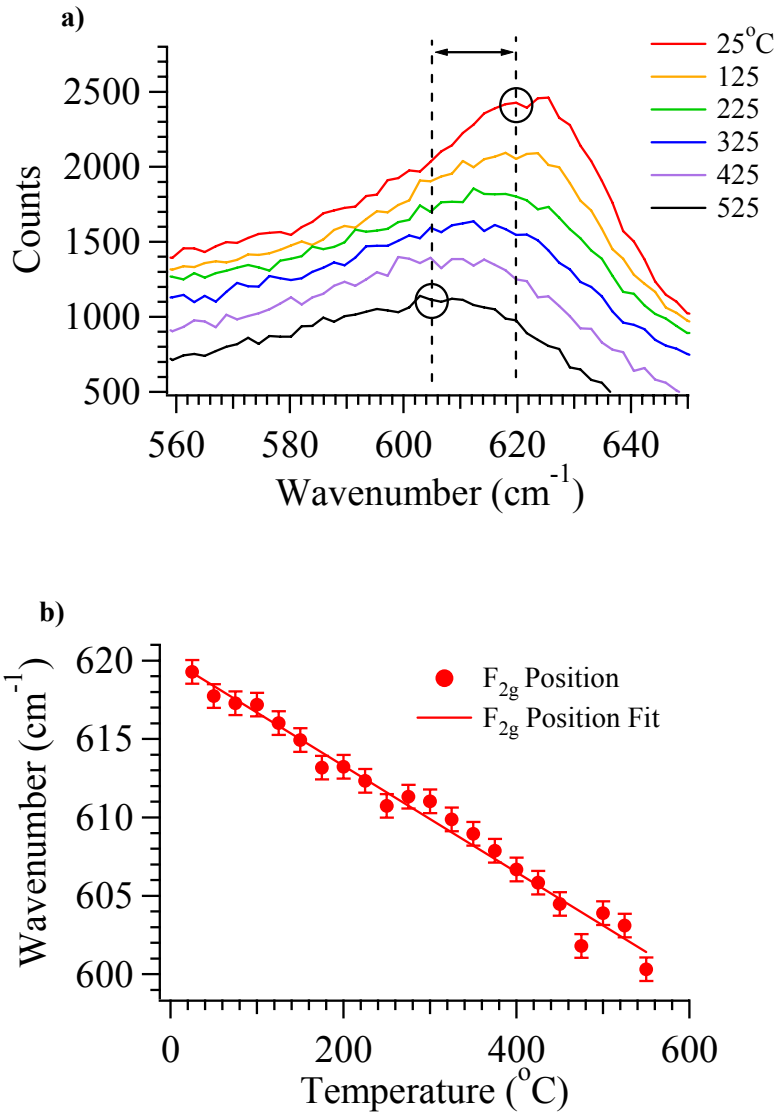

The above Figures exhibit how YSZ F_{2g} peak position is dependent on the surrounding temperature that the sample is experiencing. Figure a) shows actual spectra taken on the YSZ electrolyte as temperature is being increase, for clarity spectra are only shown for every 100˚C. This shift of ~ 15 cm^{-1} is highlighted in

Figure a) with dashed lines. Figure b) monitors the position of the YSZ F_{2g} peak with respect to temperature. This peak position migration exhibits a linear dependence on temperature. This is especially important for our experiments because we now have a technique that can accurately measure surface temperature and eliminates the need for a thermocouple. A thermocouple can accurately measure temperature above the sample, but using YSZ's peak position will provide a more accurate surface temperature and this is important because this is where our *in situ* Raman measurements will take place, *at the surface*.

Appendix III: Co-author Contributions

Chapters II through VI are all modified versions of manuscripts that have either appeared in press, have been submitted for peer-review, or are in preparation for submission and appear as such. Some of the information presented in chapter III and IV are through collaborative efforts with co-authors. The contributions of co-authors are explained below.

Chapter III. This chapter focused on observing the changes in vibrational and electronic structure of either surface reduced or oxidized YSZ samples. Martin Finsterbusch, a student at Montana State University in the Physics Department, performed all the XAS measurements presented in Chapter III of this thesis. This work provided a great insight into the species in the YSZ crystal structure (Zr) that are responsible for the formation of conductive surface states in reduced YSZ. The other co-author on this journal article is Professor Yves Idzerda who is the principle invesigator for Martin's XAS measurements as well as his advisor.

Chapter IV. This chapter explored the electrochemical fuel oxidation and anode degradation mechanisms associated with either a direct methane of methanol fuel feed. The analytical methods that were used in this chapter were *in situ* Raman, *in situ* NIR thermal imaging, real time impedance, *ex situ* FTIR exhaust. The NIR thermal imaging technique was created at the Naval Research Laboratory. Collaborative efforts allowed for this unique measurement technique to be used on our optically accessible SOFC assembly present in Appendix I. The researchers that conducted these measurements were Dr. Michael Pomfret and Dr. Daniel Steinhurst.

This technique was very informative and showed to compliment the *in situ* Raman and real time EIS measurements. At the small period of time that these experiments took place I was in transition to Montana State University with my advisor Professor Robert Walker. Because of this Dr. Pomfret and Dr. Steinhurst also performed the *ex situ* FTIR exhaust measurements presented in chapter IV. The rest of the FTIR exhaust measurements presented in other chapters were conducted by the author of this thesis.

Chapters II-VI. Since these chapters are modified manuscripts the other co-author on them is the author's research advisor, Professor Robert A. Walker. Professor Walker is the principle investigator of the research project presented in these chapters and therefore advised on all of the experiments.

Appendix IV: Quantitative Chronopotentiometry Measurements

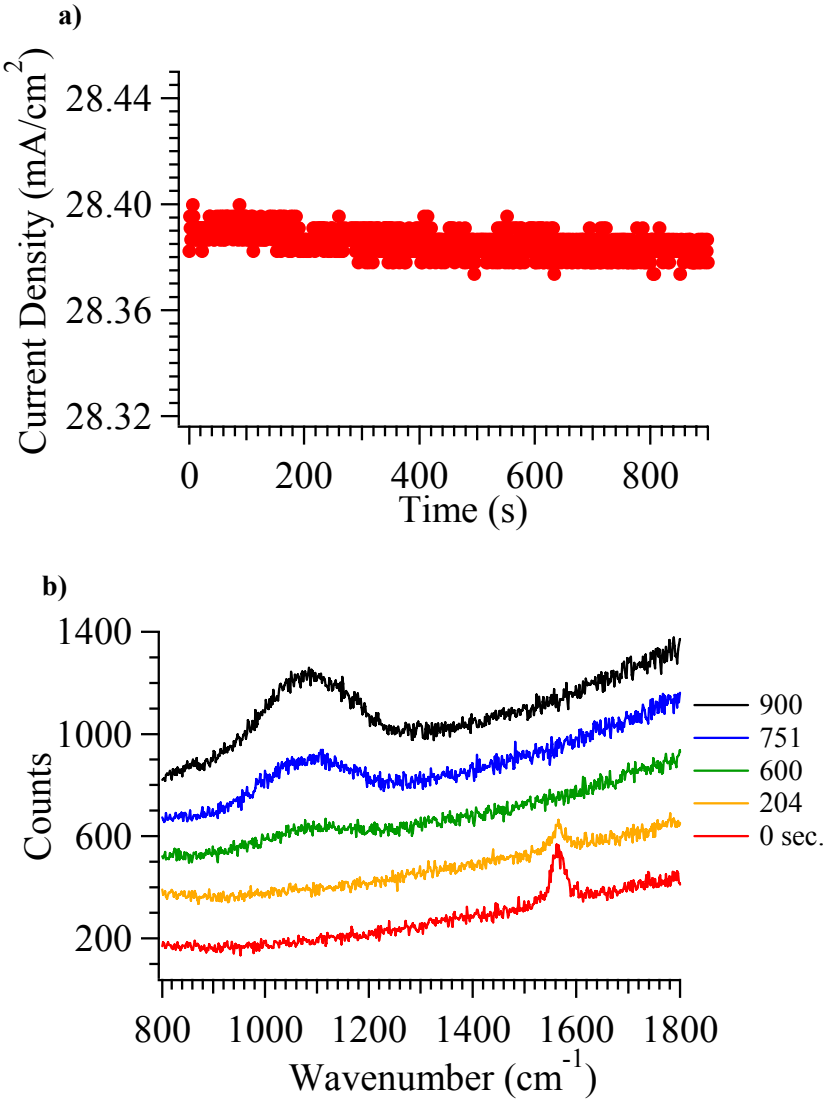

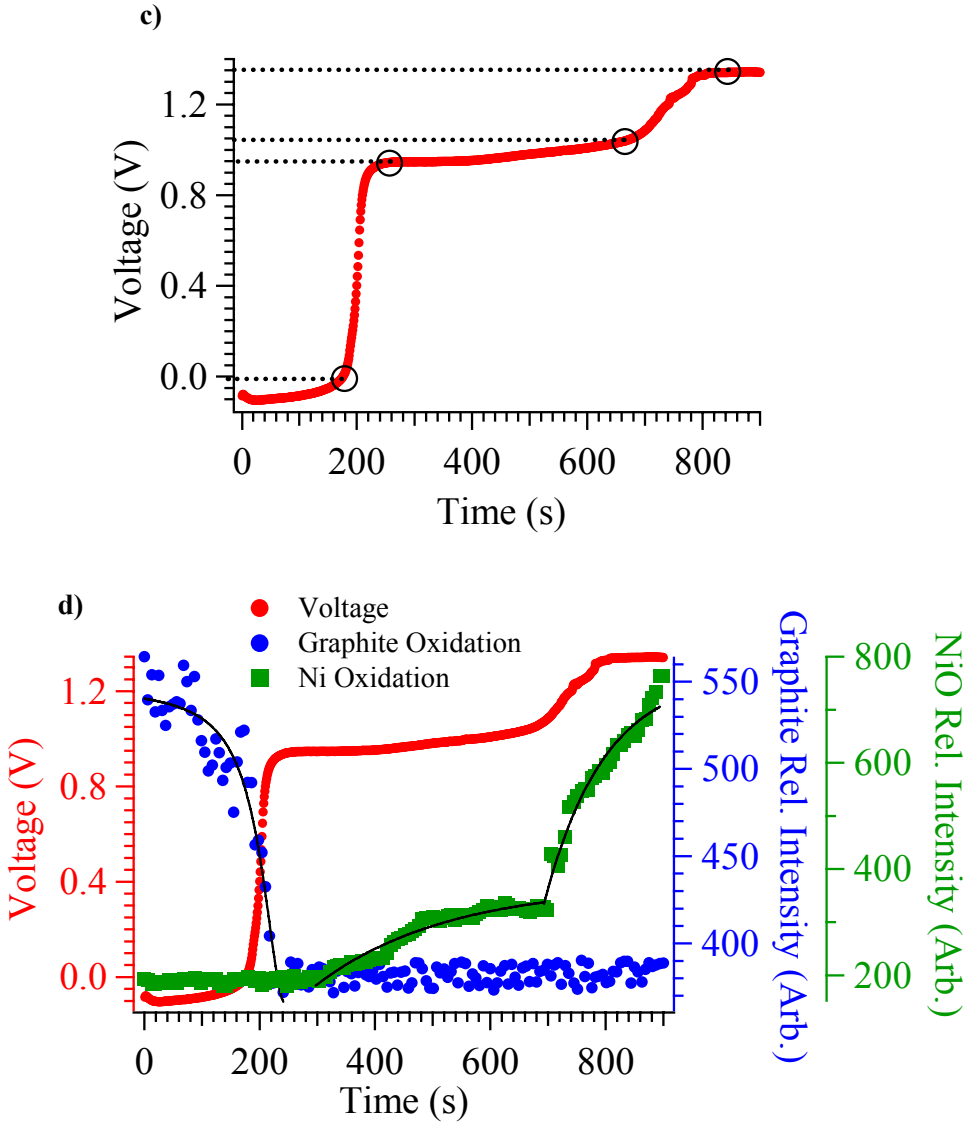

The Figures presented above represent a possible future direction of the Walker Research Group to further explore SOFC chemistry and directly correlate *in situ* Raman measurements with real time electrochemical measurements. Raman spectroscopy is only capable of providing *relative* amounts of species forming on SOFC surfaces, with especial focus on graphite formation on SOFC anodes. Our current technique of using *in situ* Raman spectroscopy is only limited to probing the anode surface and not the three phase boundary where majority of the fuel oxidation

mechanism are occurring. What is unknown is exactly how much graphite is forming based on how much fuel was utilized. *Ex situ* thermogravimetric analysis can be performed where the carbon deposits are burned off and the difference in the weight of the sample can provide the amount of graphite that was burned off. These measurements although helpful can only be conducted after the cell has been cooled down and disassembled. It would be beneficial to be able to measure the amount of graphite in situ and in real time when the device is operating.

The above Figures begin to approach using this technique. Here 1.5 L of methane is introduced in the fuel cell and allowed to form graphite deposits at open circuit voltage. Residual fuel products are cleared out of the SOFC with argon to ensure that solid carbon deposits are acting as the fuel to be electrochemically oxidized into CO_2. Current density is then drawn from the cell as shown in Figure a) with a current value of ~ 28.4 mA/cm^2. The area of our anode is 1.41 cm^2 and by multiplying this number with the current density we obtain the actual applied current, ~ 40 mA. Using *in situ* Raman measurements we can monitor the graphite being consumed as a fuel by the anode with respect to time, Figure b). We also start seeing the appearance of NiO resulting from the increase in oxide flux. Some interesting findings arise in Figure c) exhibiting the presence of five distinct voltages and four distinct changes in voltage as a constant current is being drawn.

To gain a better understanding of these observed changes in voltage, concurrent *in situ* Raman measurements were taken, as seen in Figure d). overlapping this data reveals that the first change in voltage (0.0V) is associated with the depletion of graphite or the fuel and how it is no long able to sustain the reaction.

The abrupt change in voltage to a ~ 0.90 V is attributed to the instrument taking control of the voltage in order to maintain the constant current. A slow yet steady increase in voltage is occurring next, if we correlated this with the Raman measurements we can attribute this to a slow initial growth of NiO. The final change observed is another abrupt change in voltage to ~ 1.3 V. Once again correlating this to Raman measurements show that at this time there is a more aggressive growth of NiO. And since we are converting our electronic conducting metal catalyst to an insulating metal oxide, the corresponding voltage will need to also be increased to maintain the constant current.

Knowing the amount of current being drawn and the amount of time it took for the fuel to be fully consumed, we found that it took 80 coulombs (C) to deplete the fuel source (graphite). If we multiply this term by Faradays constant (96485.3399 $C \cdot mol^{-1}$) we can then obtain the moles of electrons (8.29×10^{-4} mol) that passed though the circuit in 200 sec. Each oxide anion used to oxidize graphite has two electrons making the oxide anion molar value 4.15×10^{-4} mol. If we believe Eq. 1 in Chapter VII to be true, then our amount of moles for graphite formations through out the anode is 2.07×10^{-4} mol. This results in a total mass of 2.49 mg of graphitic deposits that were created by 1.5 L of methane fuel throughout the Ni/YSZ anode. As stated in Chapter VII there will be some uncertainty associated with this approximation, so further FTIR and GC/MS exhaust measurements would be needed to eliminate this uncertainty.

Appendix V: Electrode-Supported Solid Oxide Fuel Cells

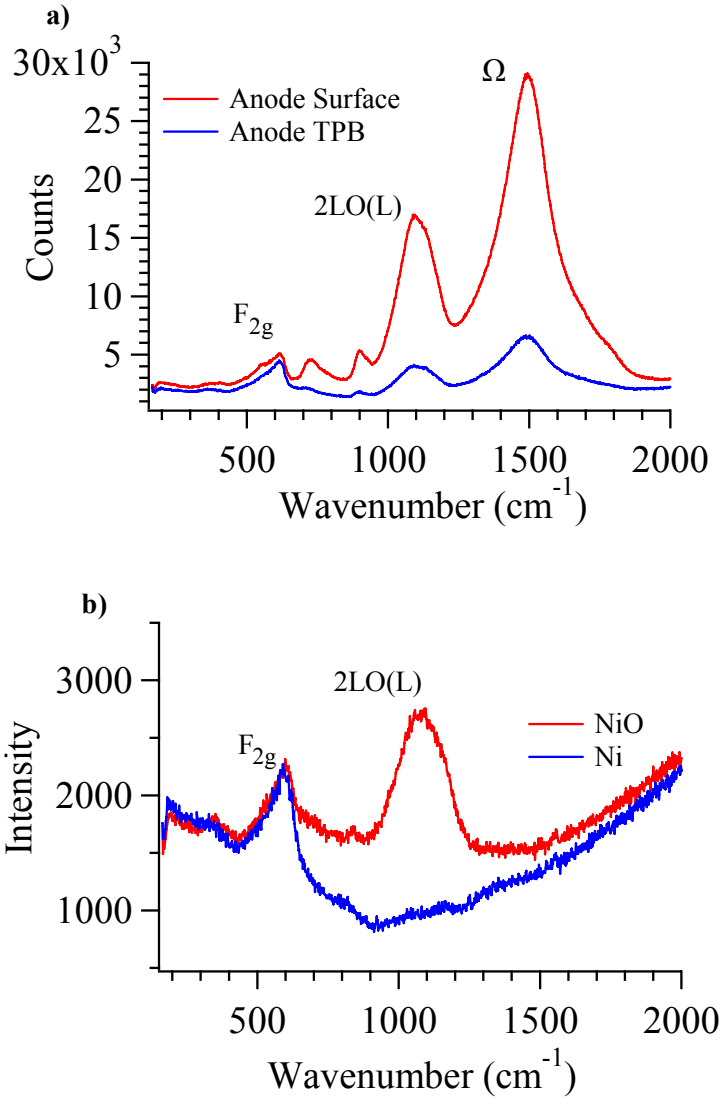

The above Figures represent initial experiments conducted with anode-supported cells SOFCs (Virkar). The ability to decrease the thickness of the electrolyte from 0.80 mm (electrolyte-supported) to 10 μm affords us the opportunity to not only increase our cell performance but also to be able to probe and gain insight in to the reactions and mechanisms occurring at the TPB of these cells. In the above Figures we wanted to observe first if it was possible to look at the anode through the

thin electrolyte first at room temperature, Figure a). It is observed that Raman spectra taken on the anode side are exceptionally intense and shows the presence of the two NiO magnon peaks and the YSZ F_{2g} peak. When we tested the SOFC from the cathode side and through the thin electrolyte we see the presence of the same peaks but just smaller intensitites. Now that we know that we can probe the TPB we wanted to test these SOFCs in our optically accessible SOFC assembly with the cathode side exposed to investigation with Raman spectroscopy, Figure b). If we position our laser spot just off the cathode and onto the YSZ surface we see the appearance of NiO. At high temperatures the temperature dependent NiO Ω peak diminishes and migrate under the temperature independent NiO 2LO peak. When we apply a mixture of H_2/Ar to the anode side we see that the NiO peak diminishes confirming that it is possible to observe reactions happening at the reactive TPB. Further advancement in cathode design would be needed to create a patterned electrode so it would be possible to focus on the cathode while simultaneously observing reactions taking place at the TPB where the electrodes overlap.

References

(1) Appleby, A. *J. Power Sources*, **1996**, *69*, 153.

(2) Assabumrungrat, S.; Sangtonkitcharoen, W.; Laosiripojana, N.; Arpornwichanop, A.; Charojrochkul, S.; Praserthdam, P. *J. Power Sources*, **2005**, *148*, 18.

(3) Atkinson, A.; Barnett, S.; Gorte, R.; Irvine, J.; Mcevoy, A.; Mogenson, M.; Singhal, S.; Vohs, J. *Nat. Mat.*, **2004**, *3*, 17.

(4) Bard, A.; Faulkner, L., *Electrochemical Methods: Fundamentals and Applications*, ISBN 978-0-471-04372-0, John Wiley & Sons

(5) Bebelis, S.; Neophytides, S. *Solid State Ionics*, **2002**, *152-153*, 447.

(6) Bedringas, K.; Ertesvag, I.; Byggstoyl, S.; Magnussen, B. *Energy*, **1997**, *22*, 403.

(7) Bessler, W. *Solid State Ionics*, **2005**, *176*, 997.

(8) Bieberle, A.; Gauckler, L. *Solid State Ionics*, **2000**, *135*, 337.

(9) Bieberle, A.; Meier, L.; Gauckler, L. *Solid State Ionics*, **2002**, *146*, 23.

(10) Bieberle, A; Meier, L.; Gauckler, L. *J. Electrochem. Soc.*, **2001**, *148*, A646.

(11) Blanksby, S.; Ellison, B. *Acc. Chem. Res.*, **2003**, *36*, 255.

(12) Bove, R.; Ubertini, S.; *J. Power Sources*, **2006**, *159*, 543.

(13) Brett, D.; Atkinson, A.; Cumming, D.; Rameriz-Cabrera, E.; Rudkin, R.; Brandon, N. *Chem. Eng. Sci.*, **2005**, *60*, 5649.

(14) Brett, D.; Atkinson, A.; Brandon, N.; Skinner, S. *Chem. Soc. Rev.*, **2008**, *37*, 1568.

(15) Cimenti, M.; Alzate-Restrepo, V.; Hill, J. *J. Power Sources*, **2010**, *195*, 4002.

(16) Cimenti, M.; Biriss, V.; Hill, J. *Fuel Cells*, **2007**, *5*, 377.

(17) Cimenti, M.; Hill, J. *Energies*, **2009**, *2*, 377.

(18) Cimenti, M.; Hill, J. *J. Power Sources*, **2009**, *186*, 377.

(19) Cimenti, M.; Hill, J. *J. Power Sources*, **2010**, *195*, 3996.

(20) Cimenti, M.; Hill, J. *J. Power Sources*, **2010**, *195*, 54.

(21) Cocco, D.; Tola, V. *J. Eng. Gas Turbines Power*, **2007**, *129*, 478.

(22) Coutelieris, F.; Douvartzides, S.; Tsiakaras, P. *J. Power Sources*, **2003**, *123*, 200.

(23) Decaluwe, S.; Zhu, H.; Kee, R.; Jackson, G. *J. Electrochem. Soc.*, **2008**, *155*, B538.

(24) Devanathan, R.; Weber, W.; Singhal, S.; Gale, J. *Solid State Ionics*, **2006**, *177*, 1251.

(25) Dokmaingam, P; Assabumrungrat, S.; Soottitantawat, A.; Laosiripojana, N. *J. Power Sources*, **2010**, *171*, 69.

(26) Douvartzides, S.; Coutelieris, F.; Demin, K.; Tsiakaras, P. *AlChE J.*, **2003**, *49*, 248.

(27) Eder, D.; Kramer, R. *Phys. Chem. Chem. Phys.*, **2002**, *4*, 795.

(28) Eigenbrodt, B.; Pomfret, M.; Steinhurst, D.; Owrutsky, J.; Walker, R. *J. Phys. Chem. C.*, **2011**, *115*, 2895.

(29) Erning, J.; Hauber, T.; Stimming, U. Wippermann, K. *J. Power Sources*, **1996,** *61***,** 205.

(30) Faungnawakij, K.; Kikuchi, R.; Eguchi, K. *J. Power Sources*, **2007**, *164*, 73.

(31) Feinberg, A.; Perry, C. *J. Phys. Chem. Solids*, **1981**, *42*, 513.

(32) Feng, B.; Wang, C.; Zhu, B. *Electrochem. Solid State Lett.*, **2006**, *9*, A80.

(33) Finnerty, C.; Coe, N.; Cunningham, R.; Ormerod, R. *Catal. Today*, **1998**, *46*, 137.

(34) Finnerty, C.; Tompsett, G.; Kendall, K.; Ormerod, R. *J. Power Sources*, **2000**, *86*, 459.

(35) Fouquet, D.; Muller, A.; Weber, A.; Ivers-Tiffte, E. *Ionics*, **2003**, *9*, 103.

(36) Frazer, B. *Surf. Sci.*, **2003**, *537*, 161.

(37) Fu, Q.; Mi, S.; Wessel, E.; Tietz, F. *J. Eur. Cerm. Soc.*, **2008**, *28*, 811.

(38) Funkunaga, H.; Ihara, M.; Sakaki, K.; Yamada, K. *Solid State Ionics*, **1996**, *86-88*, 1179.

(39) Goodenough, J. *Annu. Rev. Mater. Res.*, **2003**, *33*, 91.

(40) Gorte, R.; Kim, H.; Vohs, J. *J. Power Sources*, **2002**, *106*, 10.

(41) Gorte, R.; Park, S.; Vohs, J.; Wang, C. *Adv. Mater.*, **2000**, *12*, 1465.

(42) Goula, G.; Kiousis, V.; Nalbandian, L.; Yentekakis, I. *Solid State Ionics*, **2006**, *177*, 2119.

(43) Guo, X. *Solid State Ionics*, **1995**, *81*, 235.

(44) Gupta, G.; Dean, A.; Ahn, K.; Gorte, R. *J. Power Sources*, **2006**, *158*, 497.

(45) Gupta, G.; Hecht, E.; Zhu, H.; Dean, A.; Kee, R. *J. Power Sources*, **2006**, *156*, 434.

(46) Haering, C.; Roosen, A.; Schichl, H. *Solid State Ionics*, **2005**, *176*, 253.

(47) Harris, D.; Bertolucci, M., *Symmetry and Spectroscopy: An Introduction to Vibrational and Electronic Spectroscopy*, ISBN 0-486-66144-X, Dover Publications.

(48) Hassel, B.; Boukamp, B.; Burggraaf, A. *Solid State Ionics*, **1992**, *53-56*, 890.

(49) Hattori, M.; Takeda, Y.; Lee, J.; Ohara, S.; Mukai, K.; Fukui, T.; Takahashi, S.; Sakaki, Y.; Nakanishi, A. *J. Power Sources*, **2004**, *131*, 247.

(50) Hattori, M.; Takeda, Y.;Sakaki, Y.; Nakanishi, A.; Ohara, S.; Mukai, K.; Lee, J.; Fukui, T. *J. Power Sources*, **2004**, *126*, 23.

(51) Hirabayashi, D.; Tomita, A.; Brito, M.; Hibino, T.; Harada, U.; Nagao, M.; Sano, M. *Solid State Ionics*, **2004**, *168*, 23.

(52) Hirabayashi, D; Hasimoto, A.; Hibino, T.; Harda, U.; Sano, M. *Electrochem. Solid State Lett.*, **2004**, *7*, A108.

(53) Hirschenhofer, J. *IEEE AES Systems Magazine*, **1997**, *12*, 23.

(54) Hofmann, P.; Panopoulos, K. *J. Power Sources*, **2010**, *195*, 5320.

(55) Hofmann, P.; Panopoulos, K. *J. Power Sources*, **2010**, *195*, 5320.

(56) Holtappels, P.; De Haart, L.; Stimming, U.; Vinke, I.; Mogensen, M. *J. Appl. Electrochem.*, **1999**, *29*, 561.

(57) http://webook.nist.gov, NIST Standard Reference Database, Quantitative Infrared Database.

(58) Huayang, Z.; Kee, R.; Janardhanan, V.; Duetschmann, D.; Goodwin, D. *J. Electrochem. Soc.*, **2005**, *152*, A2427.

(59) Hui, S.; Petric, A. *J. Electrochem. Soc.*, **2002**, *149*, J1.

(60) Ihara, M.; Hasegawa, S. *J. Electrochem. Soc.*, **2006**, *153*, A1544.

(61) Iida, T.; kawano, M.; Matsui, T.; Kikuchi, R.; Eguchi, K. *J. Electrochem. Soc.*, **2007**, *154*, B234.

(62) Ingle, J.; Crouch, S., *Spectrochemical Analysis*, ISBN 0-13-826876-2, Prentice-Hall

(63) Ishihara, T.; Hiei, Y.; Takita, Y. *Solid State Ionics*, **1995**, *79*, 371.

(64) Ishihara, T: Yan, J.; Shinagawa, M.; Matsumoto, H. *Electrochim. Acta.*, **2006**, *52*, 1645.

(65) Jablonski, A.; Powell, C. *J. Electron. Spectrosc. Relat. Phenom.*, **1999**, *100*, 137.

(66) Jablonski, A.; Powell, C. *Surf. Sci.*, **2005**, *551*, 106.

(67) Jacobson, M.; Colella, W.; Golden, D. *Science*, **2005**, *308*, 1901.

(68) Janardhanan, V.; Heuveline, Deutschmann, O. *J. Power Sources*, **2008**, *178*, 368.

(69) Jiang, S.; Chan, S. *J. Mater. Sci.*, **2004**, *39*, 4405.

(70) Jiang, S.; Love, J.; Badwal, S. *Electrical Properties of Oxide Materials*, **1997**, *125*, 81.

(71) Jiang, Y.; Virkar, A. *J. Electrochem. Soc.*, **2001**, *148*, A706.

(72) Kakac, S.; Pramuanjaroenkij, A.; Zhou, X. *Int. J. Hydrogen Energy*, **2007**, *32*, 761.

(73) Kee, R. Zhu, H.; Goodwin, D. *Proc. Combust. Inst.*, **2005**, *20*, 2379.

(74) Kendall, K. *Int. Mater. Rev.*, **2005**, *50*, 257.

(75) Kenney, B.; Valdmanis, M.; Baker, C.; Pharoah, J.; Karan, K. *J. Power Sources*, **2009**, *189*, 1051.

(76) Kim, T.; Ahn, K.; Vohs, J.; Gorte, R. *J. Power Sources*, **2007**, *164*, 42.

(77) Laosiripojana, N.; Assabumrungrat, S. *J. Power Sources*, **2007**, *163*, 943.

(78) Laurencin, J.; Delette, G.; Sicardy, O.; Rosini, S.; Lefebvre-Joud, F. *J. Power Sources*, **2010**, *195*, 2747.

(79) Lee, J.; Yoon, S.; Kim, B.; Kim, J.; Lee, H.; Song, H. *Solid State Ionics*, **1997**, *144*, 175.

(80) Levy, M.; Fouletier, J.; Kleitz, M. *J. Electrochem. Soc.*, **1988**, *135*, 1584.

(81) Li, Y.; He, D.; Zhu, Q.; Zhang, X.; Xu, B. *J. Catal.*, **2004**, *221*, 584.

(82) Lin, Y.; Barnett, S. *Solid State Ionics*, **2008**, *179*, 420.

(83) Lin, Y.; Zhan, Z.; Liu, J.; Barnett, S. *Solid State Ionics*, **2005**, *176*, 1827.

(84) Liu, D.; Krumpelt, M.; Chien, H.; Sheen, S. *J. Mater. Eng. Perform.*, **2006**, *15*, 442.

(85) Liu, J. *Prog. Chem.*, **2006**, *18*, 1026.

(86) Liu, M.; Peng, R.; Dond, D.; Gao, J.; Liu, X.; Meng, G. *J. Power Sources*, **2008**, *185*, 188.

(87) Lui, D.; Perry, C.; Ingel, R. *J. Appl. Phys.*, **1988**, *64*, 1413.

(88) Macek, J.; Novosel, B.; Marinnsek, M. *J. Eur. Ceram. Soc.*, **2007**, *27*, 487.

(89) Mandin, P.; Bernay, C.; Tran-Dac, S.; Broto, A.; Abes, D.; Cassir, M. *Fuel Cells*, **2006**, *6*, 71.

(90) Manning, P.; Sirman, J.; Souza, R.; Kilner, J. *Solid State Ionics*, **1997**, *100*, 1.

(91) Martinez, A.; Brouwer, J. *J. Power Sources*, **2010**, *195*, 7268.

(92) Mat, M.; Liu, X.; Zhu, Z.; Zhu, B. *Int. J. Hydrogen Energy*, **2007**, *32*, 796.

(93) Matheu, D.; Dean, A.; Grenda, J.; Grean, W. *J. Phys. Chem. A*, **2003**, *107*, 8552.

(94) McCreery, R., *Raman Spectroscopy for Chemical Analysis*, ISBN 0471252875, John Wiley & Sons

(95) McIntosh, S.; Gorte, R. *J. Chem. Rev.*, **2004**, *104*, 4845.

(96) McIntosh, S.; He, H.; Lee, S.; Costa-Nunes, O.; Krishnan, V.; Vohs, J.; Gorte, R. *J. Electrochem. Soc.*, **2004**, *151*, A604.

(97) McIntosh, S.; Vohs, J.; Gorte, R. *J. Electrochem. Soc.*, **2003**, *150*, A470.

(98) Mertens, J.; Haanappel, V.; Tropartz, C.; Herzhof, W.; Buchkremer, H. *J. Fuel Cell Sci. Tech.*, **2006**, *3*, 125.

(99) Minh, N. *Solid State Ionics*, **2004**, *174*, 271.

(100) Mizusaki, J.; Tagawa, H.; Saito, T.; Kamitani, K.; Yamamura, T.; Hirano, K.; Ehara, S.; Takagi, T.; Hikita, T.; Ippomatsu, M.; Nakagawa, S.; Hashimoto, K. *J. Electrochem. Soc.*, **1994**, *141,* 2129.

(101) Mogensen, M.; Kammer, K. *Annual Rev. Mater. Res.*, **2003**, *33*, 321.

(102) Muradov, N. *Energy & Fuels*, **1998**, *12*, 41.

(103) Murray, E.; Tsai, T.; Barnett, S. *Nature*, **1999**, *400*, 649.

(104) Nabae, Y.; Yamanaka, I.; Hatano, M.; Otsuka, K. *J. Electrochem. Soc.*, **2006**, *153*, A140.

(105) Nagle, D.; PaiVerneker, V.; Petelin, A.; Groff, G. *Mat. Res. Bull.*, **1989**, *24*, 619.

(106) Nakajima, R.; Stohr, J.; Idzerda, Y. *Phys. Rev. B*, **1999**, *59*, 6421.

(107) Nam, J.; Jeon, D. *Electrochim, Acta*, **2006**, *51*, 3446.

(108) Nesaraj, A.: Kumar, M.; Raj, I.; radhakrishna, I.; Pattabiraman, R. *Iranian Chem. Soc.*, **2007**, *4*, 89.

(109) Nielsen, J.; Jocobsen, T. *Solid State Ionics*, **2008**, *178*, 1769.

(110) Nikooyeh, K.; Jeje, A.; Hill, J. *J. Power Sources*, **2007**, *171*, 601.

(111) Norinaga, K.; Dutschmann, O. *Ind. Eng. Chem. Res.*, **2007**, *46*, 3547.

(112) Ormerod, R. *Chem. Soc. Rev.*, **2003**, *32*, 17.

(113) Perry, C.; Fienberg, A. *Solid State Commun*, **1980**, *36*, 519.

(114) Perry, C.; Fienberg, A.; Currat, R. *Bull. Amer. Phys. Soc.*, **1981**, *26*, 405.

(115) Pillai, M.; Lin, Y.; Zhu, H.; Kee, R.; Barnett, S. *J. Power Sources*, **2010**, *195*, 271.

(116) Pomfret, M.; Demircan, O.; Sukeshini, A.; Walker, R. *Environ. Sci. Technol.*, **2006**, *40*, 5574.

(117) Pomfret, M.; Marda, J.; Jackson, G.; Eichhorn, B.; Dean, A.; Walker, R. *J. Phys. Chem. C*, **2008**, *112*, 5232.

(118) Pomfret, M.; Owrutsky, J.; Walker, R. *Anal. Chem.*, **2007**, *79*, 2367.

(119) Pomfret, M.; Owrutsky, J.; Walker, R. *J. Phys. Chem. B*, **2006**, *110*, 17305.

(120) Pomfret, M.; Steinhurst, D.; Kidwell, D.; Owrutsky, *J. Electrochem. Soc. Trans.*, **2009**, *25*, 839.

(121) Pomfret, M.; Steinhurst, D.; Kidwell, D.; Owrutsky, J. *J. Power Sources*, **2010**, *195*, 257.

(122) Pomfret, M.; Stoltz, C.; Varughese, B.; Walker, R. *Anal. Chem.*, **2005**, *77*, 1791.

(123) Pornprasertsuk, R.; Ramanarayanan, P.; Musgrave, C.; Prinz, F. *J. Appl. Phys.*, **2005**, *98*, 103513.

(124) Qiao, J.; Sun, K.; Zhang, N.; Sun, B.; Kong, J.; Zhou, D. *J. Power Sources*, **2007**, *169*, 253.

(125) Rakass, S.; Oudghiri-Hassani, H.; Rowntree, P.; Abatzoglou, N. *J. Power Sources*, **2006**, *158*, 485.

(126) Randolph, K.; Dean, A. *Phys. Chem. Chem. Phys.*, **2007**, *9*, 4245.

(127) Randolph, K.; Dean, A. *Phys. Chem. Chem. Phys.*, **2007**, *9*, 4245.

(128) Recknagle, K.; Ryan, E.; Koeppel, B.; Mahoney, L.; Khaleel, M. *J. Power Sources*, **2010**, *195*, 6637.

(129) Ridder, M.; Welzenis, R.; Brongersma, H.; Kreissig, U. *Solid State Ionics*, **2003**, *158*, 67.

(130) Rossmeisl, J.; Bessler, W. *Solid State Ionics*, **2008**, *178*, 1694.

(131) Rupp, J; Drobek, T.; Rossi, A.; Gauckler, L. *J. Chem. Mater.*, **2007**, *435*, 795.

(132) Sammes, N.; Cai, Z. *Solid State Ionics*, **1997**, *100*, 39.

(133) Sasaki, K.; Watanabe, K.; Teraoka, Y. *J. Electrochem. Soc.*, **2004**, *151*, A965.

(134) Saunders, G.; Preece, J.; Kendall, K. *J. Power Sources*, **2004**, *131*, 23.

(135) Schmidt, M.; Hansen, K.; Norrman, K.; Mogensen, M. *Solid State Ionics*, **2009**, *180*, 431.

(136) Shao, Z.; Haile, S.; Ahn, J.; Ronney, P.; Zhan, Z.; Barnett, S. *Nature*, **2005**, *435*, 795.

(137) Sheng, C.; Dean, A. *J. Phys. Chem. A*, **2004**, *108*, 3772.

(138) Simpson, R., *Introductory Electronics for Scientist and Engineers*, ISBN 0205083773, Allyn and Bacon, Inc.

(139) Sin, A; Kopin, E.; Dubitsky, Y.; Zaopo, A.; Arico, A.; la Rosa, D.; Antonucci, V. *J. Power Sources*, **2007**, *164*, 300.

(140) Skoog, D.; Holler, F.; Nieman, T., *Principles of Instrumental Analysis*, ISBN 0-03-002078-6, Saunders College Publishing

(141) Song, C. *Catal. Today*, **2002**, *77*, 17.

(142) Staniforth, J.; Ormerod, R. *Green Chemistry*, **2001**, *3*, G61.

(143) Stathis, G.; Simwonis, D.; Tietz, F.; Moropoulou, A.; Naoumides, A. *J. Mater. Res.*, **2002**, *17*, 951.

(144) Stohr, J.; H.C.S., ed., *Magnetism From Fundamentals to Nanoscale Dynamics*, ISBN 3-540-30282-4, Springer

(145) Sukeshini, A.; Habibzadeh, B.; Becker, B.; Stoltz, C.; Eichhorn, B.; Jackson, G. *J. Electrochem. Soc.*, **2006**, *153*, A705.

(146) Sun, C.; Stimming, U. *J. Power Sources*, **2007**, *171*, 247.

(147) Sun, C.; Stimming, U. *J. Power Sources*, **2007**, *171*, 247.

(148) Sundes, S. *Electrochim. Acta.*, **1997**, *42*, 2637.

(149) Suwanwarangkul, R.; Croiset, E.; Entchev. E.; Charojrochkul, S.; Pritker, M.; Fowler, M.; Douglas, P.; Chewathanakup, S.; Mahaudom, H. *J. Power Sources*, **2006**, *161*, 308.

(150) Svensson, A.; Sunde, S.; Nisancioglu, K. *J. Electrochem. Soc.*, **1998**, *145*, 1390.

(151) Svensson, A.; Sunde, S.; Nisancioglu, K. *J. Electrochem. Soc.*, **1997**, *144*, 2719.

(152) Swider, K; Worrell, W. *J. Electrochem. Soc.*, **1996**, *143*, 3706.

(153) Tanaka, Y.; Nguyen, T. ; Kato, T.; Shimada, T.; Sugano. K.; Negishhi, A.; Kato, K.; Nozaki, K. *Solid State Ionics*, **2006**, *177*, 3323.

(154) Tikekar, N.; Armstrong, T.; Virkar, A. *J. Electrochem. Soc.*, **2006**, *153*, A654.

(155) Vernoux, P.; Guth, M.; Li, X. *Electrochem. Solid State Lett.*, **2009**, *12*, E9.

(156) Villano, S.; Hoffmann, J.; Carstensen, H.; Dean, A. *J. Phys. Chem. C*, **2010,** *114***,** 6502.

(157) Wachsman, E.; Jiang, N.; Frank, C.; Mason, D.; Stevenson, D. *Appl. Phys. A*, **1990**, *50*, 545.

(158) Walters, K.; Dean, A.; Zhu, H.; Kee, R. *J. Power Sources*, **2003**, *123*, 182.

(159) Wang, C.; Xui, L.; Tang, W. *Rare Metal Mater. Eng.*, **2006**, *35*, 501.

(160) Wang, J., *Analytical Electrochemistry*, ISBN 0-471-67879-1, John Wiley & Sons

(161) Wright, D.; Thorp, J.; Aypar, A.; Buckley, H. *J. Mat. Sci.*, **1973**, *8*, 876.

(162) Ye, X.; Huang, B.; Wang, S.; Wang, Z.; Xiong, L.; Wen, T. *J. Power Sources*, **2007**, *164*, 203.

(163) Zhan, Z.; Barnett, S. *Science*, **2005**, *308*, 844.

(164) Zhan, Z.; Barnett, S. *Solid State Ionics*, **2005**, *176*, 871.

(165) Zhang, X.; Robertson, M.; Deces-Petit, C.; Qu, W.; Kesler, O.; Maric, R.; Ghosh, D. *J. Power Sources*, **2007**, *164*, 668.

(166) Zhu, H.; Kee, R. *J. Electrochem. Soc.*, **2006**, *153*, A1765.

(167) Zhu, H.; Kee, R.; Janardhanan, V.; Deutschmann, O.; Goodwin, D. *J. Electrochem. Soc.*, **2005**, *152*, A2427.

(168) Zhu, W.; Deevi, S. *Mater. Sci. Eng. A.*, **2003**, *362*, 228.

(169) Zhu, W.; Ding, D.; Xia, C. *Electrochem. Solid State Lett.*, **2008**, *11*, B83.

(170) Zhu, W.; Xia, C.; Fan, J.; Peng, R.; Meng, G. *J. Power Sources*, **2006**, *160*, 897.